Structure and Dynamics of the Pt-Ge Eutectic System

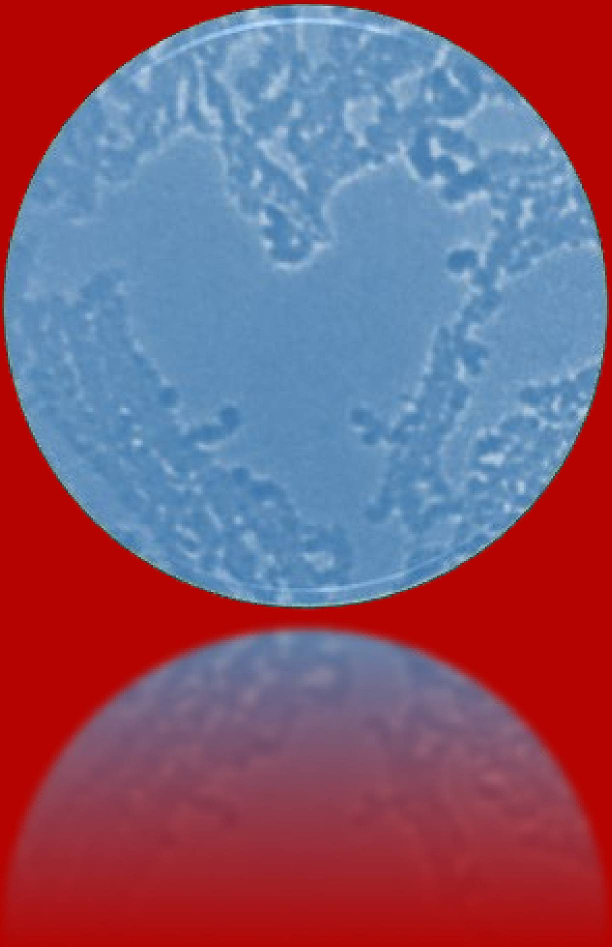

Zhiguo Zhang

STRUCTURE AND DYNAMICS OF THE PT-GE EUTECTIC SYSTEM

Zhiguo Zhang

Graduation Committee

Chairman/secretary:	
Prof. dr. J.L. Herek	University of Twente
Supervisor:	
Prof. dr. H.J.W. Zandvliet	University of Twente
co-supervisor:	
Dr. A. van Houselt	University of Twente
Committee members:	
Prof. dr. J.C.T. Eijkel	University of Twente
Prof. dr. ir. R.G.H. Lammertink	University of Twente
dr.ir. H. Wormeester	University of Twente
Prof. dr. H.R. Wu	China University of Petroleum Beijing
Prof. dr. W.X. Tang	Chongqing University

The research is financed by the China Scholarship Council (CSC).

The work and content for this thesis have been carried out at the Physics of Interfaces and Nanomaterials Group, MESA+ Institute for Nanotechnology, University of Twente, Enschede, The Netherlands.

Zhiguo Zhang
Structure and dynamics of the Pt-Ge eutectic system

ISBN: 978-90-365-5325-4
DOI: 10.3990/1.9789036553254

Cover designed by: Zhiguo Zhang

STRUCTURE AND DYNAMICS OF THE PT-GE EUTECTIC SYSTEM

DISSERTATION

to obtain
the degree of doctor at the University of Twente,
on the authority of the rector magnificus,
prof.dr. ir. A. Veldkamp,
on account of the decision of the Doctorate Board,
to be publicly defended
on Wednesday 26th of January 2022 at 12:45 hours

by

Zhiguo Zhang

born on 3rd July 1990
in Linquan, China.

This dissertation has been approved by:

Supervisor: Prof. dr. H.J.W. Zandvliet	University of Twente
Co-supervisor: Dr. A. van Houselt	University of Twente

CONTENTS

PREFACE

Never forget why I start, and my mission can be accomplished.

不忘初心
方得始终

Zhiguo Zhang
Enschede, . . . 2022

1

INTRODUCTION

1.1. INTRODUCTION

THE main objective in this thesis is to understand, and ultimately tailor, the properties of the platinum (Pt) on Germanium(110) system. The Pt on Ge system hosts a myriad of interesting physics, which will be introduced in this chapter, as well as the basic properties of the Ge(110) surface, which is used as a substrate throughout this thesis.

1.2. THE PT-GE SYSTEM

THE Pt-Ge system is well studied, due to the possible applications of metallic structures on Ge surfaces in the electronic industry [1]. The first point-contact transistor was made of germanium. Nevertheless, nowadays silicon (Si) is used in integrated circuits in modern technology, to a large extend due to the stability at high temperatures and electrical powers and the stable natural oxide. The renewed interest in Ge stems mainly from its smaller bandgap compared to Si, combined with the substantially higher electron and hole mobilities for Ge. In principle this can lead to faster devices with higher switching speeds [2].

In case of Pt on Ge surfaces, a bottom-up approach, i.e. self-organization after atomic deposition at room temperature and subsequent annealing at elevated temperatures, is a promising route towards the creation of one-dimensional (1D) or two-dimensional (2D) nanostructures. There is a fundamental reason to study 1D and 2D nanostructures, since crystal properties are heavily depending on the dimensionality of the crystal and exciting and exotic physics can be expected like Luttinger liquid behaviour, massles Dirac fermions, etc [3, 4]. In addition, calculations might become easier when one reduces dimensions, while with the ongoing scaling down of the electronic components in the semiconductor industry, the interest in nanowires, nanoswitches and other electronic components increases likewise [5-7].

After the deposition of Pt on Ge(001) self-organization of 1D wires is observed [8], while for deposition of Pt on Ge(110) the formation of the 2D material germanene is observed [9]. In the following we briefly introduce the formation of these 1D and 2D materials on Ge(001) and Ge(110), respectively.

1.3. THE PT-GE PHASE DIAGRAM

In Fig. 1.1 we reproduce the Ge-Pt bulk phase diagram [10]. It displays many different Ge-Pt alloys. For our current study the Pt-poor side is of interest. We focus on the part from 0 to 22 %Pt. We observe in the Ge-rich part of the phase diagram the formation of an eutecticum: a mixture with a composition of 22 % Pt and 78 % Ge will form a binary liquid, below the melting temperatures of the neighboring phases, pure Ge (melting at 1211 K) and Ge_2Pt (melting at 1101 K). In the following chapters we will frequently use this property of the Pt-Ge system.

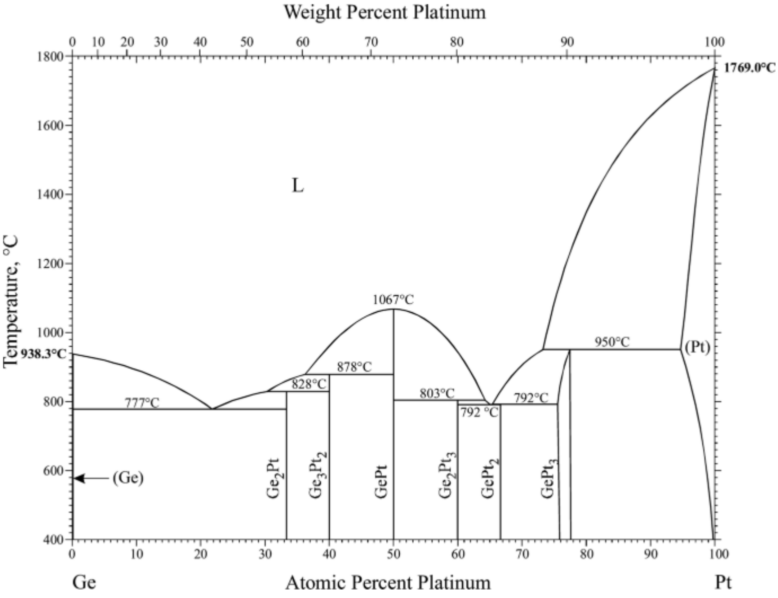

Figure 1.1: Bulk phase diagram of Pt-Ge alloys, reproduced from ref [10].

1.4. THE PT/GE(001) SYSTEM

Ge exhibits the diamond crystal structure, which is composed of two interpenetrating fcc sublattices. When a crystal is cut along the (001) plane, every surface atom is left with two dangling bonds. To minimize the surface free energy, these atoms form dimers. Upon deposition of Pt on the Ge(001) surface and subsequent annealing, the formation of 1D wires is observed [11]. These 1D wires are one atom wide and up to a micron long. It is reported that these wires confine electron states,since the wires act as barriers [12]. Using scanning tunneling microscopy and spectroscopy it was shown that these 1D electronic state are exclusively present in the troughs between the 1D wires [12,13]. The two sub-bands which are resolved correspond to the lowest energy levels of a quantum mechanical particle in a box [13]. Upon cooling from room temperature to 4.7 K, a phase transition from a 2x periodicity to a 4x periodicity is observed, which is accompanied by a reduction in the metallicity of the wires, and is therefore interpreted as a Peierls instability [14].

1.5. THE GE(110) SURFACE

BEFORE we introduce the physics of the Pt/Ge(110) system, we first describe the Ge(110) surface in a bit more detail.

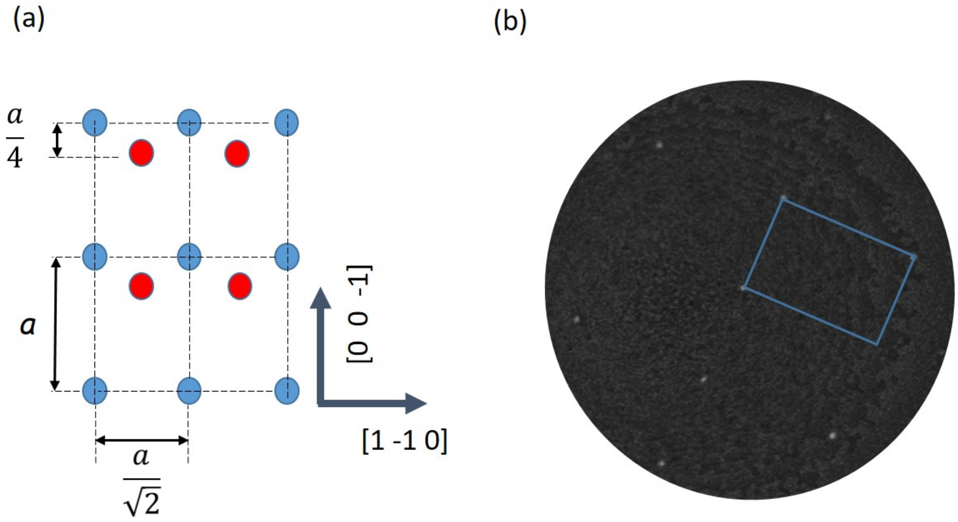

Figure 1.2: The atomic structure of the Ge(110) surface in real space and reciprocal space: (a) Atomic structure of the bulk truncated Ge(110) surface in real space. The lattice constant of Ge is 0.565 nm; (b) LEED image measured with 30 eV electronics at 1100 K. The unit cell is indicated by the blue rectangle. For more details, see chapter 4.

The low-index surfaces of the group IV semiconductors have been extensively studied, except the (110) surface. The (110) surface is intrinsically anisotropic and has higher surface free energy per unit area than the (100) and (111) surfaces. It therefore shows the tendency to facet. The bulk truncated Ge(110) surface exhibits rectangular symmetry and is composed of zigzag rows of atoms running in the [1-10] direction. The Ge(110) surface reconstructs into large cells at room temperature. The most common surface reconstructions are the (16×2) and the $c(8\times10)$ reconstructions, which are both composed of five-membered atom rings, known as pentagons and involve {17 15 1} facets as steps. Structural models of the (16×2) and $c(8\times10)$ reconstructions are discussed in Ichikawa's papers [15]. Mullet and Chiang [16] reported a $c(8\times10)$ phase upon quenching rapidly from 1070 K to room temperature, while the (16×2) phase was absent in that case. They suggested that this (8×2) phase emerged as a consequence of the absence of alternating rows of missing top layer atoms, which are the basis of the (16×2) reconstruction. Fig 1.2 presents an atomic schematic of the bulk truncated Ge(110) surface in real space and a measured Low Energy Electronic Diffraction (LEED) pattern of the Ge(110) surface at a temperature above the transition to a (1×1) phase. Fig 1.3 presents a LEEM image and LEED patterns at room temperature and high temperature. In the LEEM image shown in Fig 1.3 (a), steps or step bunches are visible. Fig. 1.3(b) shows a schematic of the LEED pattern of the Ge(110)-$c(8\times10)$ structure taken from ref. [17]. Fig. 1.3(c) shows a measured LEED pattern at room temperature. By comparing Fig 1.3 (b) [17] and Fig 1.3 (c), it is clear that the $c(8\times10)$ phase was obtained at room temperature, which is in accordance with the observations by Mullet and Chiang [16]. At elevated temperatures, the $c(8\times10)$ phase converts into the (1×1) phase, as shown in Fig 1.3 (d).

1.6. THE PT/GE(110) SYSTEM

DEPOSITION of Pt on Ge(110) and subsequent annealing above the eutectic temperature (see the phase diagram in fig. 1.1.) results in micrometer sized eutectic droplets on the substrate. Upon cooling down, the eutectic droplets undergo spinodal decomposition into a Ge_2Pt an a pure Ge phase. Due to the lower surface free energy of Ge compared to Ge_2Pt, the Ge atoms segregate to the droplet/vacuum interface. There the Ge atoms form a buckled honeycomb lattice with a lattice constant of ~ 4.2 Å. Bampoulis *et al.* [9] managed to atomically resolve this structure in STM measurements and pointed out that this structure can be interpreted as germanene, *i.e.* the germanium analogue of graphene. They were able to show that the honeycomb lattice is buckled as predicted by density functional theory calculations. Later Zhang *et al.* [18] measured the density of states of germanene and found a clear V-shape, which is one of the hallmarks of a 2D Dirac system.

2D materials have a thickness of only a single layer. Since the start of the 2D materials research field with the isolation of graphene by Geim and Novoselov [19, 20], the research

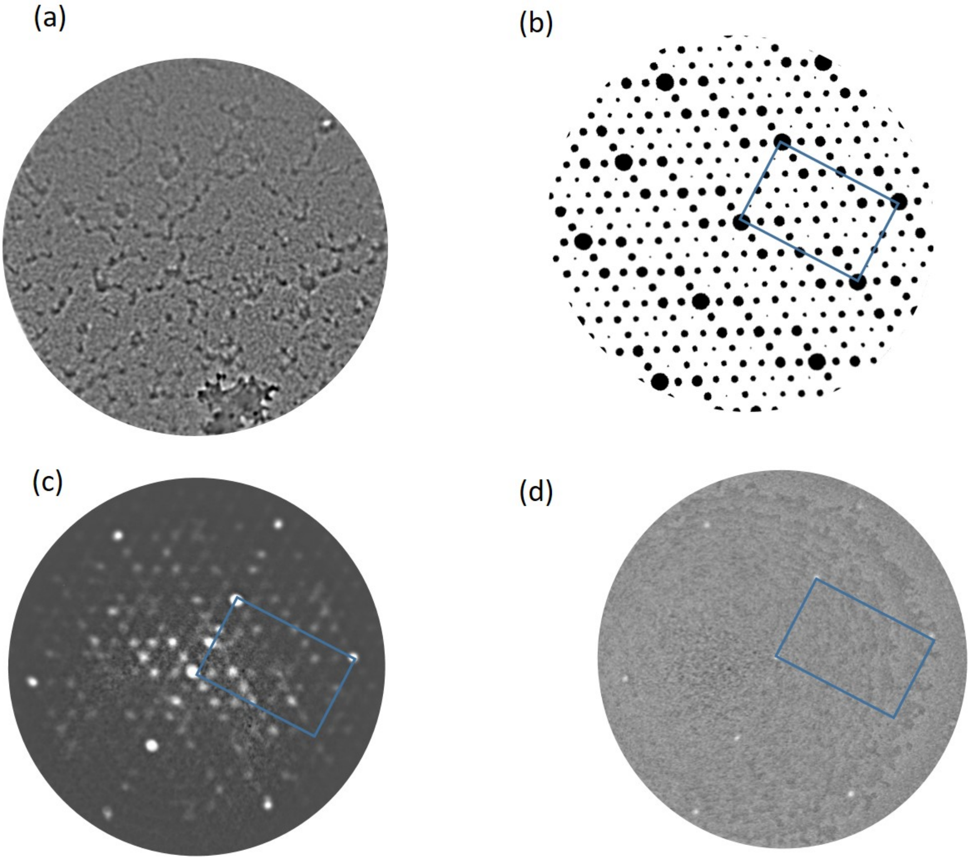

Figure 1.3: LEEM and LEED images of the Ge(110) substrate: (a) LEEM image of Ge(110) obtained with 3.0 eV energy electrons at T = 300 K; (b) Schematic of the Ge(110)-$c(8\times10)$ structure [17]; (c) and (d) LEED images obtained with 30 eV energy electrons at T = 300 K and 1100 K, respectively.

field exploded. From simple tight binding calculations one can extract that graphene is a semimetal: the maximum of the valence band and the minimum of the conduction band touch at the Fermi level. The energy bands in the vicinity of the Fermi level exhibit a linear energy-momentum dispersion relation, which gives rise to the earlier mentioned V-shape in the density of states. This linear dispersion relation also implies that electrons in graphene behave as massless Dirac fermions, obeying the relativistic Dirac equation. Besides these intriguing fundamental properties also the high electrical conductivity, good thermal conductivity, high mechanical strength and flexibility of graphene are promising properties for numerous applications. A drawback is, however, that graphene lacks a bandgap and thus cannot be used in field-effect based applications.

The other group IV elements of the periodic table, Si, Ge and Sn, are very similar to carbon, in the sense that they all have two electons in their outermost s and p shells, and therefore it is very likely that they can also form graphene-like honeycomb structures [9, 21- 24]. These analogues of graphene do not occur in nature and have to be synthesized. Silicene was successfully synthesized in 2012 [21], followed by germanene in 2014 [23] and stanene in 2015 [24].

The evolution of Pt on Ge(110) during heating to the eutectic temperature, above the eutectic temperature, and subsequently cooling down is the topic of this thesis.

1.7. OUTLINE OF THIS THESIS

THE techniques employed in this study are introduced and discussed in Chapter 2.

In chapter 3 we study in situ the shape and work function of the eutectic Pt-Ge droplets formed at elevated temperatures on the Ge(110) surface. We will show that we can successfully extract both the contact angle of the hemispherical droplet as well as the work function of this droplet from our measurements.

In chapter 4 we discuss the motion of the eutectic droplets. We show that they all move to the local hot spot on the surface and we discuss the underlying physics in relation with existing models for similar motion in other systems. We will show that in our case the existing models fail spectacularly to describe the observed behaviour.

In chapter 5 we continue our in situ study of the eutectic droplets during cooling down. We follow the droplet dynamics during controlled cooling down and discuss, using electron diffraction measurements, the structures which emerge in the neighborhood of the local hot spot on the surface.

Finally in chapter 6 we summarize our findings and finish off with a brief outlook.

BIBLIOGRAPHY

[1] R. Pillarisetty, Nature **47**, 324 (2011).

[2] J.H. Zhou, C.X. Zhang, Q.R. Liu, J. You, X. Zheng, X.A. Cheng, and T. Jiang, Nanophotonics **7**, 2797 (2020).

[3] R. Egger, Phys. Rev. Lett. **8**, 5547 (1997).

[4] R. Egger, Phys. Rev. B **85**, 235462 (2012).

[5] L. Jung, J.L. Pries, T.W.W. Maβ, M. Lewin, D.S. Boyuk, A.T. Mohabir, M.A. Filler, M. Wuttig, and T. Taubner, ACS Photonics **6**, 1744 (2019).

[6] S. Demoustier, E. Minoux. M. Le Baillif, M. Charles, and A. Ziaei, C.R. Physique **9**, 53 (2008).

[7] J. Schäfer, S. Meyer, C. Blumenstein, K, Roensche, R. Claessen, S. Mietke, M. Klinke, T. Podlich, R. Matzdorf, A.A. StekoInikov, S. Sauer, and F. Bechstedt, New. J. Phys. **11**, 125011 (2009).

[8] O. Gurlu, O.A.O. Adam, and H.J.W. Zandvliet, Appl. Phys. Lett. **83**, 4610 (2003).

[9] P. Bampoulis, L. Zhang, A. Safaei, R van Gastel, B. Poelsema, and H.J.W. Zandvliet, J. Phys.: Condens. Matter. **26**, 442001 (2014).

[10] H. Okamoto, J. Phase Equilib. Diffus. **40**, 311 (2019).

[11] S.F. Tsay, Surf. Science. **606**, 1405 (2012).

[12] N. Oncel, A.van Houselt. J. Huijben, A. Hallbäck, O. Gurlu. H.J.W. Zandvliet, and B. Poelsema, Phys. Rev. Lett. **95**, 116801 (2015).

[13] D. Kockmann, B. Poelsema, and H.J.W. Zandvliet, Nano. Lett. **9**, 1147 (2009).

[14] C. Blumenstein, J. Schäfer. M. Morresi, S. Mietke, R. Matzdorf, and R. Claessen, Phys. Rev. Lett. **107**, 165702 (2011).

[15] T. Ichikawa, Surf. Science **544**, 58 (2003).

[16] C.H. Mullet and S. Chiang, Surf. Sci. **621**, 184 (2014).

[17] B.Z. Olshanetsky, S.M. Repinsky, and A.A. Shklyaev, Surf. Sci. **64**, 224 (1977).

[18] L. Zhang, P. Bampoulis, A.N. Rudenko, Q. Yao, A. van Houselt, and H.J.W. Zandvliet, Phys. Rev. Lett. **116**, 256804 (2016).

[19] A.H.C. Neto, F. Guinea, N.M.R. Peres, K.S. Novoselvo, and A.K. Geim, Rev. Mod. Phys. **81**, 109 (2009).

[20] K.S. Nomoselov, A.K. Geim, S.V. Morozov, V. Giacometti, D. Jiang, Y. Zhang, S.V. Dubonos, I.V. Grigorieva, and A.A. Firsov, Science **306**, 666 (2004).

[21] P. Vogt, P. Padova, C. Quaresima, J. Avila, E. Frantzeskakis, M.C. Asensio, A. Resta, B. Ealet, and G. Le Lay, Phys. Rev. Lett. **108**, 155501 (2012),

[22] J.J. Yuhara, H.K. Shimazu, K. Ito, A. Ohto, M. Araidai, M. Kurosawa, M. Nakatake, and G. Le Lay, ACS Nano. **12**, 11632 (2018).

[23] L.F. Li, S.Z. Lu, J.B. Pan, Z.H. Qin, Y.Q. Wang, Y.L. Wang, G.Y. Cao, S.X. DU, H.J. Gao, Adv. Mater. **26**, 4820 (2014).

[24] F.F. Zhu, W.J. Chen, Y. Xu, C.L. Gao, D.D. Guan, C.H. Liu, Q. Dong, S.C. Zhang, and J.F. Jia, Nature Materials **14**, 1020 (2015).

2

EXPERIMENTAL

This chapter introduces low energy electron microscopy (LEEM), low energy electron diffraction (LEED) and photo-emission electron microscopy (PEEM), the methods that are used in this thesis.

2.1. INTRODUCTION

SPECIAL experimental techniques are required to analyze surface structures, surface composition and dynamics at surfaces. In the case of eutectic droplets and surface structures at high temperatures, the topic of this thesis, only a limited subset of experimental techniques is available. In order to follow the motion of eutectic droplets and to study the accompanied surface reconstructions, one needs real time and in-situ measurements. In this thesis, Low Energy Electron Microscopy (LEEM), Low Energy Electron Diffraction (LEED) and Photo Emission Electron Microscopy (PEEM) were used to perform the experiments.

2.2. LOW ENERGY ELECTRON MICROSCOPY

LEEM is an in-situ imaging technique, which enables the analysis of surface processes, for example, thin film growth, droplet growth and coalescence and other dynamical processes in ultra-high vacuum (UHV) [1]. In LEEM, the surface is imaged by low energy electrons, which are reflected from the sample surface without energy loss. Due to the large scattering cross-section of most materials for electrons that backscatter elastically, LEEM is an efficient technique to perform real time video-imaging. To obtain high quality images, the sample has to be cleaned by a combination of physical and chemical cleaning cycles. LEEM is a very surface sensitive technique, because the penetration depth of electrons with an energy of several eV and a corresponding de Broglie wavelength of a few Angstroms is in the order of a few nanometers. The lateral resolution of LEEM is limited to about ten nanometer.

Figure 2.1 shows a simplified schematic representation of the image formation process in LEEM. Electrons that leave the sample under the same angle are focused in the back focal plane of the objective lens, resulting in a diffraction pattern. In normal LEEM imaging, the beam of back-scattered electrons is selected to form an image of the surface. The beam of back-scattered electrons enable imaging at frame rates nearly up to frequencies as high as 10 Hz, provided that the source delivers sufficient intensity. Figure 2.2a shows the Elmitec LEEM III, which was used to perform the experiments described in this thesis. A LaB_6 electron gun, mounted at the beginning of the illumination column, generates the incoming electron beam with an energy of 20 kV, and is controlled by a Wehnelt cap, located just in front of the gun. In the illumination column, a set of condenser lenses is employed to focus the incident electron beam towards the sector field, which deflects the beam by 60 degree along the optical axis of the objective lens, which faces the sample holder in the main chamber. In the sector field, an illumination aperture can be inserted, which selects the size of the beam. The illumination aperture enables a selection of the beam cross-section on the sample of 1.4, 4.8, or 19 micrometer, respectively. The incoming electron beam is decelerated by an electric field between the electrically grounded objective lens and the sample, while the outgoing electron beam is accelerated by the same electric field. The electrons are decelerated to an energy level between -5 and 100 eV (called "Start Voltage (SV)"), before they interact with the sample. This is achieved by biasing the sample at the negative beam voltage of 20 kV, plus SV. The electrons reflected from the sample surface are accelerated by the same field, and focused in the back focal plane of the objective lens, where they form a diffraction pattern. Then the beam changes direction in the beam separator. After leaving the beam separator, the electrons enter into the imaging column.

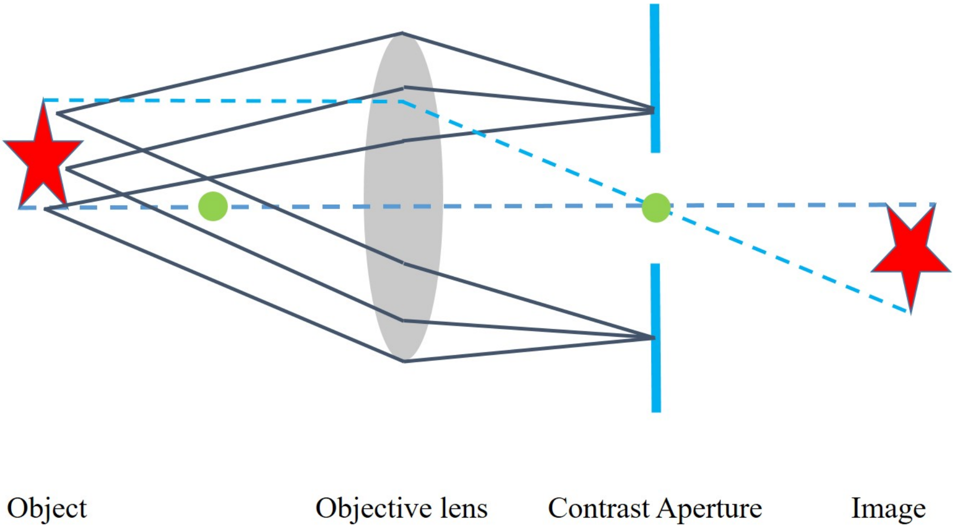

Figure 2.1: Basic schematic of the electron optics. The backscattered electrons are focused onto the back-focal plane to form a diffraction pattern. The contrast aperature is employed to select a diffraction spot, which is used for imaging.

When no diffraction spot is selected by the contrast aperture in the imaging column (see figure 2.2), the instrument is operated in the LEED mode (when an illumination aperature is used, this is called the μLEED mode or selected area diffraction) and the diffraction pattern in the back focal plane of the objective lens is projected onto the screen.

When the contrast aperature is used to select the specular diffraction spot, a real space image of the surface is imaged in the bright field mode. In this mode contrast arises from different electron reflectivities due to differences in the electronic and crystalline structure. Steps or step bunches are visible as a consequence of phase contrast: electrons reflected from both sides of a step (bunch) have a different path length, and thus a different phase, resulting in destructive or constructive interference. When sufficiently low start voltages are used, the incident electrons are reflected before they reach the surface. This way of operation is called the mirror mode. In the mirror mode the interaction with the sample is minimal, resulting in a high intensity. Upon increasing the electron energy, the electron beam starts to interact with the unoccupied states in the sample, thus lowering the intensity. In chapter 3 the onset of this intensity dip is used to determine the local work function of the surface.

When the contrast aperature is used to select a non-specular beam, this is referred to as dark field imaging. Dark field imaging is for instance very helpful to visualise the two different domain orientations of Si(001) [2] and Ge(001) surfaces [3].

Finally, another set of lenses focuses the beam on a Micro Channel Plate (MCP), which consists of a two-dimensional periodic array of glass capillaries fused together. A single incident electron entering a channel emits an electron from the channel wall. The generated secondary electrons are accelerated by an applied electric field and also strike the channel surface, thus producing more electrons. As a result, this cascade process results in a cloud of thousands of electrons, emerging from the rear of the plate. They hit a fluorescent screen at the end of the column, thus producing an image. A high resolution charge coupled device (CCD) camera captures the images from the fluorescent screen. The entire beam route is schematically presented in Figure 2.2b.

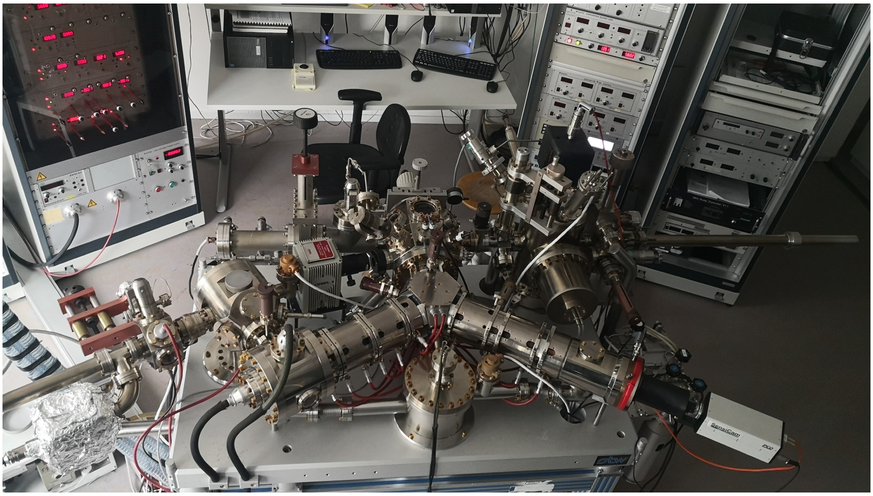

(a) Photograph of the Elmitec LEEM III instrument used for the experiments described in this thesis.

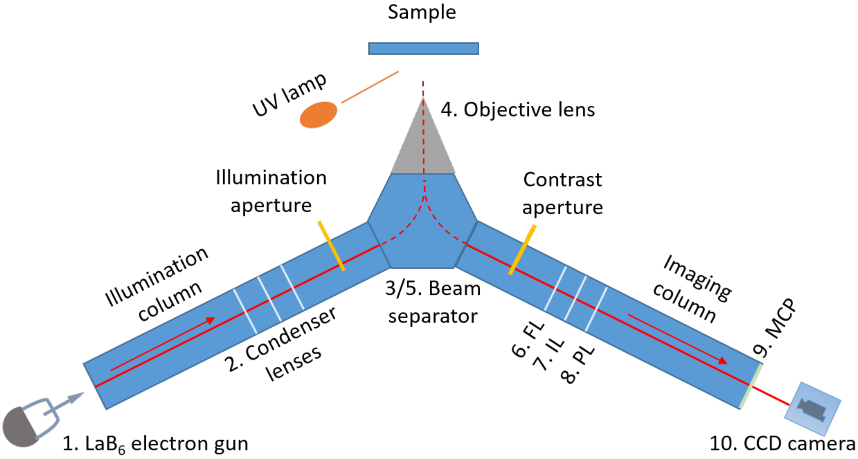

(b) Schematic drawing of the electron beam path way.

Figure 2.2: Experimental setup (a) Elmitec LEEM III employed for experiments in this thesis; and (b) schematic route of the pathway of the electrons through the instrument: 1) LaB$_6$ electron gun; 2) condenser lenses; 3) beam separator; 4) objective; 5) beam separator; 6) field lens (FL); 7) intermediate lens (IL); 8) Projection lens (PL); 9) microchannel plate (MCP) 10) CCD camera.

2.2.1. CORRECTED LEEM IMAGES

DUE to the existing defects and inhomogeneities in the channel plate in our instrument, the obtained LEEM images are corrected, as illustrated in Figure 2.3. To do so, a mirror image is recorded before performing an experiment. In the mirror mode the contrast is due to the long ranging differences in the surface work function. Thus for a clean surface, the mirror image is featureless and for every pixel of the image proportional to the local amplification factor of the MCP. A devision by a mirror image corrects thus for the inhomogeneities and defects in the MCP. The corrected images are achieved by dividing the original images by the mirror image.

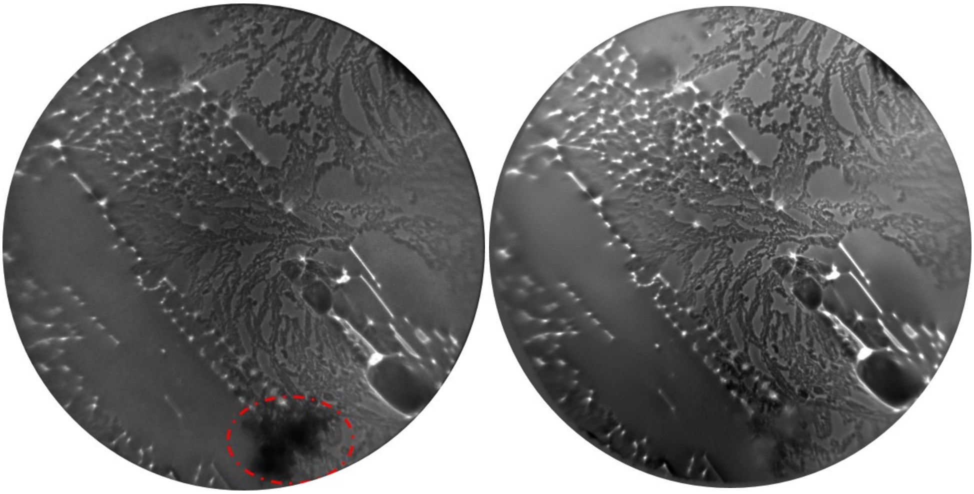

(a) Original LEEM image.

(b) Corrected LEEM image.

Figure 2.3: (a) Original LEEM image (SV = 1.2 eV, FOV = 20 μm) with a butterfly feature due to a defect (encricled) on the channel plate and (b) Corrected LEEM image for inhomogeneities in the MCP.

2.3. LOW ENERGY ELECTRON DIFFRACTION

LEEM has the ability to measure Low Energy Electron Diffraction (LEED) patterns. As mentioned already before, the reflected electrons from the sample are accelerated again by the electric field between the sample surface and the objective lens. The electrons that have left the sample under the same angle are focused into a single diffraction spot in the back focal plane of the objective lens. These spots together form a LEED pattern in the back focal plane, which is projected on the MCP detector.

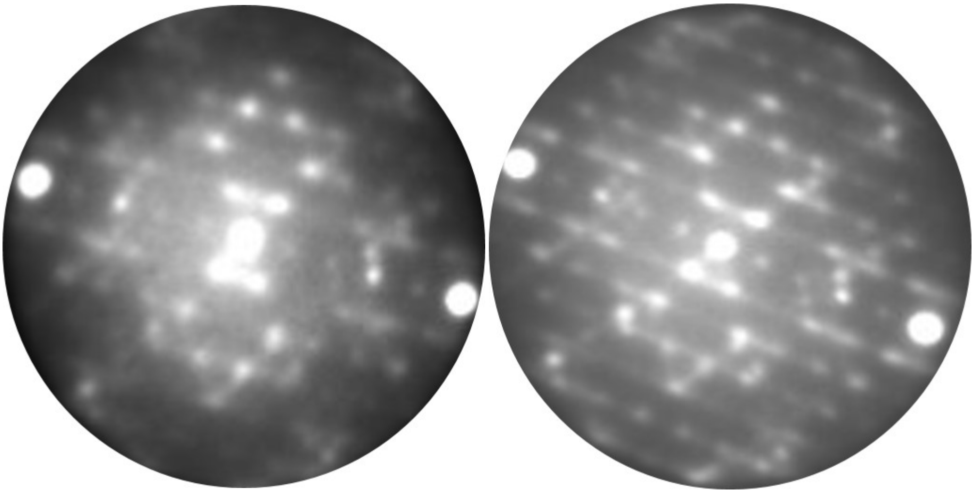

(a) Unsharp LEED pattern.

(b) Sharp LEED pattern.

Figure 2.4: Measured LEED patterns: (a) Blurred LEED pattern (SV = 5.0 eV) and (b) Sharp LEED pattern (SV = 5.0 eV).

LEED measurements are quite significant for our investigations, because they help us to distinguish not only whether the surface of our sample is clean or not, but also to resolve the structure of different domains by insertion of an illumination aperture (so called μLEED). Figure 2.4 shows LEED patterns, of the $c(8 \times 10)$ reconstruction on Ge(110). The left LEED image is blurry due to contamination of the sample surface. After several cycles of sputtering and annealing, the sample gets cleaner and the contamination is removed, leading to a sharp LEED pattern in Figure 2.4b.

2.3.1. CORRECTED LEED PATTERN

SECONDARY electrons (inelastically scattered electrons) form a diffuse background in the diffraction pattern, especially in the patterns obtained at higher start voltages. These secondary electrons hamper analysis of the diffraction patterns, see for example Figure 2.5a, where the secondary electrons cover part of the 1/2 order spots in the diffraction pattern. To correct for these secondaries, we determine for each image the background image, containing only the secondaries. First, a minimum filter is applied, which replaces each pixel value by the minimum value found in a predefined radius around it. This radius should be larger than the spots size radius, usually 15-20 pixels are sufficient. Subsequently, the reverse action is performed with a maximum filter applied for the same radius, followed by a Gaussian filter to smooth the background image. Then the original pattern is divided by the background image. In the corrected pattern in Figure 2.5b, all the half order spots, are observed. For more details on the diffraction pattern in Figure 2.5 we refer to Chapter 4.

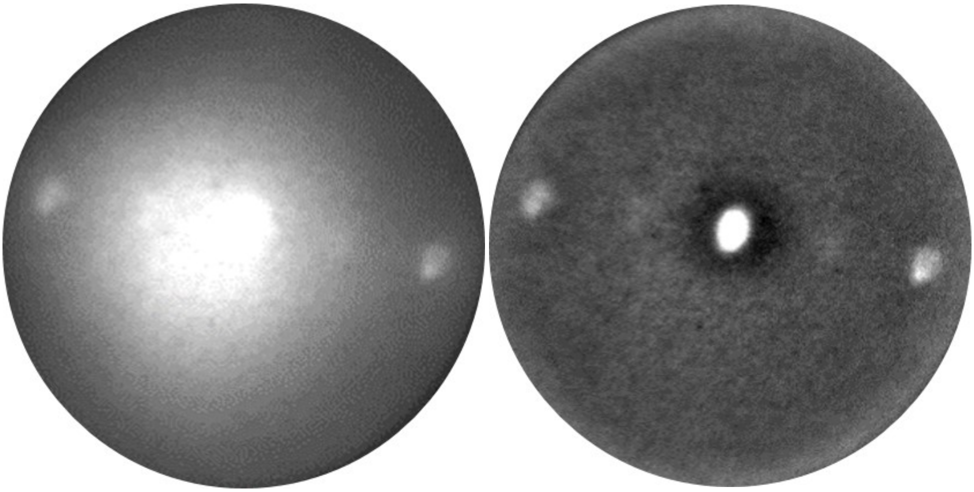

(a) Original μLEED image. (b) Corrected μLEED image.

Figure 2.5: The half order spots are much better visible in the corrected image. (a) Original LEED pattern (SV = 7 eV) and (b) LEED pattern of the Pt/Ge(110) surface corrected for the secondary electron cloud (see chapter 4 for more details on the Pt/Ge(110) LEED pattern).

2.3.2. CUMULATIVE LEED PATTERN

A single μLEED pattern measured at a given start voltage might contain spots that fulfill the out of phase condition for that energy, and, hence, they will be hardly visible. To avoid this problem, LEED patterns obtained at a range of start voltages are measured. Then, we stack them together into one single image by selecting the maximum intensity from the whole range for each pixel. An example is shown in Figure 2.6. All the spots are now clearly visible. Note that the edges of the Ewald spheres for the used energies show up as artifacts in this image. Alternatively, one could take the average intensity over the sampled energy range.

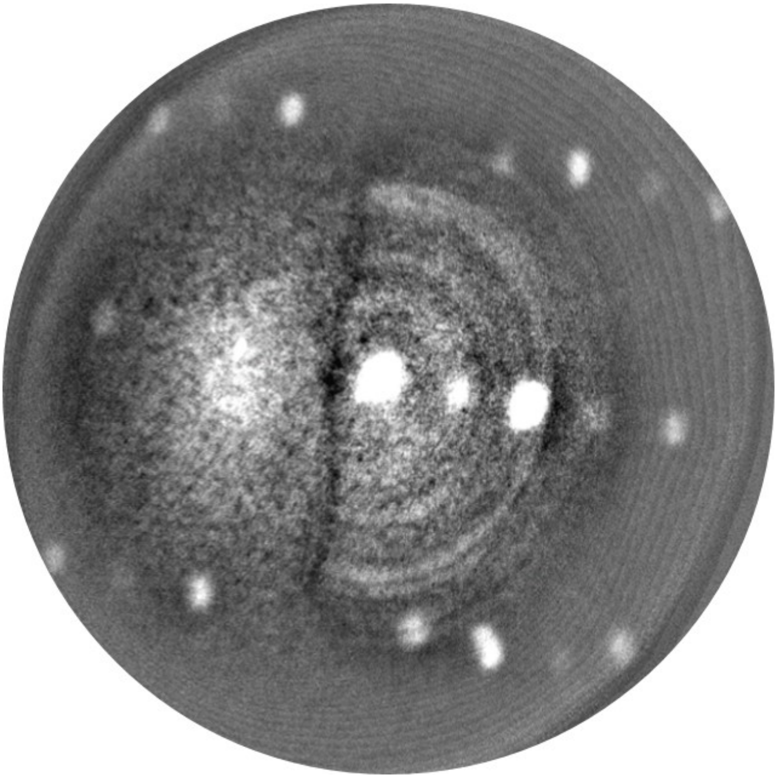

Figure 2.6: Cumulative LEED pattern, stacking series of LEED patterns from 5 eV to 30 eV on Pt/Ge(110). For details on the diffraction pattern we refer to the Chapter 4.

2.4. PHOTOEMISSION ELECTRON MICROSCOPY (PEEM)

In PEEM mode, a hydrogen discharge UV lamp (100 W, $\lambda = 0.253\ \mu$m) is used to illuminate the sample. When the photon energy exceeds the threshold for photo-emission, a photo-emission image of the surface can be obtained using the imaging collum in Figure 2.2. PEEM is surface sensitive, because the emitted electrons have a limited escape depth. In general, the photoelectrons originate from the valence band and core level electrons. This provides work function contrast and chemical contrast [4]. Deposited material or adsorbed molecules lead to a local change of the work function, hereby affecting the PEEM intensity. Additionally, a phase transition can also be observed in PEEM. An example of a PEEM image is shown in Figure 2.7, where eutectic Pt-Ge droplets are observed as bright circles. The information in this image is discussed in detail in Chapter 3.

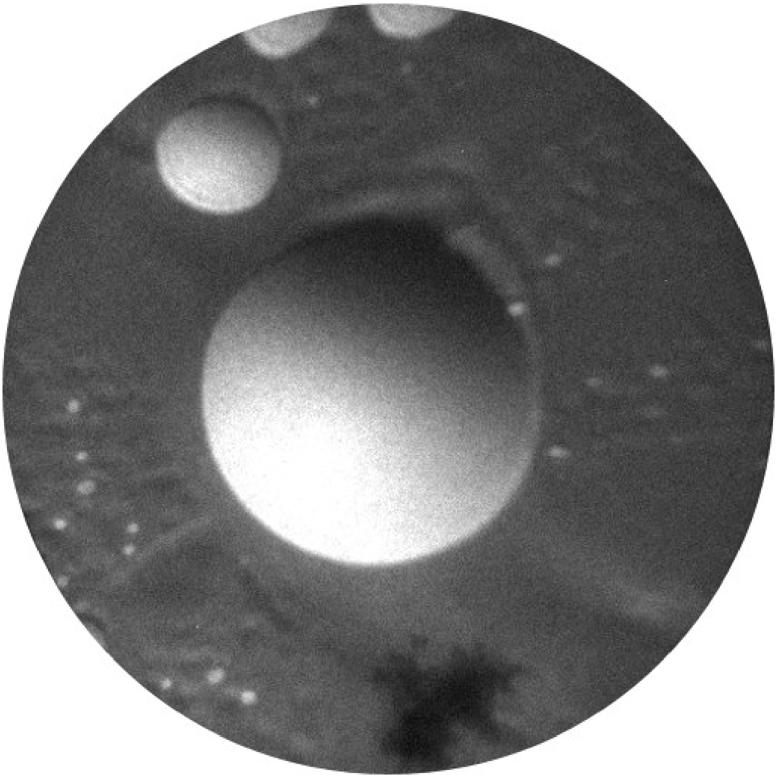

Figure 2.7: PEEM image (FOV = 150 μm) of the Pt/Ge(110) surface, obtained above the eutectic temperature (see chapter 3 for more details).

2.5. SURFACE PREPARATION

THE experiments have been performed with an Elmitec LEEM-III instrument with a base pressure lower 1×10^{-10} mbar. A Ge(110) substrate, 10 mm x 10 mm nominally flat, single-side-polished n-type Ge (110) crystals (MTI Corporation, R > 50 Ω cm) was used. After sample was introduced into the LEEM, firstly it was degassed for about 24 hours at 700 K, followed by several cycles of Argon ion bombardment and flash annealing by e-beam bombardment at a temperature exceeding 1000 K. We proceeded with these cycles untill we obtained a sharp c(8×10) LEED pattern, Pt is deposited from a resistively heated W wire wrapped with high purity (99.995 %) Pt (Alfa Aesar).

BIBLIOGRAPHY

[1] E. Bauer, Ultramicroscopy **119**, 18 (2012)

[2] N.C. Bartelt, W. Theis, and R.M. Tromp, Phys. Rev. B. **16**, 11741 (1996).

[3] E. van Vroonhoven, H.J.W. Zandvliet, and B. Poelsema, Phys. Rev. Lett. **91**, 11741 (2003).

[4] E. Bauer, Rep. Prog. Phys. **57**, 897 (1994).

3

DETERMINATION OF THE SHAPE OF EUTECTIC PTGE DROPLETS USING PHOTOEMISSION ELECTRON MICROSCOPY

This chapter is published as Z. Zhang, B. Poelsema, H. J.W. Zandvliet and A. van Houselt, *Detailed characterization of supported eutectic droplets using photoemission electron microscopy*, Phys. Rev. Materials **5**, 105601 (2021).

Abstract Pt-Ge eutectic alloy droplets are scrutinized by microscopic analysis of electrons excited by 4.9 eV photons. Using only the work function and contact angle as fitting parameters, we determine the exact droplet shape that reproduces the experimental electron emission profile. The local inclination of the droplets' surface plays a decisive role in the generated emission profile. Intensity variations at the illuminated side of the eutectic droplets are a consequence of standing waves in the electromagnetic field responsible for excitation. Intensity variations at the non-illuminated side are ascribed to a diffraction pattern of the photons after their interaction with the droplet.

3.1. INTRODUCTION

SMALL liquid droplets on solid substrates have been intensively studied. With decreasing volumes the influence of different surface and line tensions play a decisive role in the equilibrium shape of the droplets [1]. A special class of (nano)droplets is formed by alloys composed of a deposited material and that of the substrate, which form above their eutectic temperature. Applications involve the growth of the 2D material germanene [2] or standing-up Si nanowires [3] from the eutectic dropletx. Several of these eutectic systems have been studied by surface electron microscopy [4-10]. Information on the three—dimensional (3D) details of these liquid droplets, however, is rarely obtained from electron microscopy [11, 12]. Here we analyze the measured intensity profiles along the plane of incidence in order to reveal the 3D surface topography. We show that the local inclination is a crucial ingredient to reconstruct the surface topography from the photoemission intensity, using photo-electrons originating from both the surface and the thin bulk-like skin of the droplet. We obtain a very convincing simple fit to the observed intensity profiles of the photo-emitted electrons, which appears extremely sensitive to their local spatial distribution. This fact allows an absolute determination of the work function of the eutectic droplet.

3.2. EXPERIMENTAL DETAILS

EXPERIMENTS were performed using an Elmitec LEEM III with a base pressure below 1×10^{-10} mbar. 10 mm × 10 mm nominally flat, single-side-polished *n*-type Ge (110) crystals (MTI Corporation, $R > 50\ \Omega$ cm) have been degassed for about 24 hours at 700 K, followed by several cycles of Argon ion bombardment and flash annealing by e-beam bombardment at a temperature exceeding 1000 K. Subsequently, Pt is deposited from a resistively heated W wire wrapped with a high purity (99.995 %) Pt wire (Alfa Aesar). Photoemission electron microscopy (PEEM) measurements were performed using a 100 W mercury discharge lamp ($\lambda = 0.253\ \mu$m).

3.3. RESULTS

EXAMPLES of eutectic droplets exhibiting a spherical cap profile are shown in a PEEM image, see Fig. 3.1. The image shows eutectic PtGe droplets on a Ge(110) substrate. The image is a frame taken from a movie of the eutectic system at 50 K above the bulk eu-

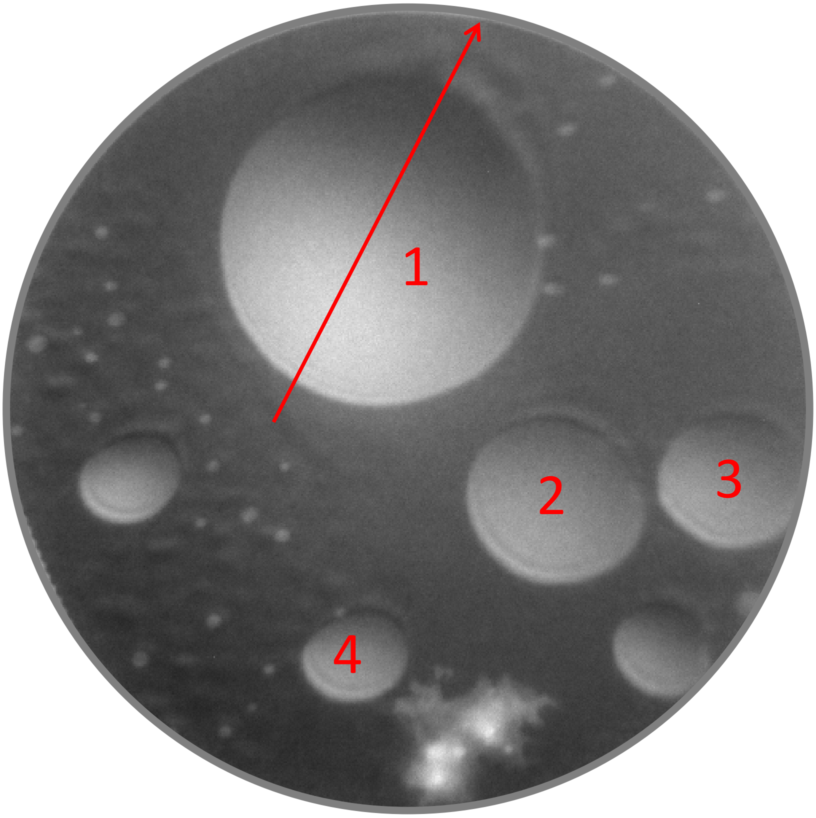

Figure 3.1: Frame from a PEEM movie showing eutectic PtGe droplets on Ge(110). Illumination direction is along the red arrow. Field of view is 150 m. The irregularly shaped bright feature next to droplet 4 is due to a defect in the microchannel plates of the detector.

tectic temperature of 1043 K. Prior to recording the movie, the system was driven through the eutectic transition to a maximum of 1150 K several times. In the image many smaller droplets are visible, next to a few larger ones with diameters ranging from 25 μm (droplet 4) to 60 μm (droplet 1). Above the eutectic temperature, the droplets move to the region with the highest temperature, which is near the center of this image. Droplet 1 is at the local hot spot, and is thus fully in equilibrium, while the other droplets are on their way to the hot spot. Such movement in the direction of the highest temperature has also been observed for the similar eutectic systems [4–10]. In the following sections we discuss important characteristics of the morphology of the eutectic PtGe droplets as revealed by PEEM.

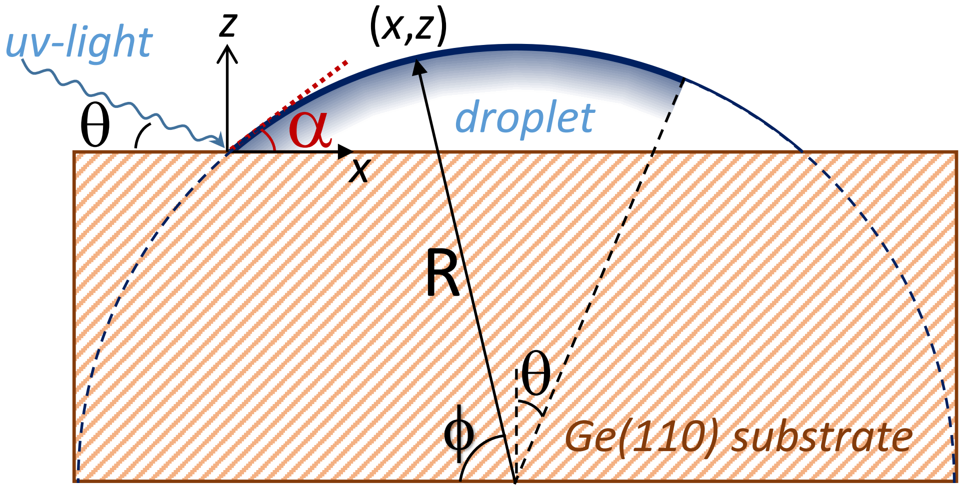

Figure 3.2: Profile of a spherical cap with radius R and a contact angle α of the eutectic PtGe droplet along the red line in Fig. 3.1 The illuminated part of the droplet-vacuum interface is indicated by the dark blue line. Photo-electrons originate also from a thin skin (fading blue rim).

3.3.1. INTENSITY PROFILE ACROSS THE DROPLET

First we discuss the PEEM intensity profile across the droplets. The PEEM images are obtained by collecting photo-electrons excited with a 4.9 eV ultraviolet beam, incident at a glancing angle $\theta = 16^\circ$ with the substrate. The emitted photo-electrons are captured along the substrate normal, yielding a top view of the droplets. We assume that the PtGe-droplet has the shape of a spherical cap, characterized by a radius of curvature R and a contact angle α. Fig. 3.2 shows a cross-section of the droplet profile along a plane parallel to the plane of incidence of the UV light, i.e. in the direction of the red arrow in Fig. 3.1. Any point (x, z) along this cross-sectional surface profile in Fig. 3.2 is given by

$$x = R(\sin\alpha - \cos\phi) \text{ and } z = R(\sin\phi - \cos\alpha), \tag{3.1}$$

for $90^\circ - \alpha \le \phi \le 90^\circ + \alpha$. This profile is illuminated by UV light for $90^\circ - \alpha \le \phi \le 90^\circ + \theta = 106^\circ$, since for ϕ values exceeding $90^\circ + \theta$ the corresponding parts of the droplet are in its shadow zone. For completeness we note that the exact shape of the droplet-substrate interface plays no role, because of the limited escape depth of the photo-electrons. Along the cross-section in Fig. 3.2 the local angle of incidence θ_l is given by

$$\theta_l = 90^\circ - (\phi - \theta), \tag{3.2}$$

again for $90^\circ - \alpha \leq \phi \leq 90^\circ + \theta = 106^\circ$. The local incoming photon flux I_l along the cross-section is then proportional to $C \sin\theta_l = \cos(\phi - \theta)$, with C a constant proportional to the photon density of the incoming beam. The emitted photo-electrons originate from the surface of the spherical cap (illustrated by the dark blue curve in Fig. 3.2) and also from a thin bulk-like skin of the sphere (illustrated in exaggeration by the fading blue rim in Fig. 3.2). The latter electrons have a reduced probability to reach the actual surface due to a finite attenuation length $\wedge$ [13, 14]. The value of $\wedge$ is 5.8 nm for 4.9 eV electrons, very close to the value for the inelastic mean free path for electrons of 4.9 eV [15]. We assume that this thin outermost layer is densely packed and we approximate the liquid as a homogeneous bulk with density ρ, taken equal to the atomic density of the Ge substrate, starting at a depth d_0 ($\sim$ 0.25 nm). The number of photo-emitted electrons N_e originating from this thin shell arriving at the surface is proportional to

$$N_e = \rho \int_{d_0}^{\infty} e^{-\frac{r}{\wedge \sin\phi}} \, dr = \rho \wedge \sin\phi \, e^{-\frac{d_0}{\wedge \sin\phi}}. \tag{3.3}$$

In order to contribute to the image, the photo-electrons have to overcome the work function Φ. The (local) normal component of their kinetic energy, E_n, has then to fulfill the condition: $E_n \geq \Phi$. Together with the curved vacuum-droplet interface, this leads to a peaked angular distribution of the escaping photo-electrons, F, which is approximated by

$$F(\beta) = \cos^m \beta = \sin^m \phi, \tag{3.4}$$

where β is the angle between the escape direction and the local surface normal and ϕ defined as in Fig. 3.2. The exponent m determines the sharpness of this distribution. A higher value of Φ, leads to a sharper peak profile of the angular distribution, and thus to a higher value of m. The intensity $I(\phi)$ of photo emitted electrons escaping from the droplet is then given by

$$I(\phi) = C \cos(\phi - \theta) \sin^m \phi \left(1 + \rho \wedge \sin\phi \, e^{-\frac{d_0}{\wedge \sin\phi}}\right), \tag{3.5}$$

The first term accounts for the contribution of the surface and the second term for that of the thin shell. For a given footprint diameter of the droplet, R and ϕ are completely determined by the contact angle α. The only remaining fitting variables in eq. (3.5) are thus α and m. The emitted photo-electron intensity $I(x)$ as a function of coordinate x, along the profile in Fig. 3.2 is given by $I(x) = I(\phi)\frac{d\phi}{dx} = \frac{I(\phi)}{R\sin\phi}$:

$$I(x) = C\cos(\phi-\theta)\sin^m\phi\left(\frac{1}{R\sin\phi}+\frac{\rho\wedge}{R}e^{-\frac{d_0}{\wedge\sin\phi}}\right) \tag{3.6}$$

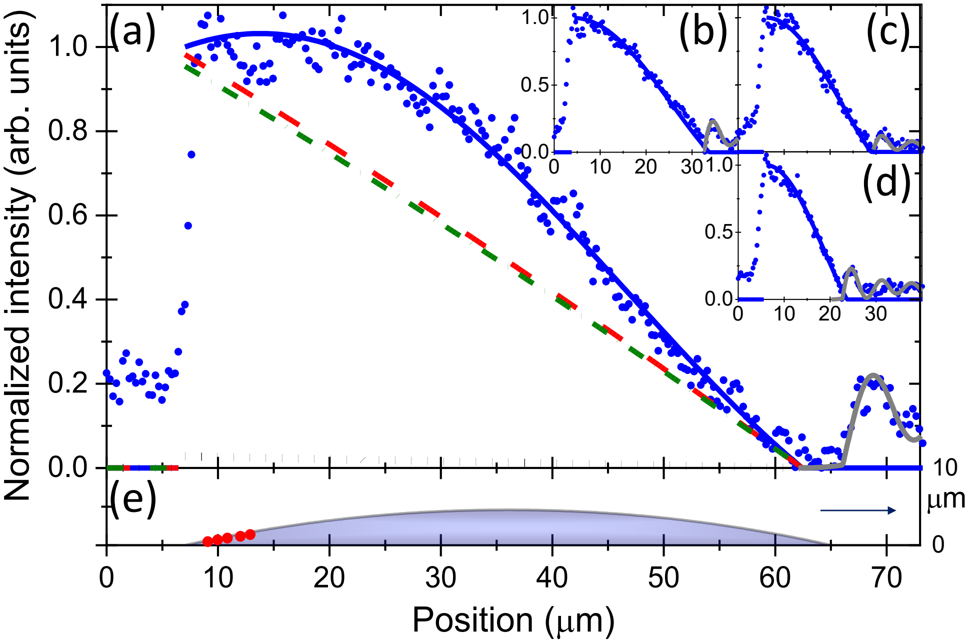

Figure 3.3: (a)-(d) Measured and calculated intensities along the optical plane of incidence through the droplets (1)-(4), respectively, in Fig. 3.1. The blue circles represent the experimental data, the solid blue lines are the fits using Eq. 3.6 with $\alpha = 20°$ and $m = 5.5$ in (a) and $\alpha = 18°$ and $m = 4.5$ in (b)-(d). The dotted black line and the dashed-dotted green line in (a) are the calculated contributions without the $\sin^m\phi$ term for the surface and the thin bulk like shell, respectively, with the red dashed line being their sum. The solid grey lines are calculations of the diffraction patterns behind the droplet (see text). (e) Cross sectional profile of droplet (1). The five red dots in the lower panel are experimentally determined points of the droplet's surface (see text).

In Fig. 3.3 we compare the measured intensities with fits to eq. (3.6). For the largest droplet (Fig. 3.3(a)) an excellent fit is obtained for $\alpha = 20° \pm 1°$ and $m = 5.5 \pm 0.5$. The value for m defines a profile with a FWHM of $56° \pm 2.5°$, which for 4.9 eV UV light leads to a work function of the eutectic droplet $\Phi = 4.9\cos^2(28 \pm 1.3)° = 3.8 \pm 0.1$ eV. The fitted profile is very sensitive to chances in the contact angle α and the value of . The size of the droplet in the profile is merely determined by the value of α. The size of the droplet can be accurately determined from the PEEM images, with an accuracy well within 1 μm. Variation of the contact angle α by 1 degree around the value of 20° determined in Fig. 3(a) results in a variation of about 1 μm in the length of the profile. We are thus able to extract value of α with an accuracy in the order of 1 degree. The value of the exponent m, is completely determined by the bulge of the profile. The dotted black and dash-dotted green lines in Fig. 3.3(a) represent the contributions from the surface and the thin bulk-like shell, respectively, without taking the peaked angular distribution of the escaping photo-electrons (given by eq. (3.4)) into account. The characteristic curvature in the intensity curves undoubtedly results from the angular distribution of the photo-electrons escaping from the curved droplet interface. For the smaller droplets in Fig 3.3(c)-(d) $\alpha = 18°$ and $m = 4.5$ (resulting in Φ= 3.6 eV) are used in the fits. Occasionally we observed eutectic droplets without a shadow zone (not shown here), in which cases we obtained a contact angle of 16° or lower from the fit to eq. (3.6). Note that variation of the finite electron attenuation length $\wedge$ or the atomic density ρ by an order of magnitude (which is rather unlikely) will not result in notable changes in the profiles in Fig 3.3.

3.3.2. RADIAL INTENSITY VARIATIONS ON THE ILLUMINATED DROPLET SIDE

A close inspection of the spatially resolved PEEM intensity of the eutectic droplets reveals a pattern of concentric rings on the illuminated sides of the eutectic droplets. These intensity variations are the result of standing waves through interference between the incoming plane wave at $\theta = 16°$ and the specularly reflected plane wave, as schematically shown in Fig. 5(a). Interference between incident and reflected waves yields standing waves with maxima and minima in the electromagnetic field responsible for excitation in the (near) surface regions of the droplets. The height z of successive nodal planes is given by $z = \frac{n\lambda}{2\sin\theta} = 0.459n$ μm, while for successive anti-nodal planes the height is given by $z = \frac{(n+\frac{1}{2})\lambda}{2\sin\theta} = 0.229(2n+1)$ μm, with $n = 0, 1, 2$ etc. Note that a possible phase shift at specular scattering, that would result in a shift of these planes along the normal, is disregarded. The phenomenon is very similar to observations in grazing incidence X-ray scattering [16] and has been discussed in terms of Lloyd's mirror [11,12].The presence of the planar sets of maxima and minima in the electromagnetic field enables probing of the shape of the illuminated side of the eutectic droplets. In Figure 5(b) and (c) we show radially averaged intensity profiles over the circle segments indicated in the insets, for droplets 1 and 2 in Fig. 2. Note that the gray scale values in the insets are set to optimize the contrast. From the maxima and minima of droplet 1 the coordinates of the droplet interface are extracted and displayed as red dots in Fig. 4(e). From this data we find a contact angle of 18° for droplet 1, slightly below the contact angle derived above from

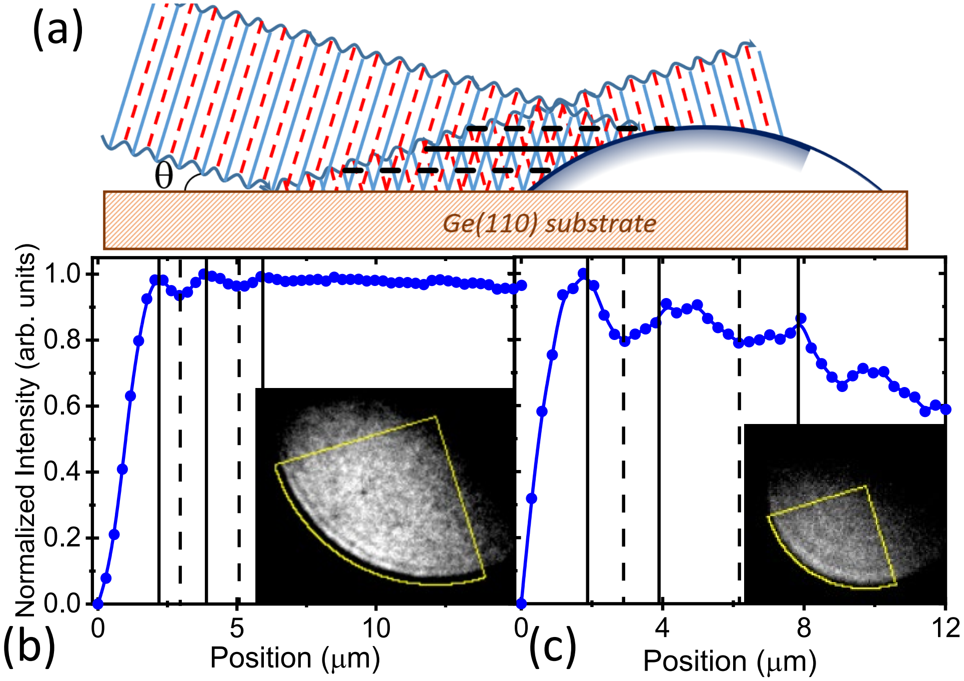

Figure 3.4: (a) Construction of the standing wave interference pattern of the photon intensity (see text). Solid and dashed lines correspond to, respectively, constructive and destructive interference. (b)-(c) Radially averaged intensity profile, obtained for droplets 1 and 2 from Fig. 2 and derived from the segments shown in the inserts representing the illuminated sides, as a function of distance from the leading edge. Again constructive and destructive interference are marked by solid and dashed lines.

the fit to eq. 6. For droplet 2 we find a contact angle of 14°, also slightly lower than the value derived above. For both droplets the first maximum and minimum are closer to each other than the other maxima and minima, which implies that directly at the edge the slope of the droplet vacuum-interface is steeper, leveling off further away from the edge.

3.3.3. INTENSITY VARIATIONS BEHIND THE DROPLETS

BEHIND the droplets in Fig. 3.2 we also observe corona-like intensity variations. These intensity variations are attributed to diffraction of the incoming plane wave by the droplet. Sommargren and Weaver [17] described a method to calculate the diffraction intensity on a screen perpendicular to the optical axis behind an opaque sphere, based on the evaluation of the first Rayleigh diffraction integral. The geometry for the eutectic PtGe droplets is sketched in Fig. 6. We have slightly modified their approach, in order to calculate the intensity profile at the surface behind the eutectic droplets. A point source is assumed at a distance d from the origin (in our case d is in the order of a meter). The origin is situated on the optical axis at a distance $e = R\sin\theta - R\tan(\cos\theta - \cos\alpha)$ away from the center axis of the spherical cap. The height a of the spherical cap in the direction of the UV illumination is given by $a = R\left(1 - \frac{\cos\alpha}{\cos\theta}\right)$. With $dl = ds\cos\theta$ and $dy = ds\sin\theta$ we can use the variables $v = ka\tan\theta$ (with $k = \frac{2\pi}{\lambda}$) and $u = \frac{ka^2}{s\cos\theta}$ to calculate the intensity I along s (for $s > e + \frac{a}{\sin\theta}$):

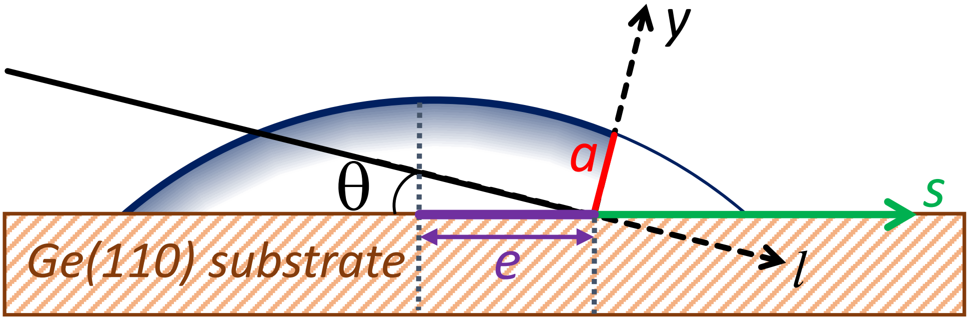

Figure 3.5: Schematic representation of the diffraction geometry. The solid/dashed black line l displays the optical axis of the problem. The droplet is treated as sphere with height a. The distance between the intersection point of the optical axis and the surface and the center axis of the spherical cap is e.

$$\begin{aligned} I(s) = & \frac{1}{(d + s\cos\theta)^2}\left(1 + U_1(u,v)^2 + U_2(u,v)^2\right. \\ & \left. - 2U_1(u,v)\sin\left(\frac{u^2+v^2}{2u}\right) + 2U_2(u,v)\cos\left(\frac{u^2+v^2}{2u}\right)\right), \end{aligned} \qquad (3.7)$$

with $U_n = \sum_{m=0}^{\infty}(-1)^m\left(\frac{u}{v}\right)^{n+2m} J_{n+2m}(v)$, where $J_{n+2m}(v)$ are integer order Bessel functions. The solid grey lines in Fig. 4 are calculated using Eq. 3.7, for droplet 1 with a contact angle of 17°, while for droplets (2)-(4) a contact angle of 18° was used, but the profiles have been shifted 6, 1 and 3 micrometer, respectively, towards the origin to match the experimental data, which also indicates that the actual contact angle is slightly lower than 18°.

3.4. DISCUSSION AND CONCLUSIONS

When comparing the three methods described above, the value obtained for the contact angle of droplet (1), at the hottest region of the surface, is for all three methods $19° \pm 1°$, while for droplets (2)-(4), that are on the move towards the hottest region, the variation in the obtained contact angle is slightly larger. We regard the fit of the droplet profile to the intensity data as the most reliable method, since in this method the datapoints from the entire droplet profile are used. In order to verify whether the larger variation in the value of the obtained contact angle for smaller droplets can be attributed to a more advancing or receding character of the contact angle, we showing in Fig. 3.6 the measured intensities along two equally large droplets which are illuminated from the advancing (red pluses) and receding droplet side (blue crosses) and the resulting fits using Eq. 6. The profiles and the fits are almost indistinguishable, indicating that there is, within our reliability limits,no detectable difference between advancing and receding contact angle. The droplet shape is thus exclusively determined by thermodynamics and contact angle dynamics play no noticeable role.

From the methods described above, the intensity variations at the illuminated side of the droplets have been discussed in terms of Lloyd's fringe contrast [11, 12] for the case of Ga droplets on GaAs(001). For the Ga/GaAs(001) system up to 8 almost equidistant intensity maxima were observed over a distance of 10 μm, which, following our approach described above, results in a contact angle of 20°. Using the whole intensity profile in an iterative procedure, which takes into account the influence of the local variations in the electric field due to the nonuniform surface topography, a contact angle of 22° was deduced [11, 12]. In our case, with only 3 intensity maxima, such an iterative refinement will not increase the accuracy of our contact angle determination.

To assess the obtained work function value, we performed LEEM $I(V)$ measurements on the eutectic droplets and the neighboring environment, as well as on the pristine clean Ge(110) surface, see Fig. 7. In the LEEM $I(V)$ measurements a well-defined steep drop in the reflectivity occurs when the electron beam starts to interact with the unoccupied states in the sample surface. The start voltage position of this steep intensity drop reflects the (local) sample's work function. Using a work function of 4.5 eV for Ge(110) [18], we find by fitting a sigmoid to the measured $I(V)$ curves, a work function of 3.6 eV for the eutectic droplets, which is similar to the estimation from the peaked distribution of photo-electron intensity above. For the area around the eutectic droplets we find a work function of 4.0 eV, which explains why the eutectic droplets appear brighter than

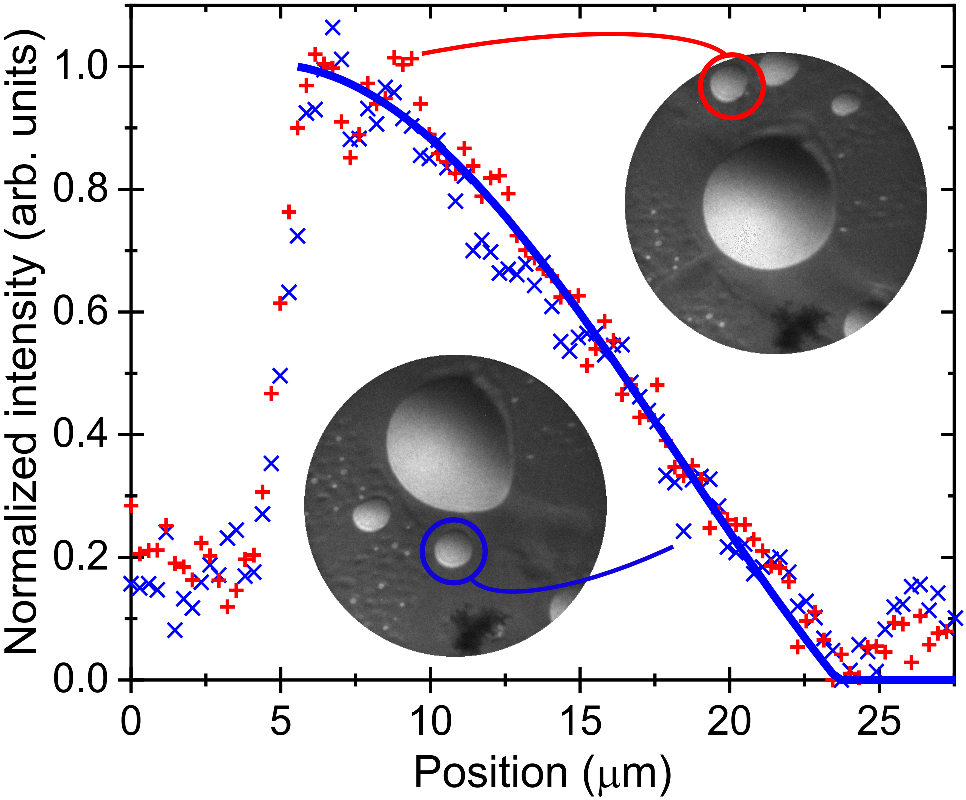

Figure 3.6: Measured and calculated intensities along the optical plane of incidence through the droplets encircled in the insets. The blue crosses represent the experimental data for the droplet encircled in the left inset, which is illuminated from the receding side. The red plusses represent the data for the droplet in the right inset, which is illuminated from the advancing side. The solid blue lines, which are virtually identical, are the fits using Eq. 3.6 with $\alpha = 16.3°$ and $m = 4.5$.

the neighboring area in Fig. 2.

In conclusion, we analyzed the shape of Pt-Ge eutectic droplets using PEEM. The surface topography is obtained from a fit to the emission profile, using only the workfunction and the contact angle as parameters. The intensity profile consists of two components, a small contribution from the surface and a much larger contribution from a thin bulk-like skin of the droplet. The characteristic curvature in the emission profiles is a direct consequence of the angular distribution of the generated photo-electrons in combination with the curved droplet's surface. The contact angle extracted from the emission profile is in agreement with contact angle values derived from both maxima

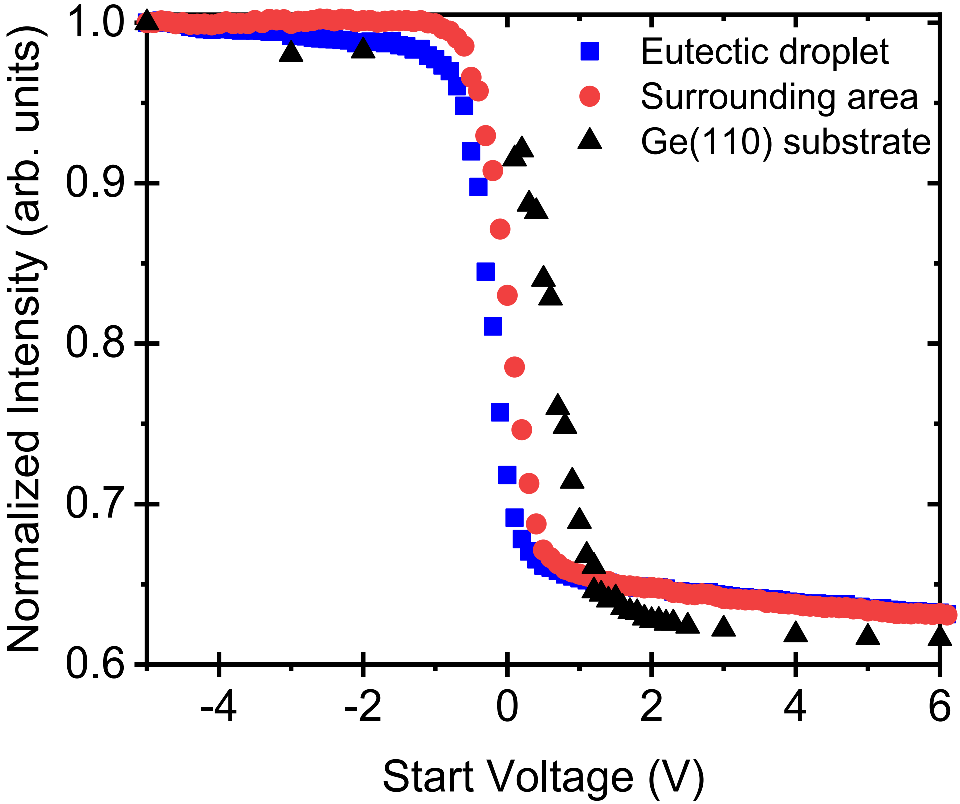

Figure 3.7: LEEM I(V) measurements obtained on an eutectic droplet (blue squares), the surrounding area (red circles) and a pristine Ge(110) surface.

and minima in the emission intensity on the illuminated side of the droplets. Simulation of the diffraction pattern behind the eutectic PtGe droplets results also in very similar values for the contact angle. These methods allow a very precise determination of the shape of 3D from PEEM images, together with an estimate of the droplets' work function, which corresponds to the workfunction obtained from LEEM $I(V)$ measurements. Our methods are generically applicable to other droplets too.

BIBLIOGRAPHY

[1] J. H. Snoeijer and B. Andreotti, Annu. Rev. Fluid Mech. **45**, 269-292 (2013).

[2] P. Bampoulis, L. Zhang, A. Safeai, R. van Gastel, B. Poelsema and H.J.W. Zandvliet, J. Phys.: Condens. Matter **26**, 442001 (2014).

[3] S. Kodambaka, J. Tersoff, M. C. Reuter, and F. M. Ross, Science **316**, 729 (2007).

[4] W.-C. Yang, H. Ade, and R. J. Nemanich, Phys. Rev. B **69**, 045421 (2004).

[5] P.A. Bennett, J. Chobanian, J.I. Flege, E. Sutter and P. Sutter, Phys. Rev. B **76**, 125410 (2007).

[6] P. Sutter, P.A. Bennett, J.I. Flege and E. Sutter, Phys. Rev. Lett. **99**, 125504 (2007).

[7] A. El-Barraj, S. Curiotto, F. Cheynis, P. Müller and F. Leroy, Appl. Surf. Sci. **509**, 144667 (2020).

[8] S. Curiotto , F. Leroy, F. Cheynis and P. Müller, Sci. Rep. **7**, 902 (2017).

[9] B.H. Stenger, A.L. Dorsett, J.H. Miller, E.M. Russell, C.A. Gabris and S. Chiang, Ultramicroscopy **183**, 72 (2017).

[10] F. Leroy , A. El Barraj, F. Cheynis, P. Müller and S. Curiotto, Phys. Rev. Lett. **123**, 176101 (2019).

[11] D.E. Jesson, K.M. Pavlov, M.J. Morgan and B.F. Usher, Phys. Rev. Lett. **99**, 016103 (2007).

[12] W.X. Tang, D.E. Jesson, K.M. Pavlov, M.J. Morgan and B.F. Usher, J. Phys.: Condens. Matter **21**, 314022 (2009).

[13] A. Jablonski and C.J. Powell, J. Electron Spectrosc. Relat. Phenom. **100**, 137 (1999).

[14] W.S.M Werner, Surf. Interface Anal. **1**, 2 (1979).

[15] M.P. Seah and W.A. Dench, Surf. Interface Anal. **31**, 141 (2001).

[16] M. J. Bedzyk, G.M. Bommarito and J.S. Schildkraut, Phys. Rev. Lett. **62**, 1376 (1989).

[17] G. E. Sommargren and H.J. Weaver, Appl. Opt. **29**, 4646 (1990).

[18] B. Borca, C. Castenmiller, M. Tsvetanova, K. Sotthewes, A.N. Rudenko and H.J.W. Zandvliet, 2D Materials **7**, 035021 (2020).

4

SHINING NEW LIGHT ON THE MOTION OF DROPLETS ACROSS SURFACES: A PEEM STUDY OF PTGE ON GE(110)

This chapter is published as B. Poelsema, Z. Zhang, J.S. Solomon, H. J.W. Zandvliet and A. van Houselt, *Shining new light on the motion of droplets across surfaces: a PEEM study of PtGe on Ge(110)*, Phys. Rev. Materials **5**, 125602 (2021).

ABSTRACT Thermally stimulated motion of micron sized eutectic PtGe droplets on Ge(110) has been studied in-situ by mainly PEEM (Photo Emission Electron Microscopy), LEEM (Low Energy Electron Microscopy) and μLEED (spatially resolved Low Energy Electron Diffraction). In line with earlier studies of eutectic AuSi-, PtSi-, AuGe- and PtGe-clusters on, respectively, various Si- and Ge-substrates we find that the motion toward regions at higher temperature is driven by the entropy gain of substrate atoms which become constituents of the droplet during its journey. At ~ 1100K, i.e. well above the bulk eutectic temperature the direction is governed solely by the local thermal gradient, irrespective of eventual crystalline preferences. Access to the diffusivity of the host material (in this case Ge) inside the eutectic droplets shows that this is well above one order of magnitude higher than expected if it was rate limiting for the velocity of the moving droplets. This excludes a significant gradient of the (Ge-) concentration inside the droplet and disqualifies dissolution-diffusion-deposition flow as the driving force for motion of the droplets on the surface as assumed widely hitherto to explain surface diffusion of eutectic droplets on surfaces. In addition, the interface between the droplet and the surface appears flat and we find no indication for “endotaxy”. The droplets make direct contact with the flat Ge substrate through atomic steps, which are abundantly present at the interface. The droplets are surrounded by a $PtGe_3$ wetting layer with an ordered (2x1) structure. Dissolution of the edges of the wetting layer at the leading edge of the droplet with an activation energy of 2.2 eV is identified as the rate limiting step for its motion.

4.1. INTRODUCTION

THE motion of metal containing eutectic droplets inside a Si crystal subjected to a strong thermal gradient has been studied in detail by Cline and Anthony [1]. The droplets move toward higher temperature within the host material (Si). Subsequently, Si dissolves at the advancing side, diffuses through the eutectic and is expelled and redeposited at the receding side. The migration speed was found to increase substantially at temperatures far above the eutectic temperature due to higher atomic percentages of the host material inside the droplet. Considerable attention has been paid to the dynamics of metallic droplets on surfaces since then. This includes the motion of Ga droplets on GaAs under incongruent evaporation conditions [2,3], thermomigration of PtSi droplets on stepped Si(111) and Si(100) [4-6], AuSi- and AuGe- droplets on various Si and Ge substrates [7,8], AuGe on Ge(110) [9] and recently, electromigration of AuGe [10]. The surface studies were motivated by interest in possibilities for bottom up fabrication of nanostructures, catalysis of standing up [11] and lying down nanowires [12,13] on surfaces and, last but not least, genuine interest in the complex physics of the motion of metallic droplets on surfaces. Although consensus is emerging on the role of the gain of entropy when the droplets travel toward hotter regions on the surface as the driving force for droplet mobility, many questions remain still open, such as: - the exact role of the atomic steps at the surface, - the nature of the enhanced uniform morphology in the wake, i.e. in the trail behind the moving droplet, - the morphology of the interface between the spherical droplet segments and the hosting surface and - the directionality and velocity of the mobile droplet segment and their influence on the size of the droplets. It is generally accepted that during their motion the droplets stay at the liquidus line and are in thermal equilibrium with the substrate. The current, quite commonly accepted, notion is that the diffusivity of the host material inside the eutectic droplets is rate limiting for their diffusion speed on the surface [4,5,6,9].

In our present contribution for micron-sized droplets on Ge(110) we critically evaluate the applicability of the Cline-Anthony (dissolution-diffusion-repulsion) mechanism for surface diffusion. We find no evidence for a driving role of atomic steps in the droplet motion. Moreover, most importantly, we find no indication at all for a linear dependence of the diffusion speed on the local thermal gradient at the surface as required in the Cline-Anthony model for particles with a constant size. We find clear evidence that the dissolution of the wetting layer at the leading edge of the droplet is the rate limiting step of the motion of the droplet.

4.2. EXPERIMENTAL

THE PEEM/LEEM experiments have been carried out with an Elmitec LEEMIII instrument with a base pressure of 10^{-10} mbar. In PEEM, the surface was illuminated with a 100 W mercury discharge lamp (λ = 0.253 μm) incident at 16° from the surface plane. The absolute temperature reading is estimated to be correct within ca. 25 K and calibrated by making the highly reasonable assumption that the eutectic temperature at the surface equals that of the bulk (1050 K for GePt). A Ge(110) substrate, 10 mm × 10 mm nominally flat, single-side-polished n-type Ge (110) crystals (MTI Corporation, $R > 50\Omega$ cm) has been degassed for about 24 hours at 700 K, followed by several cycles of Argon ion bombardment and flash annealing by e-beam bombardment at a temperature exceeding 1000 K. Subsequently, Pt is deposited from a resistively heated W wire wrapped with high purity (99.995 %) Pt (Alfa Aesar). The surface structure has been examined using LEED. Similar to the findings in ref. 14, we also observed a $c(8\times10)$ structure at lower substrate temperatures, while above the Ge-Pt eutectic temperature, only the non-reconstructed (1×1) structure is observed. With the sample kept at high temperatures for many hours a photo image has been obtained and from the spatial color distribution the temperature distribution is determined assuming black body radiation. The resulting temperature profile of the surface is shown in Fig. 4.1. The temperature is maximal in the centre and falls off about 50 K toward the edges due to, mainly, heat conduction to the sample holder. This results into modest but persistent temperature gradients even quite close to the centre of the substrate.

In the relevant area, the obtained temperature profile closely follows a paraboloid with $T(K) = 1100 - 0.9r^2$ with r (mm) being the distance from the center. Obviously, the temperature gradient increases linearly with r.

4.3. RESULTS

AN amount equivalent to about five monolayers of Pt has been deposited with the Ge(110) substrate held at room temperature. Following this exposure the crystal was heated slowly for several hours until a steady state set in with a maximum temperature of ~ 1100 K. Upon passing the eutectic temperature during heating a phase transition is observed in which the GePt clusters become liquid and get brighter than their environment in PEEM images. Some of the larger droplets become mobile. Let us now consider the scenario for the motion of individual eutectic droplets in more detail. For

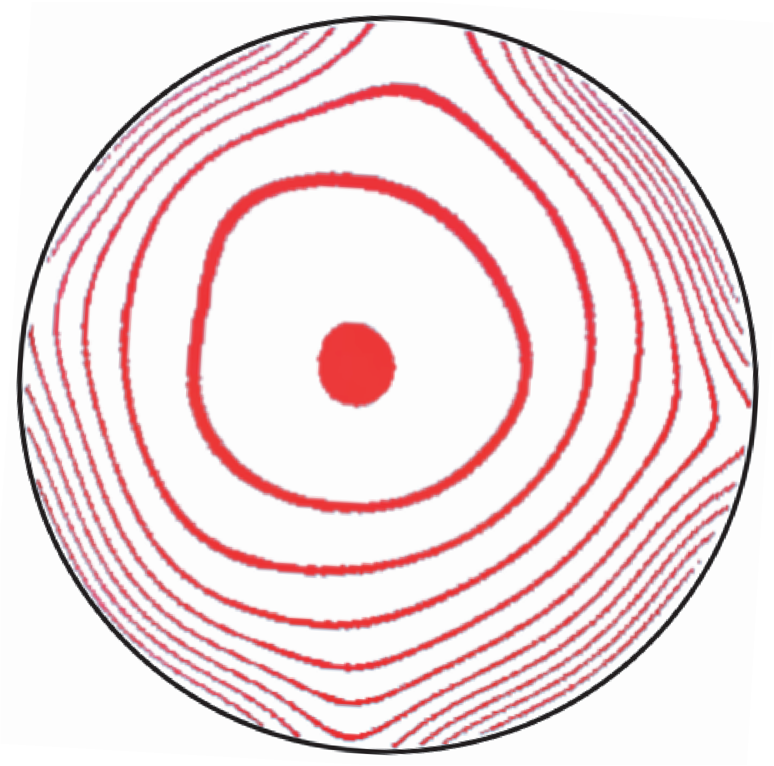

Figure 4.1: Contour map of the isotherms on the Ge(110) substrate with a diameter of 7 mm. The distance between the isotherms is 7 K and the maximum temperature in the centre is ~ 1100 K.

this purpose we seek guidance by the bulk phase diagram for Ge-Pt. The Ge-rich part of the phase diagram [15] has been reproduced in Fig. 4.2(a). Upon heating, the first eutectic solution emerges at 1050 K. Above the eutectic temperature the droplet is in equilibrium with the supporting Ge(110) substrate. The shape and position of the liquidus line in the phase diagram provide information on the composition of the eutectic solution and the latent heat as a function of temperature.Let us consider a GePt droplet in equilibrium with the supporting Ge(110) substrate. The droplet – substrate combination consists of a constant number of particles at a constant pressure. Then Maxwell's equation $(\frac{\partial G}{\partial T})_{N,P}$ = -S dictates that the total Gibbs free energy for this system decreases with increasing temperature. As a consequence, the droplet moves toward the location with the highest temperature in the presence of a temperature gradient at the surface. During its trip the droplet, with a constant number of Pt-atoms, accommodates additional Ge atoms originating from the substrate in order to keep fulfilling the composition condition imposed by the liquidus line (red curve in Fig. 4.2a).

The Gibbs free energy g of a Ge atom in either the crystalline substrate or the liquid phase is by definition:

$$g_{x,l} = h_{x,l} - Ts_{x,l} \tag{4.1}$$

where the subscripts, x and l, refer to the crystalline and the liquid phase, respectively, h is the enthalpy, s is the entropy, both per Ge atom and T the temperature. The Gibbs free energy per atom in the eutectic droplet also depends on the fraction of Ge atoms in the eutectic droplet (θ) [16],

$$g_l(T,\theta) = g_l(T) - \Delta g_{mix}(T,\theta) \tag{4.2}$$

where the $\Delta g_{mix}(T,\theta)$ is the mixing Gibbs free energy per Ge atom. In equilibrium, the Gibbs free energies per Ge atom in the crystalline phase and the eutectic droplet are the same, i.e. $g_x(T) = g_l(T,\theta)$. This means that in our system we have

$$g_x(T) \neq g_l(T) \tag{4.3}$$

The Ge-particle currents from the substrate to the eutectic droplet and vice versa are then by definition given by

$$j_{x\to l} = cn_x \exp\left[\frac{-(g_b - g_x)}{k_B T}\right] \text{ and } j_{l\to x} = cn_l \exp\left[\frac{-(g_b - g_l)}{k_B T}\right] \tag{4.4}$$

where $n_{x,l}$ refer to the Ge concentrations in the respective phases, g_b is the activation barrier and c is a constant. With a relative density of Ge in the substrate equal to 1 and that of Ge in the droplet θ_{Ge} given by:

$$\theta_{Ge} = \frac{n_l}{n_l + n_{l,Pt}} \tag{4.5}$$

with $n_{l,Pt}$ is the atomic concentration of Pt in the droplet one obtains in equilibrium between droplet and substrate:

$$j_{x\to l} = j_{l\to x}, \text{ or } \exp\left(\frac{g_x}{k_B T}\right) = \theta_{Ge} \exp\left(\frac{g_l}{k_B T}\right), \text{ or } \ln\theta_{Ge} = \frac{-\Delta g}{k_B T} \tag{4.6}$$

All expressions are exact. In an attempt to acquire some more insight we apply Eq. 4.1 and rewrite Eq. 4.6:

$$\ln\theta_{Ge} = \frac{\Delta h}{k_B T} - \frac{\Delta s}{k_B} \tag{4.7}$$

From a conventional analysis, i.e. from a plot of $\ln\theta_{Ge}$ versus $1/k_B T$, one derives naively Δh_m as a function of θ_{Ge}. The result is shown in Fig. 4.2b, which reveals a strong decay of the melting enthalpy with decreasing Ge content. However, a hidden T-dependence in the entropy term inevitably leads to an incorrect result for the melting enthalpy. In the limit of large Ge concentrations, i.e. close to the Ge melting temperature, the melting entropy obtained from Eq. 4.7 with Δs is temperature independent, is correct in very good approximation, i.e. $\Delta h_m = 0.383$ eV per atom. We cannot obtain more detailed information from the data in Fig. 4.2b without more specific and independent knowledge of the temperature (or coverage) dependence of either Δh_m, or Δs_m.

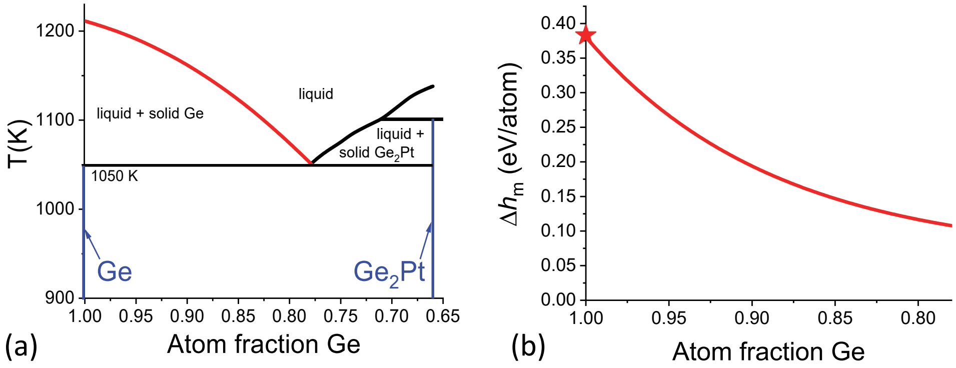

Figure 4.2: (a) The high Ge content part of the GePt bulk phase diagram. At the eutectic temperature at 1050 K a eutectic phase, with a 78-22 atomic percent Ge-Pt ratio, is formed in contact with pure Ge and Ge_2Pt. During the experiments the system moves along the red liquidus curve. Data replotted from [15]. (b) Latent heat of Ge atoms within the eutectic droplet versus the atomic fraction of Ge within the droplet. The asterisk indicates the latent heat of pure Ge.

The total latent heat of a droplet with a fixed number of Pt-atoms, traveling from colder to a hotter position thus increases for two reasons: 1) an increasing latent heat per atom and 2) an increasing number of Ge atoms within the droplet. As a result the eutectic droplet experiences a strong incentive to move toward the hottest position at the surface. The effect is present all along the surface and is stronger when operating closer to the melting point of pure Ge [1]. We estimate that in our current experiments the surfed temperature range is around 50 K above the eutectic temperature.

The driving force *per Pt-atom* in the droplet for motion toward hotter positions is identical and does not depend on the droplet size, since the latter scales one-to-one with the number of Pt-atoms inside the droplet. We note that the (extreme) Ge-rich part

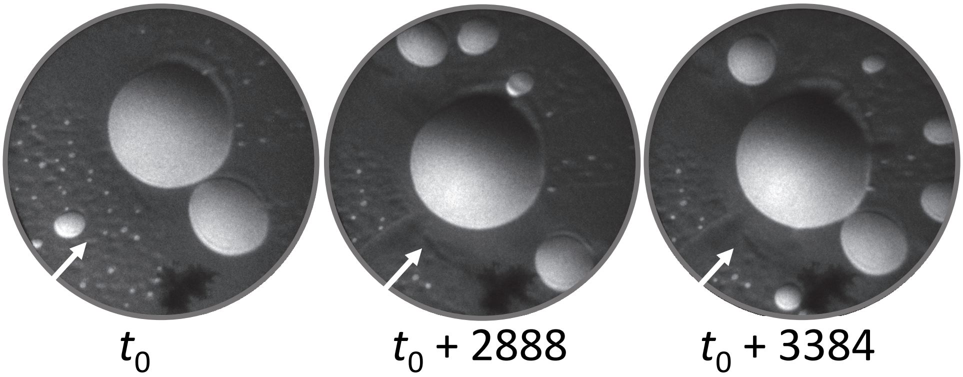

t_0 $t_0 + 2888$ $t_0 + 3384$

Figure 4.3: Snapshots of PEEM movie (1100 K) [17], taken close to the centre of the surface at an advanced stage during in a thermal steady state situation, at different points in time after the arbitrary point in time in the right hand image (time in s). Field of View is 150m. The bright eutectic droplets are illuminated along the direction indicated by the white arrows. They represent spherical caps with a wetting angle of 18° [18]. The dark feature near the bottom is a defect in the channelplate.

of the bulk phase diagram is relevant for the current situation of a eutectic droplet in contact with a pure Ge substrate. The liquidus line represents the equilibrium between the eutectic and mainly the pure Ge solid. As argued above, the eutectic droplets all move toward the centre, i.e. the highest temperature location (cf. Fig. 4.1), of the surface when thermodynamic equilibrium between the substrate and the individual spherical droplets has set in. The final ideal situation would lead to one huge droplet in the centre, growing mainly due to coalescence with arriving smaller droplets. The latter move in a radial fashion toward the centre and, for geometrical reasons, the rate of coalescence is high(est) near the centre. Indeed we have identified such behavior. As evidence we refer to an illustrative movie [17]. A few frames obtained near the substrate centre are displayed in Fig. 4.3. The bright objects are, irrespective of their lateral size, spherical segments (caps) of eutectic PtGe droplets. They appear bright in these PEEM images due to a, compared to their surroundings, slightly lower work-function. Their wetting angle is about 18° and the incident UV light is directed along the azimuth indicated by white arrows. The brightness profile of the droplets is understood in detail as described in Ref. 18. In short, the wetting angle has been obtained from both the PEEM intensity profile of the droplet, as well as the position of the interference fringes of the direct and the specularly reflected light on the illuminated side of the droplet. The surface morphology is quite heterogeneous as the environment around the large droplets appears pretty featureless, in contrast to the surroundings of the small objects. The smallest objects are sessile eutectic droplets and all other ones move toward the large droplet residing in the centre and eventually all would merge and finally constitute a huge eutectic droplet with a Ge content that corresponds to the reigning temperature and given by the liquidus line in Fig. 4.1. It is estimated that droplets with a diameter less than about 2-3 μm remain immobile under the current conditions. The latter behavior has been observed previously for the related PtSi/Si(100) system too by Yang *et al.* [4].

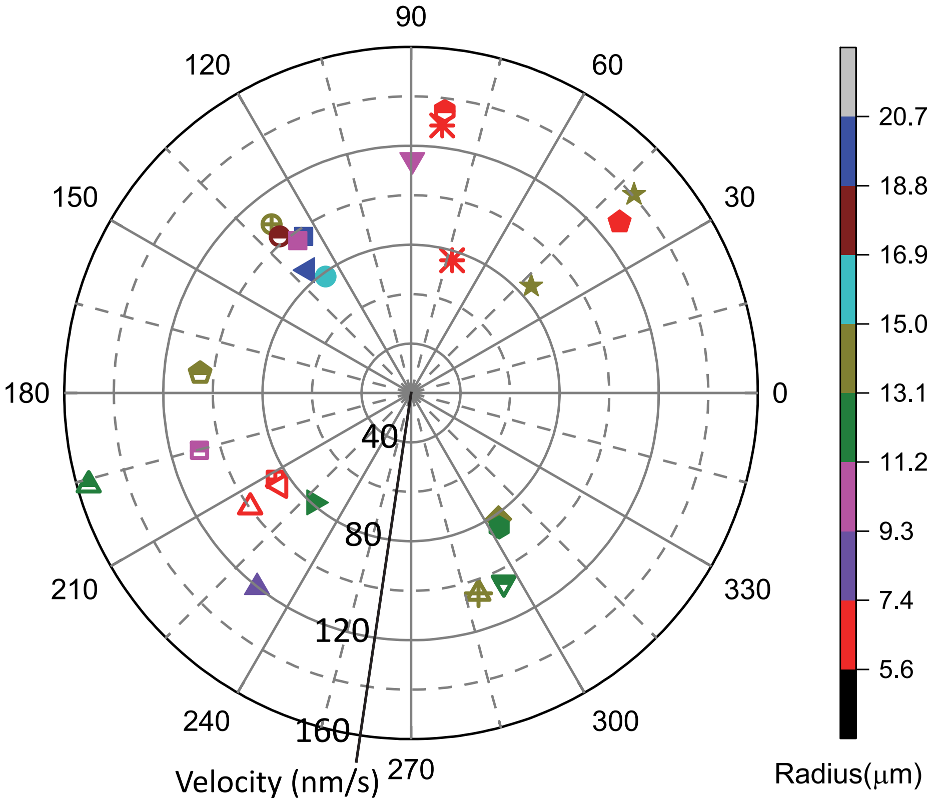

Figure 4.4: Polar diagram of the moving droplets. The radius denotes their velocity in nm/s (left scale) and the (arbitrary) azimuth their direction of motion. A given point on the negative horizontal axis would thus represent a droplet traveling from right to left toward the hottest spot. The colors refer to the droplet size (right scale). The substrate temperature was 1100 K. Each symbol represents a different droplet.

Next we consider eventual crystalline preferences for the direction of motion for the moving droplets. The result for some 30 eutectic droplets is summarized in Fig. 4.4. It exhibits a polar plot of the direction and the magnitude of the velocity of the moving droplets. Any data point situated in the first quadrant represents a motion from globally bottom left to the centre at a velocity given by the radius (left hand scale in nm/s). The colors represent the size of the particular objects (right hand scale, radius in μm). The final large droplet and the sessile small droplets are not included in the plot.

The data do not reveal any correspondence between the velocity and the droplet size. Moreover, the data shows no preference for any azimuth at this surface with its two-dimensional symmetry. These observations lead unequivocally to two conclusions: 1) The motion is driven by solely by the direction of the local temperature gradient and 2) the twofold crystalline anisotropy plays no role. These facts both disqualify the anisotropy of Ge dissolution kinetics at atomic steps as the driving force for the droplet motion as was suggested in Ref. 18. for the motion of AuSi droplets on Si(111). In addition, it is noted that the obtained velocities of roughly 70-130 nm/s are right in the ballpark of literature values found for moving eutectic droplets on varies surfaces [4-6,8-10,18-19] and further that no distinct relation between the size and the velocity is observed. The latter is in line with several earlier reports too [4-6].

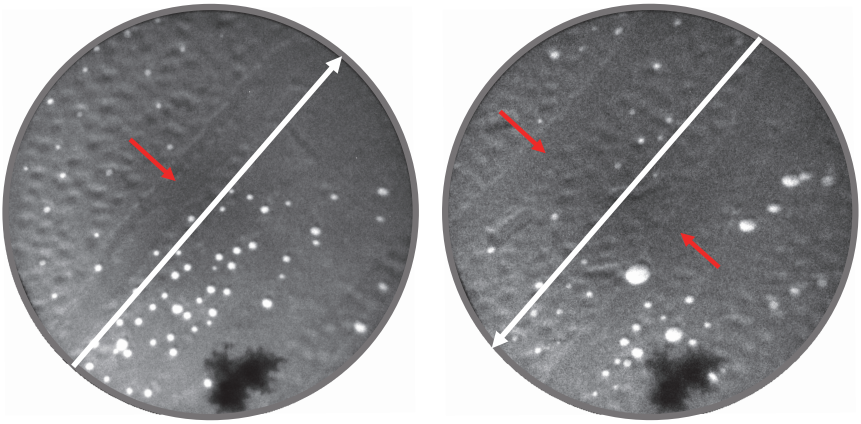

Figure 4.5: Snapshots from a movie representative of the motion of droplets “far” away from the centre. In both images the manipulator was moved in such a way that the centre moved out the field of view along the direction of the white arrow; in the left hand case almost 1 mm and in the right hand case by about 0.5 mm. Small sessile droplets reside in areas that look quite heterogeneous. Note that in PEEM one images the local work function and the heterogeneity could be caused by either roughness, composition or a combination of both. The larger droplets still move under the influence of a thermal gradient and move along the direction of the arrows. They leave behind trails with a much more homogeneous appearance and a few are marked with red arrows. Moving droplets have a strong tendency to follow fresh trails. This can also be observed in the movie [17]. The Field of View is 150 micron and the temperature is 1100 K.

The motion of droplets driven by the thermal gradient is highly complex. This is caused in part by the lack of homogeneity on the surface as is apparent from Figs. 4.3 and 4.5. In the left and right hand panel of Fig. 4.5 the field of view is displaced by, respectively, about 1 mm and 0.5 mm in the direction opposite to that of the white arrows. The sessile small droplets with a diameter of about 2-3 μm or less remain immobile in an environment with a heterogeneous work function as concluded from the varying local brightness. Note that in PEEM the contrast results predominantly from differences in work function and not purely from height variations. The motion is oriented toward the centre, i.e. it follows a positive local temperature gradient to the maximum at the centre. The “wakes” of the passing droplets (a few are indicated by red arrows) appear substantially more homogeneous when compared to their environment. Also a strong tendency to follow the wakes of earlier passing droplets is observed. This happens at a higher velocity than that of the pioneering droplets distinctly more slowly finding their way through the heterogeneous areas. This behavior is also apparent in the movie [17] underlying Figs. 4.3 and 4.4.

The actual situation may even be further complicated by left-over traces from previous experiments. An illustration is shown in Fig. 6, where the currently prevailing motion is from left to right at an angle of about -30°. A remainder of a trail (wake) of a moving droplet in an earlier experiment is pointed at by the dashed red arrow. We cannot conclude on its direction of motion: it was probably from left to right, but could have been from right to left.

Obviously again, the motion of the eutectic droplet is a complicated process, which is moreover hard to define exactly due to heterogeneities at the surface, which are inherent to the (current and previous) Pt deposition and heating experiments. That fact prevents us from performing systematic temperature dependent measurements of the velocity to gain information on activation energies.

We emphasize that the speed of the moving droplets does not depend on the magnitude of the local temperature gradient. This finding is highly relevant and in line with the results of studies of similar systems [5] and will be rationalized as the first item in the discussion and conclusion section below.

Almost all studies dealing with the velocity of eutectic droplets in the presence of a temperature gradient adopt the bulk based model put forward by Cline and Anthony [1]. They find for the migration velocity v(T) of a liquid eutectic droplet at a temperature T

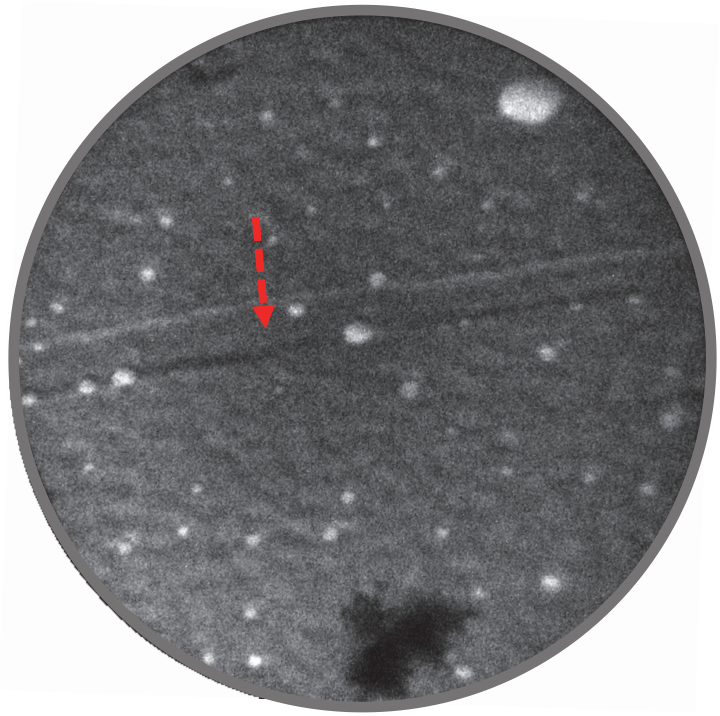

Figure 4.6: A snapshot from a different position at the surface, in this case about a few tenths of a mm left of the centre. The dashed arrow refers to a trace left from an earlier experiment (see text).

the following expression:

$$v(T) = \frac{D(T)}{1 - X(T)} \cdot \left(\frac{\partial X}{\partial T}\right) \cdot \nabla T \tag{4.8}$$

with D(T) the diffusivity of the host material (in our case Ge) inside the droplet, X(T) is the normalized alloy fraction along the liquidus line and is the temperature gradient. X(T) approaches 1 when the guest component (in our case Pt) inside the droplet becomes negligible compared to the host component. The migration velocity was found about constant even if the volume of the droplets is changed by three orders of magnitude. In others words the migration speed of the eutectic droplets does not depend on the size, which is probably the reason for the surprising and remarkable popularity of this bulk model for explaining migration rates of the on surfaces. Assuming that this model indeed holds for droplets on surfaces too, we note that a decrease of near the centre goes along with a higher X(T) value. In all cases we stay well below the melting temperature and a variation of (1-X(T)) by two orders is way off limits. The independence of the velocity of the moving droplets on the thermal gradient as noted in the previous paragraph still remains to be understood.

We now address the motion of single droplets as well as their mergence in much more detail. In the current experiment a large droplet moves from left to right in Fig. 4.7. It does so slowly, because it is held up while "consuming" all the smaller, sessile droplets on its way. A movie is added to illustrate this behavior [21]. The wake of this huge droplet appears remarkably homogeneous, i.e. much more so than is the case in the wider surroundings. The same is true for the trails left behind by the smaller moving droplets without exception. A similar observation was reported earlier [4,6] for motion of eutectic droplets in a similar systems. To rationalize this observation one may assume that the eutectic droplets move on non-reconstructed areas of the Ge(110) surface. Note that for the clean surface, i.e. in the absence of deposited Pt, the (1x1) structure is observed at the elevated temperature, 1100 K, maintained here. This is evidenced by Fig. 4.8a.

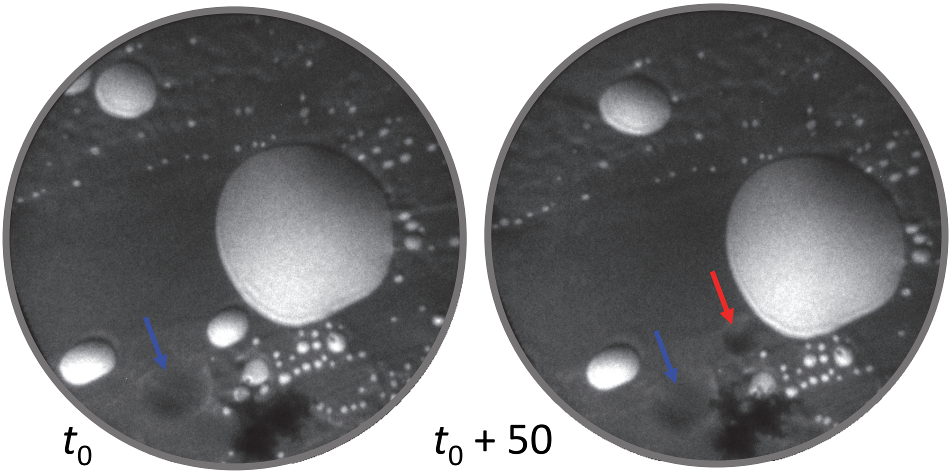

Figure 4.7: PEEM images from a movie (1100 K) in a different experiment on another Ge(110) surface; FoV 150 μm. The images show evidence for the remainder of trails from moving droplets in a previous experiment. This is the reason for the appearance of sets of small droplets heading from left to right. Their alignment is caused by the sweep of passing droplets in an earlier experiment. We observe several trails. Left: just before the coalescence of a small droplet with the large one. Right: just after coalescence with the red arrow marking a left behind footprint. The blue arrows marks a footprint left behind in an earlier coalescence event.

It shows the diffraction pattern taken with 30 eV electrons shows the extinct peaks

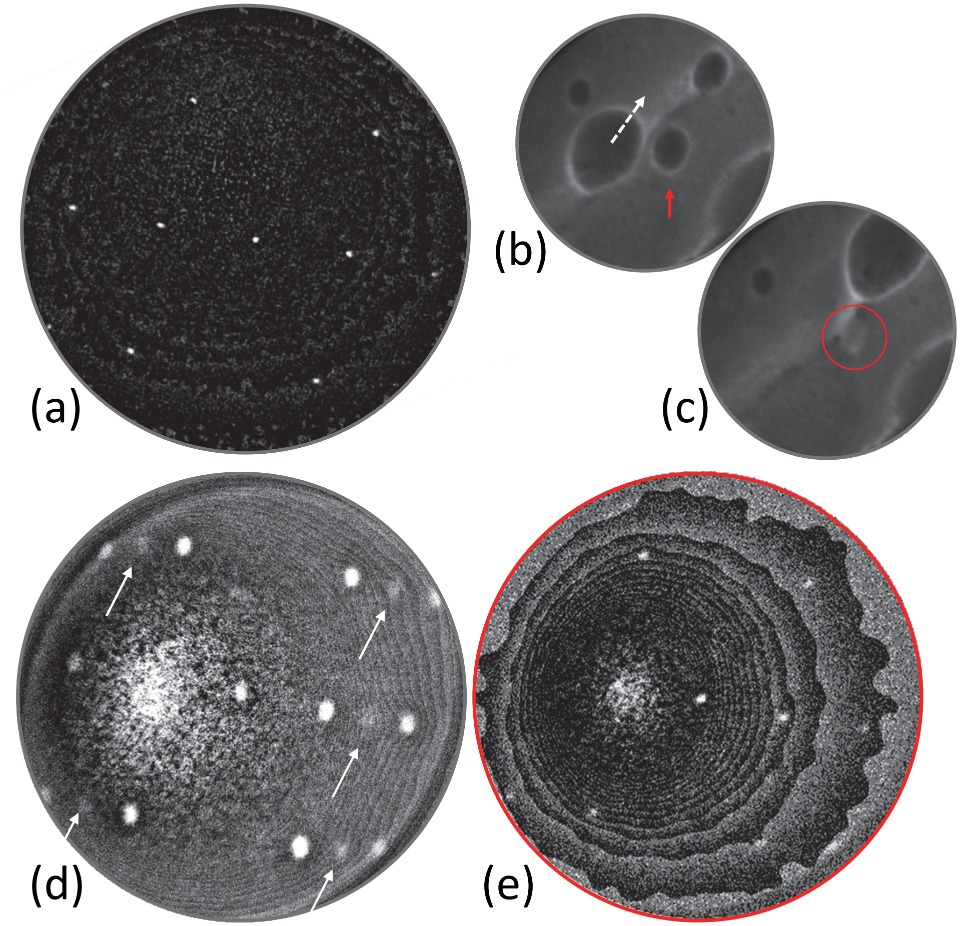

Figure 4.8: (a) Diffraction pattern of the clean surface measured at 1100 K and taken at 30 eV. (b) and (c) Mirror image data (SV = -1.3 eV) from the footprint area, respectively before and after coalescence of the droplets in the centre resulting in the encircled footprint in (c) of the droplet pointed out in (b) by the red arrow. The white dashed arrow indicates the direction of motion of the larger droplet, which has advanced to the edge in (c). FoV 15 m. N.B. The images were taken in mirror mode. Note the reversal of contrast when compared to PEEM. (d) and (e) diffraction patterns taken at 30 eV outside and inside the footprint, respectively. The arrows indicate a new half order peaks revealin a (2×1) reconstruction in (d)

.

(0,1) and (0-1) characteristic of the (1x1) pattern of a (110) surface of a diamond crystal such as Ge(110). See also Fig. 4.9. Instead we observe for an area, selected outside the footprint of the droplet in Fig. 4.7 the diffraction pattern exhibited in Fig. 4.8(d). It represents a (2×1) structure as sketched in Fig. 4.9(c) with its corresponding diffraction pattern in Fig. 4.9(d). Here every second atomic string of one of the two Ge-sublattices is replaced by a string of Pt atoms (sketched in blue). The replacement of each Ge atom in that string leads to extinction of the (0,1) peak. The constructed (2×1) pattern matches exactly the one observed in Fig. 4.8(d) and we thus conclude that the uniform wake of the moving eutectic droplets consists of (2×1) cells with a composition of 1 Pt atom per 3 Ge atoms. This ratio (0.25) is close to that (0.22) at the eutectic point. We note that no preference for the Pt exists for the replacement of [-110] Ge chains belonging to either the bluish or the reddish sublattice. Therefore, different equivalent domains coexist. The size of domains must be small compared to the transfer width of the used instrument (several tens of nm) as we conclude from the extinct (0,±1) peaks in the (2×1) diffraction pattern. The distance between two neighboring [-110] Pt chains is 1.12 nm, i.e. exactly equal to the minimum distance between Pt induced nanowires [22].

We now return to Fig. 4.7. Smaller droplets follow the thermal gradient in the wake of the large one. They are about equally fast and all eventually catch up with the large one resulting in successive mergence of the small one(s) with the large one. The large droplet has a straight contact line with the surface because it touches and wets a step bunch (bottom-right side). A main part of the subsequently arriving droplets follows its wake and they tend to make contact to the step bunch too. The two panels illustrate a mergence event of a smaller droplet with the largest one. It is highly remarkable and meaningful that the smaller of the merging droplets leaves behind a “footprint”, indicated by the red arrow. This footprint is an area with a higher work function since it is imaged at a lower brightness in PEEM. The blue arrow shows a similar footprint after a previous mergence event. All footprints are remarkably stable with time even at the current high temperatures. Using LEED we have also measured diffraction patterns inside these areas. An example is shown in Fig. 4.8(e). Here the diffraction pattern is measured inside the footprint of the smaller droplet after coalescence in Fig. 4.8(c). We note in passing that the brightness in mirror images of the footprints is higher than their environment in contrast to PEEM images. This is in both cases a consistent signature of the higher work function in the footprints. To our surprise we find a (1×1) diffraction pattern (Fig. 4.8(e)), which is indicative of a non-reconstructed Ge(110) patch. Evidently, the footprint is swept clean from previously present Pt during coalescence and a direct consequence is that the droplets make direct contact with the underlying substrate. This enables a direct exchange of Ge between the substrate and the eutectic droplet on its way to areas at higher temperatures in order to obey the temperature imposed composition, i.e. the Ge-Pt ratio on the liquidus line. The mass exchange takes readily place via atomic steps,

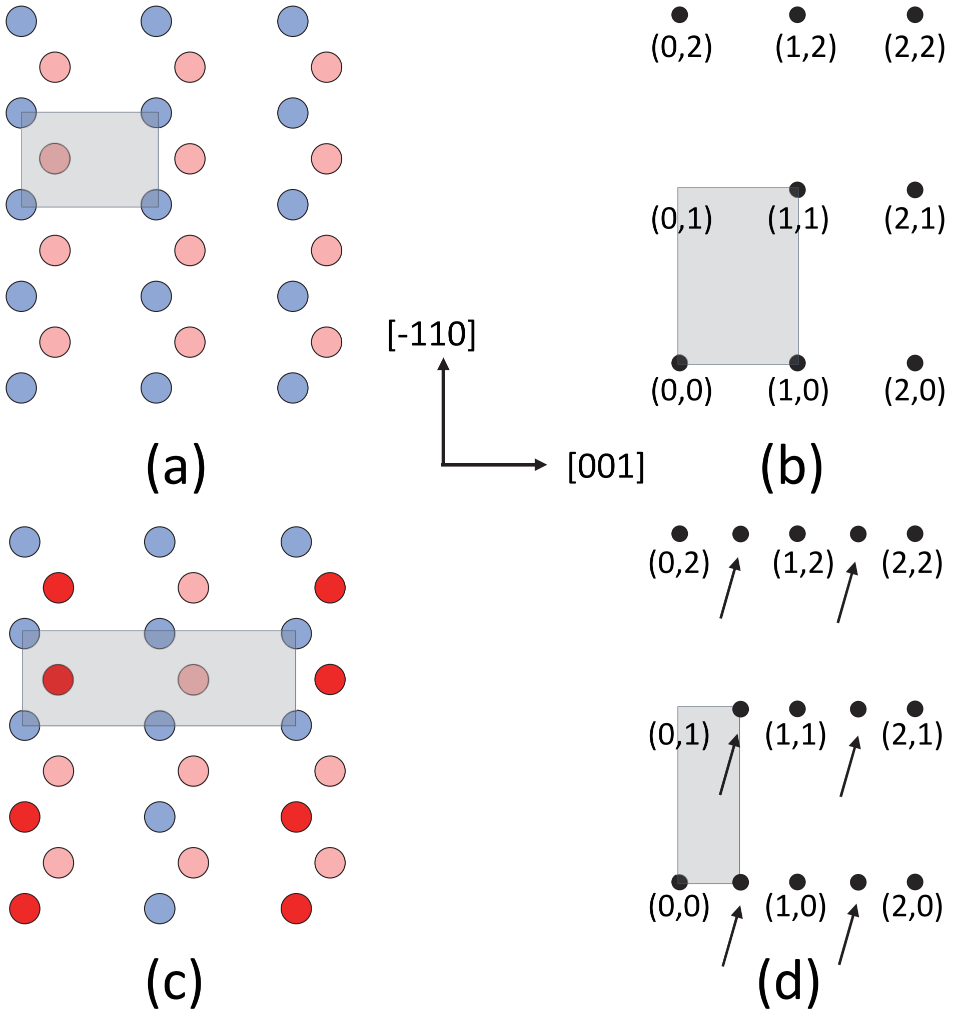

Figure 4.9: The crystal directions are indicated and the two identical sublattices are distinguished by a different color. (a) The atomic arrangement of atoms in the uppemost layer of a bulk terminated (110) face, also showing a (1x1) unit cell and (b) the corresponding LEED pattern. Note the extinct (0,1) peak as a direct consequence of the diamond structure of Ge (c) each second of the [-110] surface strings of the reddish sublattice is replaced by Pt atoms (red). A possible (2×1) unit cell is shown too. An equivalent domain with exchange of [-110] strings of the bluish sublattice is possible and involves a glide line. (d) Corresponding (2×1) LEED pattern. For the sketched configuration the (0,1) peak is also extinct if the domains separated by glide lines are small. The glide vector runs along [-111] with a length of $\sqrt{6}$ Å.

multiple steps or step bunches. At the same time this explains how substrate steps are affected by the passage of a eutectic droplet as observed in many publications [5,6,8,18]. We emphasize that even for a misalignment of 0.1° the step density is of the order of 20 per running micron and steps are thus readily available for micron sized droplets in order to establish equilibrium between the droplet and the substrate.

The overall picture that emerges so far is summarized by the sketch in Fig. 4.10.A close inspection of the wake of the eutectic droplets appears to indicate that upon each passage of a eutectic droplet the trail gets slightly less bright. This is attributed to a minimal loss of Pt from the strings to the passing spherical segment of the eutectic droplet. This would result more and more in a situation that slowly approaches the pure Ge case and goes along with an increase of the work function. This would be accompanied by a slight increase of the average distance between the Pt strings (see Fig. 4.9).

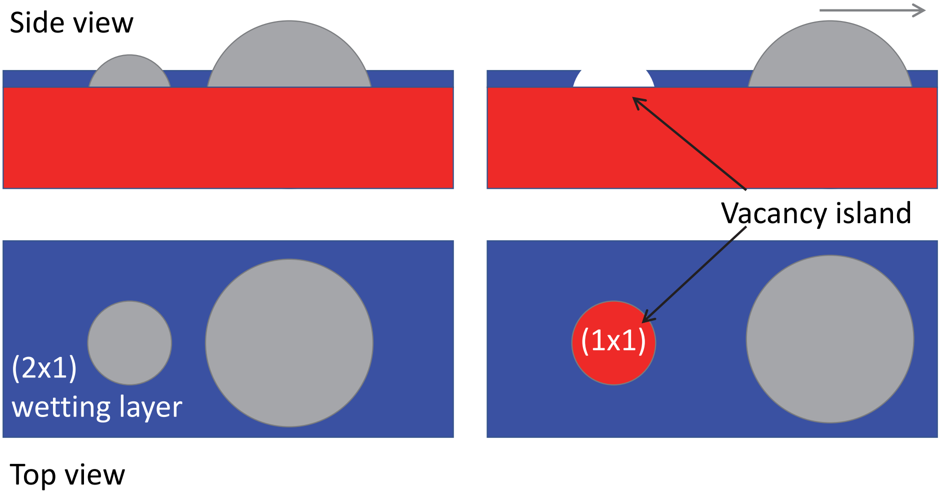

Figure 4.10: Sketch of two eutectic PtGe droplets in light blue before and after coalescence on the left hand and the right hand sides, respectively, in side view and in top view. The Ge (110) substrate in red, the (2x1) wetting layer in dark blue and (1x1) Ge(110) visible in the vacancy island left behind by the smaller of the two initial droplets. The wetting layer is 1 atomic layer thick and thus much thinner than it appears here.

Subsequently, the motion of droplets along the wake of the large one in Fig. 4.7 is evaluated in more detail. Characteristic and highly instructive data is exhibited in Fig. 4.11. A sequence of smaller droplets follows the route alongside the step bunch. A vacancy island is marked with “n”, a consecutive droplet by “$n+1$” (Fig. 4.11(a)).

In fact, “n” rather marks the stable footprint of droplet “n” which emerged during

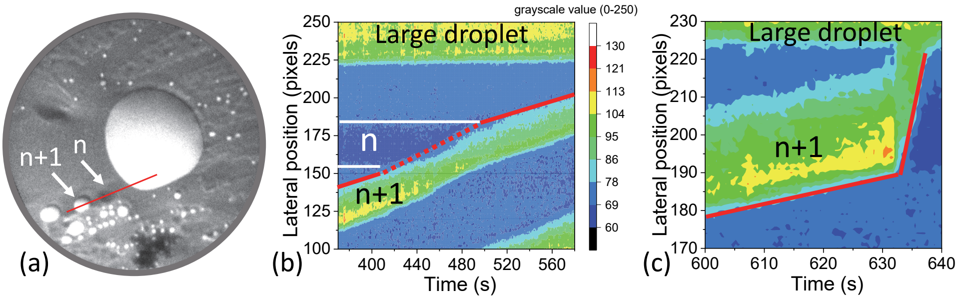

Figure 4.11: (a) Frame of the PEEM movie already addressed in Fig. 4.7 (see that caption for details). The frame has been captured about 17 minutes later than the last captured frame in Fig. 4.7. n marks the footprint of droplet n's mergence with the large one on the right and $n+1$ marks a consecutive droplet. (b) The brightness of the image measured along the red line in (a) with proceeding time. The passage of droplet $n+1$ through the vacancy cluster n is highlighted. The slope of the red lines defines the velocity of the droplet before and after (solid lines) and during (dashed line) passing vacancy n. (c) The brightness of the image measured along the red line in (a) just before mergence of droplet $n+1$ with the large one on the right. The evolution of the receding edge of "$n+1$" is indicated by the read lines.

its coalescence with the large one. The red line in Fig 4.11(a) indicates the trajectory followed by the small droplets. In the central part the droplets touch the step bunch at the substrate and move forward parallel to it. Figure 4.11(b) shows the brightness (see color scale on the right) measured along the trajectory. The corresponding position is plotted along the Y-axis. The time advances along the X-axis. The vacancy island is visible and immobile till ca $t = 480$ s. The receding edge of the large droplet is visible in the upper part of the figure and its small positive slope reveals a low speed of the order of a few nm/s. Also the motion of droplets $n+1$ and the next one is visible and from their slope one extracts a speed of the order 100 nm/s. Upon passage of the droplet $n+1$ the position and shape of the vacancy island n is affected.

Most importantly one can follow the speed of the receding edge of droplet $n+1$ during its mergence with the big droplet. This speed, which is controlled by the diffusivity of the liquid material in the small droplet during its pick up by the large droplet, is determined from the slope of the low- to high brightness transition during the final few seconds of the data. Due to its prime importance to this paper we illustrate these in Fig. 4.11(c). It shows on the left the last few frames of the movie already discussed above just before mergence of the small droplet "$n+1$" with the large one of the right. The corresponding part of the brightness diagram is shown in the right hand panel. The position of the receding edge of droplet “$n+1$” is enhanced by the red lines. Just near the right edge a vacancy island emerges as the result of the mergence. During merging, the contact lines disappear between the droplets and the breaking of bonds is no longer rate limiting. The advance rate of the receding edge during mergence is not less than about 50 times faster than during the motion of the small droplet. From this strong mismatch it is immediately clear that the diffusivity inside the droplet is *not* the rate limiting factor for the speed of the thermally driven motion of the eutectic droplets. This is at variance with the model for bulk diffusion of eutectic droplets put forward by Cline and Antony [1] given by Eq. 4.8, which has been embraced in so many surface diffusion studies. This fact, in combination with the total absence of a dependence of the speed for droplets with equal size on the magnitude of the thermal gradient, as noted further above, leads to a complete failure of Eq. 4.8 to describe the droplets' speed. An explanation for the velocity of the droplets must include these facts as well as the lack of influence of the droplet size. A viable scenario would then be the dissolution of the edges of the wetting layer at the advancing side (see the sketch in Fig. 4.10). At the receding edge the material will be incorporated in the reestablished edge. Note that the Pt/Ge ratio in the wetting layer (1/4) and that inside the eutectic droplet are highly similar. One element in the motion of the droplet would then be dissolution of chains of atoms in the leading edge and simultaneous expulsion at the trailing edge. This process is size independent since the dissolution rate at the edge does hardly depend on the radius for large droplets. It also explains the lack of dependence on the local thermal gradient since only the absolute temperature counts and thermal differences are very small anyway. If we start from a typical diffusion speed, v, for the droplets of 100 nm/s and rate limitation by the breaking up breaking up of atomic bonds in the edge (contact line) of the wetting layer at the advancing side of the droplet we can derive the

$$v = f a \exp\left(\frac{E}{k_B T}\right),\ E = k_B T\ \ln\left(\frac{v}{f a}\right) \tag{4.9}$$

corresponding activation barrier. The lattice distance is denoted by a. By assuming an attempt frequency, f, of 10 $^{13} s^{-1}$ we arrive at $E \sim 2.2$ eV.

A still unanswered question is why the small droplets (diameter less than ca. 3 μm) stay immobile across the entire surface. This appears connected to the unusual ripening behavior. It is well known due to Gibbs-Thomson that the equilibrium pressure to maintain droplets or crystallites increases with decreasing radius [23]. As a result, near equilibrium larger droplets grow at the expense of smaller ones and this process is known as Ostwald ripening. Less broadly realized is the fact that the same Gibbs-Thomson principle leads to the opposite result for vacancy clusters in the bulk or, for the same reason, vacancy clusters in 2D. The equilibrium pressure P_r to maintain liquid clusters in crystalline surroundings *decreases* with *decreasing* radius r according to

$$\frac{P_r}{P_\infty} = \exp\left(-\frac{2 \cdot \sigma \cdot v_l}{r \cdot k_b \cdot T}\right). \tag{4.10}$$

i.e. smaller vacancy clusters are more stable than their larger counterparts. The interface tension is σ and v_l is the atomic volume in the liquid, while P_∞ denotes the equilibrium pressure for a flat infinitely large separation plane. A similar expression holds for a liquid surrounded by a crystal in two dimensions as is the case here. In other words it becomes increasingly difficult to dissolve edge atoms of smaller vacancy clusters in the wetting layer into the droplet. We attribute the observation of a threshold size for small droplets to become mobile in a thermal gradient to this feature.

Ripening on the surface takes predominantly place through the coalescence of moving droplets (Smoluchowski ripening) as documented above and this conclusion was reached in previous reports too [4-7]. This statement holds in particular in regions near the temperature maximum since, by its nature, there the density of radially moving droplets is highest and, consequently, the collision frequency is highest too. At larger distances from the centre the rate of Smoluchowski type ripening events is lower. At these positions also Ostwald type ripening is active as illustrated in Fig. 4.12. It shows a frame from the earlier referred to movie [17] and the red, arrows mark small droplets which disappear during a time lapse of 47 minutes. (We cannot exclude that the involved entities are crystalline Pt containing features.) The mass transport takes place on top of the wetting layer and Pt_xGe_y particles are detached from the droplet at the contact line with the wetting layer. Consequently, Ostwald type ripening does occur but Smoluchowski type becomes increasingly more dominant at smaller distances from the centre.

Finally, we focus on the question whether the interface or the contact plane between the droplet and the substrate is flat or has a pit-like structure. The latter has been suggested for similar systems [4,8,10]. A complicating factor is that the optical impression of the footprints (see Fig. 4.8c.) seems to confirm that. However, it must be realized that the PEEM images only contain information on the local “structure” of the work function and thus reveals no direct information on the contour lines at the surface. *Ex-situ* information from AFM (Atomic Force Microscopy) or TEM (Transmission Electron Microscopy) is useless in this case since any temperature variation necessarily leads to huge mass exchange between the eutectic droplet and the surface. N.B., in the case of cooling from say 1100 K to the eutectic temperature of 1050 K per Pt atom 1.2 Ge atoms are re-deposited at

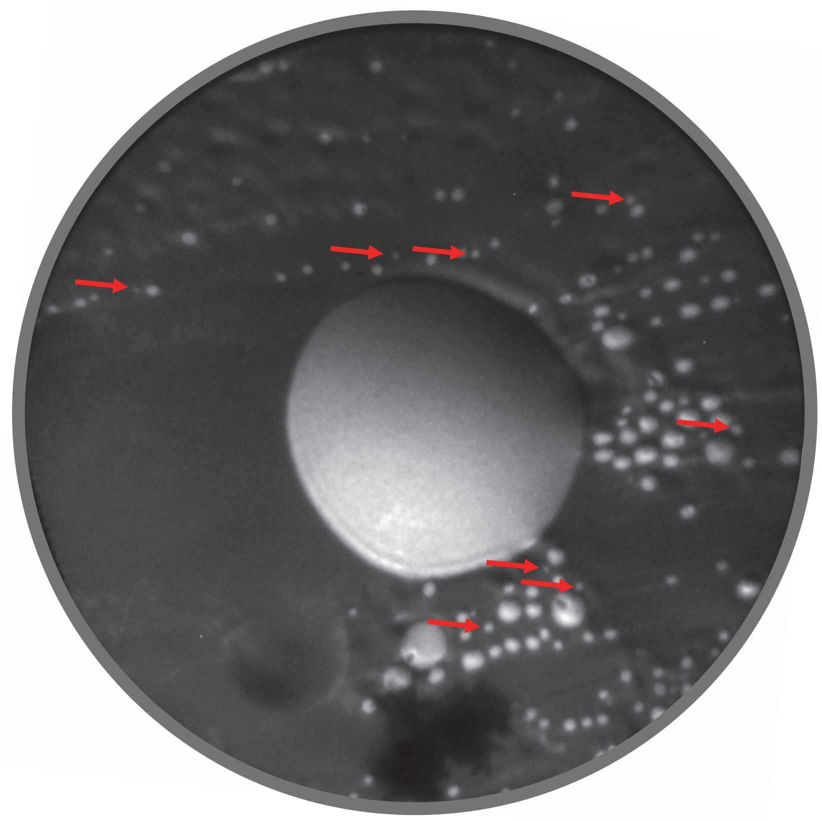

Figure 4.12: Frame from the PEEM movie referred to above (see Figs. 4.7 and 4.11). Field of view 150 μm, T = 1150 K. The central droplet moves to the right, while snapping smaller ones on its way to the centre (not shown here). Within 47 minutes space of time the small droplets, pointed at by red arrows, disappear due to Ostwald ripening (see text).

the surface. For a droplet with an exposed area of 10 μm^2 this implies > 1000 Ge atoms per Ge (110) unit cell of the initial interface. Thus, extreme caution must be exercised when trying to gain information on the flatness of the eutectic droplet-substrate interface from ex-situ data. Therefore, one is thrown back to indirect methods to shed light on this issue. In an attempt we presume that endotaxy applies and instead of a monolayer thick vacancy cluster inthe wetting layer the footprint marked with "n" in Fig. 4.11(a) one then deals with huge, thousands of layers deep pit. The passage of droplet "$n+1$" would accordingly take breaking up of the order of 10^{12} substrate atoms which one has to expect that the motion of the droplet must be *decelerated* substantially. Instead, it is found that the passage of the footprint "n" by droplet is leads to a temporary *acceler-*

ation of the velocity of the droplet by about 30% (see Fig. 4.11(b)). We conclude that this finding is hard to reconcile with any sizeable pit (endotaxy) underneath the eutectic droplet. In contrast, the acceleration is understood straightforwardly with the vacancy cluster model: passage the vacancy cluster involves the breaking of *lesser* bonds at the edge of the vacancy cluster and thus locally *speeds up* the motion.

4.4. DISCUSSION AND CONCLUSION

A wide spread notion for thermo-migration of micron sized eutectic droplets is based on the assumption that the driving force is given by the relative rates of dissolution of substrate material at the advancing side and re-deposition at the receding side. A concentration gradient of host substrate material (in the current case Ge) is maintained by its low diffusivity inside the eutectic droplet, which is finally limiting the speed of the moving droplets. This model provides a convenient way to explain the widely observed size independence of this speed "since driving force and mobility scale inversely" [5]. We think that this idea has contributed largely to the success of this model. Our current study for migration of GePt eutectic droplets on Ge(110) demonstrates that the explanation is in contrast with some key observations. First and of prime importance: the diffusivity inside the droplet is about 50 times faster than needed to make diffusion of Ge inside the droplets rate limiting for their speed. Second and equally significant is the fact that the speed of migrating droplets with equal size is unaffected by a thermal gradient that varies by as much as a factor of 6 (see Fig. 4.13). Obviously, in this situation inverse scaling of mobility and driving force does not apply. In order to access this information we monitored the speed of a moving droplet from about 1.2 mm from the temperature maximum toward about 0.2 mm from the hottest spot. The results are exhibited in Fig. 4.13 given by the black squares. The variation of the absolute temperature at the visited positions is about 3.5 K and the rate of thermally activated processes is thus virtually constant. The red curve (dashes) shows the variation for an actual activation energy of 2.2 eV. The current model predicts according to Eq. 4.2 a linear variation with the thermal gradient. An estimate is illustrated by the straight blue line through the origin in Fig. 13. Within the position window, in which data were gathered, one should expect an increase of the velocity by a factor of not less than 6. In reality the velocity remains constant or even leans toward a minor decrease. The result reveals an obvious failure of the currently popular model. To explain our observation we instead propose that the droplets make direct contact to the substrate and are surrounded by a flat wetting layer. The rate limiting step for the migration speed is then determined by

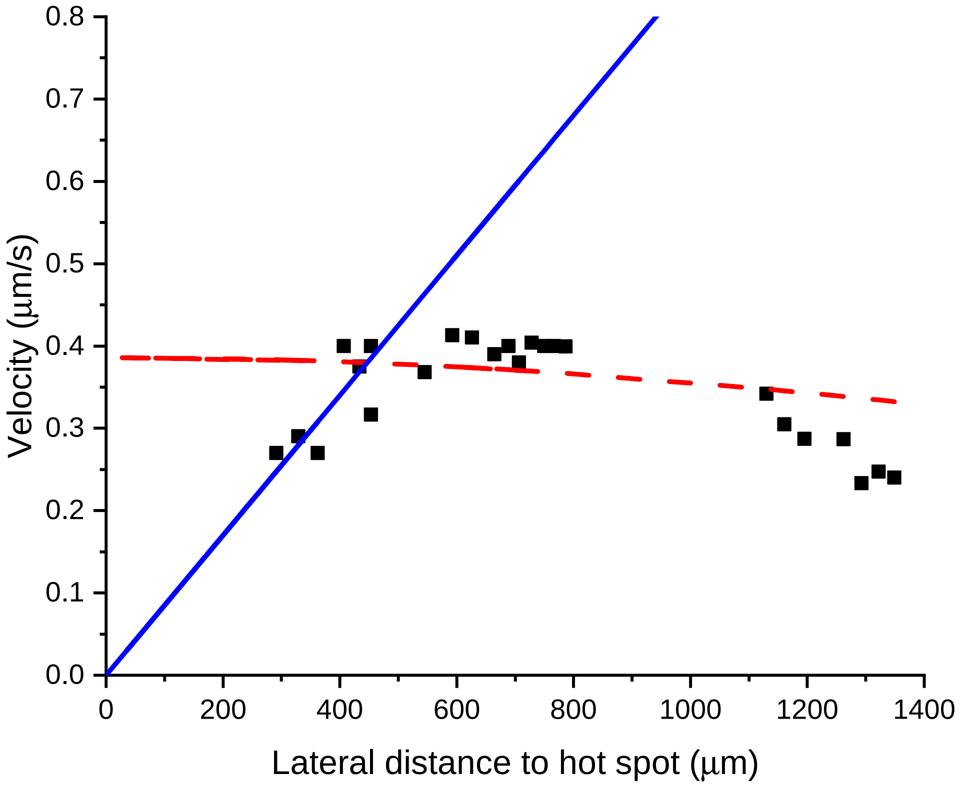

Figure 4.13: Velocity in μm/s of a moving droplet followed from 1200 till 200 μm toward the centre (black squares). Between ca. 750 and 1100 μm the droplet follows a pre-existing trail at an enhanced speed. The straight blue line from the origin through the cloud of the first seven data points indicates the expected behavior for a paraboloid-shaped temperature profile on the basis of Eq. 4.2. See text for further details. Note that the velocity values are somewhat higher than those in Fig. 4.4, which is attributed to a non reversible change in the thermocouple, which caused an offset of about 20 K.

the rate of dissolution in the contact line of the wetting layer with the moving droplet at the advancing side. The integrity of the wetting layer is restored at the receding side. The involved activation energy amounts to 2.2 eV, assuming a frequency factor of 10^{13} Hz. A very slight increase of Ge per Pt atom content within the droplet during travel is readily provided by exchange at pre-existing substrate steps. The interface between droplet and substrate remains basically flat. This model naturally provides the explanation for the size independence of the motion and also for its independence on the thermal gradient. The presence of a wetting layer is also held responsible for the relative smoothness in the wake of the moving droplets.

Our model also offers an alternative and quantitative description for the temperature dependence of the velocity of traveling eutectic droplets that appeared in the most detailed reports in literature so far. The result for AuGe droplets on Ge(110) [14] is exhibited in Fig. 4.14. The experimental results have been taken from Ref. 9 (Fig. 4.5) and also the calculated mobility curve by the dashed curve from the bulk based model. The blue dots are obtained with our model with an activation energy of 1.75 eV. The obtained frequency factor is ~10 ^{11} Hz. The latter description provides a clearly convincing result. Note that the three experimental points around 1010 K deviate severely from the overall trend for unknown reasons.

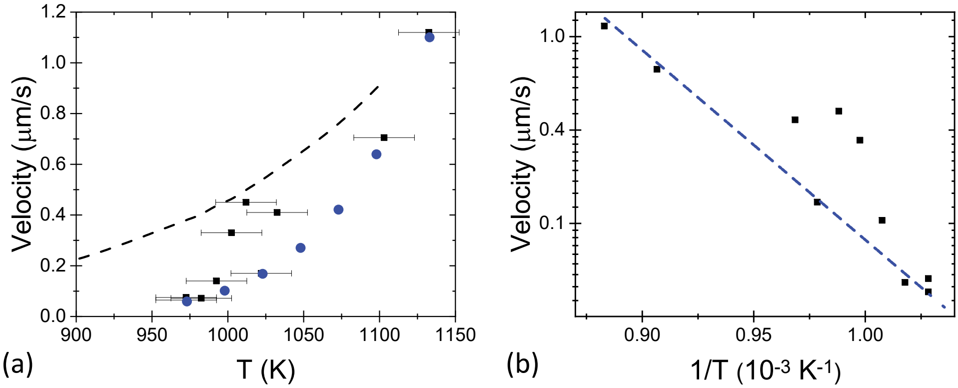

Figure 4.14: (a) Measured (black squares) and calculated (dashed curve) traveling velocities of AuGe eutectic droplets on Ge(110) as replotted from Fig. 4.5 in Ref. 9. The blue dots were obtained using our current model (see text). (b) Semilog plot of measured velocities and reciprocal temperature.

Another direct support of our current model is illustrated in Fig. 4.15 for the motion of PtSi eutectic droplets on Si(100). The beautiful experimental data have been taken from Ref. 4 (Fig. 4.7). Both the temperature dependence and the remarkable temperature dependent critical size for motion of droplets remained unexplained so far. It is even in obvious contrast with a velocity limiting diffusion rate of Si within the droplets. Our model offers a straight forward frame for understanding the temperature dependence of the velocity of the moving droplets. An Arrhenius plot of ln v versus T^{-1} yields a perfect straight line with a slope that corresponds to an activation energy of 2.0 eV and a frequency factor of ~ 3 × 10^{10} Hz. Note that the size independence is a natural aspect of our model. Even the enigma of a temperature dependent critical droplet size is easily resolved. The only assumption to make is that in line with Eq. 4.10 the relative pressure

P_r/P_∞, necessary to keep the contact line of the vacancy inside the wetting layer intact, is constant or, is constant. The only thing to realize is that σ varies in a generic way as a function of $\frac{T}{T_C}$ when the (twofold) symmetry of the surface is accounted for properly. We have taken the roughening temperature T_C equal to the melting temperature, but note that the exact choice is of marginal importance. With the most accurately known value at 1358 K as a fitting point the critical value for r_c at the other two temperatures is calculated readily. We consider the result as highly encouraging and conclude overall that the bulk based model for motion of eutectic droplets on a surface fails and propose instead to apply our current model. The structure of the wetting layer for PtSi on Si(100) is $c(4\times2)$ and that for AuSi on Ge(110) is (2×1). A careful reconsideration and re-evaluation of the validity of the Cline and Anthony model for diffusion of eutectic droplets on surfaces is urgently required.

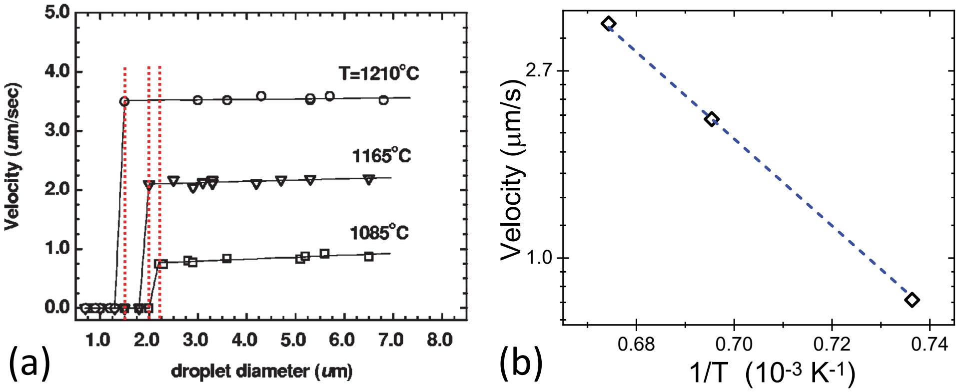

Figure 4.15: (a) Velocity of moving eutectic PtSi droplets on Si(100) as a function of their diameter at three different temperatures. The red vertical lines represent the critical values for motion of the droplets (see text). The experimental data were taken from Fig. 4.7 of ref. [4]. (b) Semi-log plot of velocities versus reciprocal temperature.

Finally, we emphasize that our current results refer to the mobility of large (micron sized) droplets on surfaces. The nice studies by Müller and colleagues [e.g., 8,19] address the mobility of (much) smaller droplets. The latter occurs in a different ball park with a much larger influence of steps as mentioned already by Sutter and co-workers [5,6]. The notion that droplets move step upward would and cannot apply for the large droplets considered here. In this case and in extremity an upward self propelling would demand the build up the base shape of a not yet erupted “vulcano” at the centre of the surface, i.e. the hottest spot. This unphysical picture is at variance with our observations. It is noted as a disclaimer too that Müller et al’s experiments were performed mainly during deposition of metals on the semiconductor substrate.

BIBLIOGRAPHY

[1] H. E. Cline and T. R. Anthony, J. Appl. Phys. **47**, 2325 (1976).

[2] W.-X. Tang, C.X. Zheng, Z.-Y. Zhou, D. E. Jesson, and J. Tersoff, IBM J. Res. Dev. **55** (4) Paper 10 (2011).

[3] J. Tersoff, D. E. Jesson, W. X. Tang, Phys.Rev. Lett. **105**, 035702 (2010).

[4] W.C. Yang, H. Ade, and R. J. Nemanich, Phys. Rev. B **69**, 045421 (2004).

[5] P. A. Bennett, J. Chobanian, J. I. Flege, E. Sutter, and P. Sutter, Phys. Rev. B **76**, 125410 (2007).

[6] P. Sutter, P. A. Bennett, J. I. Flege, and E. Sutter, Phys. Rev Lett. **99**, 125504 (2007).

[7] A. El-Barraj, S. Curiotto, F. Cheynis, P. Müller, and F. Leroy, Appl. Surf. Sci. **509**, 144667 (2020).

[8] S. Curiotto , F. Leroy, F. Cheynis, and P. Müller, Sci. Rep.**7**, 902 (2017).

[9] B.H. Stenger, A.L. Dorsett , J.H. Miller, E.M. Russell, C.A. Gabris, and S. Chiang, Ultramicroscopy **183**, 72 (2017).

[10] F. Leroy , A. El Barraj, F. Cheynis, P. Müller, and S. Curiotto, Phys. Rev. Lett. **123**, 176101 (2019).

[11] S. Kodambaka, J. Tersoff, M. C. Reuter, and F. M. Ross, Science **316**, 729 (2007).

[12] O. Gürlü, O. A. O. Adam, H. J. W. Zandvliet, and B. Poelsema, Appl. Phys Lett. **83**, 4610 (2003).

[13] H. J. W. Zandvliet, A. van Houselt, and B. Poelsema, J. Phys.: Cond. Matt. **21**, 474207 (2009).

[14] C.H. Mullet and S. Chiang, Surf. Sci. **621**, 184 (2014).

[15] J.S. Wang, S. Jin, W.J. Zhu, H.Q. Dong, X.M. Tao, H.S. Liu, and Z.P. Jin, Calphad **33**, 561 (2009).

[16] D. A. Porter, K.E. Easterling, M.Y. Sherif, Phase transformations in metals and alloys, CRC Press, Boca Raton, 2009, chapter 1 and 4.

[17] B. Poelsema, Z. Zhang, J.S. Solomon, H.J.W. Zandvliet, and A. van Houselt, Phys. Rev. Materials **5**, 125602 (2021).

[18] Z. Zhang, B. Poelsema, H.J.W. Zandvliet, and A. van Houselt, Phys. Rev. Materials **5**, 105601 (2021)

[19] S. Curiotto, F. Leroy, F. Cheynis, and P. Müller, Surface Science **632**, 1 (2015).

[20] C. H. Liu, W. W. Wu, and L. J. Chen, Appl. Phys. Lett. **88**, 133112 (2006).

[21] B. Poelsema, Z. Zhang, J.S. Solomon, H.J.W. Zandvliet, and A. van Houselt, Phys. Rev. Materials **5**, 125602 (2021).

[22] L. Zhang , P. Bampoulis , A. Safaei, H.J.W. Zandvliet, and A. van Houselt, Appl. Surf. Sci. **387** (2016) 766.

[23] I.V.V. Markov, Crystal Growth for Beginners, World Scientific, 2003.

5

A MICROSCOPIC STUDY OF THE SPINODAL DECOMPOSITION OF SUPPORTED EUTECTIC DROPLETS DURING COOLING: PTGE/GE(110)

This chapter is submitted as Z. Zhang, B. Poelsema, H.J.W. Zandvliet and A. van Houselt, *A microscopic study of the spinodal decomposition of supported eutectic droplets during cooling: PtGe/Ge(110)*.

ABSTRACT We embarked on an *in-situ* LEEM, PEEM, and μLEED study during cooling of large eutectic droplets through critical stages of the eutectic transition. On this journey through uncharted waters we revealed an expected initial shrinking of the exposed area of the droplet followed by an unanticipated expansion. This behavior is attributed to an initial fast amorphization of the interface between droplet and surface, followed by recrystallization of the Ge expelled from the droplet at the interface. As a major surprise we discovered the emergence of extensive "spaghetti"-like patterns, which are rationalized in terms of parallel Ge ripples oriented mainly along [-554] and [-55-4] directions. They emerge during spinodal decomposition when passing the eutectic temperature of the system. Their sides are defined by {111}- and {11-1}- Ge-vicinals covered with Pt-modified ($\sqrt{3} \times \sqrt{3}$) superstructures. The distance between adjacent ripples is about 18 nm. The mirror side of the Ge evolution is the coincident emergence of a large orthorhombic Ge_2Pt crystal, which is aligned with Ge{110} at an almost perfect lattice match.

5.1. INTRODUCTION

THE emergence of eutectic droplets on solid surfaces and their temporal evolution above the critical temperature has received proper attention [1-6]. It has been well-documented that, under the influence of a finite temperature gradient, eutectic droplets are thermodynamically driven towards the hottest available location at the surface and grow mainly through Smoluchowski ripening, i.e. coalescence and mergence. This leads in the ideal case to one big droplet at the thermal summit and in practice to accumulation of few large droplets in the center. We have recently communicated a compelling example for PtGe on Ge(110) [7]. Where *in situ* information on the evolution of eutectic droplets at different temperatures above the eutectic temperature, $T_{eutectic}$, is readily accessible, the situation is different for evolution during cooling through $T_{eutectic}$. It is evident that during the thermally induced motion strong interaction with pre-existing atomic steps occurs. Obviously, direct information on the scene of the all-important action, i.e. the exchange of (former or future) substrate material at the interface between substrate and the droplet is not accessible. It is known already that *ex situ* measurements, in this case Transmission Electron Microcopy, TEM, show that crystalline AB-remainders of the eutectic droplets reside on pedestals of B precipitated from the droplet during cooling on substrate B [2]. However, live information on the evolution of eutectic droplets when the system is driven through the eutectic transition during cooling is still lacking [8,9]. It appears that our current knowledge of the system PtGe/Ge(110) offers a promising opportunity to gain *in situ* more insight into the processes that are active during spinodal decomposition of eutectic droplets. We start with a microscopic view of a relatively small area around the hottest spot at the surface and thus with a large droplet. During cooling down the position of the hottest spot hardly changes and as a result the thermal gradient induced motion of the present droplets is minimal. This is of utmost importance, since the experiment can be executed only once after depositing Pt on the virgin Ge(110) surface.

In this study we apply PEEM (Photo-Electron-Emission-Microscopy), LEED (Low-Energy-Electron-Microscopy) and μLEED (selected area Low-Energy-Electron-Diffraction). We find an unanticipated “breathing” of the wetting angle and of, as a consequence, the exposed area of the droplet, which is traced back to structural changes at the droplet-substrate interface during cooling. In addition, we observe the emergence of “spaghetti”-like structures upon passing the critical temperature, which are rationalized in terms of a rippled spreading layer of pure Ge around the original droplet. In this process a crucial role is taken by a Pt containing (3×3) wetting layer on vicinal Ge(111) facets that constitute the ripples developing at the Ge(110) surface.

5.2. EXPERIMENTAL

THE experiments have been carried out with an Elmitec LEEM-III instrument with a base pressure of 10^{-10} mbar. In PEEM, the surface was illuminated with a 100 W mercury discharge lamp ($\lambda = 0.253\ \mu$m) incident at 16° from the surface plane. The absolute temperature reading is estimated to be correct within ca. 25 K and calibrated by making the reasonable assumption that the eutectic temperature at the surface equals that of the bulk (1050 K for GePt). A Ge(110) substrate, 10x10 mm^2, nominally flat, single-side-polished, n-type Ge (110) crystal (MTI Corporation, R > 50 Ω cm) has been degassed for about 24 hours at 700 K, followed by several cycles of Argon ion bombardment and flash annealing by e-beam bombardment at a temperature exceeding 1000 K. Subsequently, Pt is deposited from a resistively heated W wire wrapped with high purity (99.995 %) Pt (Alfa Aesar). The structure of the clean surface has been examined using LEED. Similar to the findings in ref. [6], we also observed a $c(8 \times 10)$ structure at lower substrate temperatures, while above 1050 K only the non-reconstructed (1×1) structure is observed.

5.3. RESULTS

AT the start of the current experiment the surface was prepared as described above, followed by a prolonged period (> eight hours) at a temperature of about 50 K above the eutectic temperature. As a result a large eutectic cluster is situated in the center at the hottest location at the surface and several smaller ones are still on their way to this center. We follow the lifeline of this particular object during a gentle cool-down. Initially, at the start of our PEEM-movie, the cluster moves a little due to a small change of the temperature profile: it still remains at the local hot spot, just microns away from its starting position. A few characteristic snapshots of the movie are reproduced in Fig. 5.1. We use spherical caps as a good approximation of the eutectic droplet with, initially, a flat interface with the Ge(110) substrate. Quite minor deviations from a circular geometry are attributed to step architecture such as step-bunches [10, 11]. The radius of curvature of the sphere cap of the major eutectic droplet (bright objects) amounts to $R_C = 90\ \mu$m and the wetting angle θ_w equals 20° [12]. The volume of the spherical cap is given by:

$$V = \pi R^3 \left(\frac{2}{3} - \cos\theta_w + \frac{\cos^3\theta_w}{3} \right) \tag{5.1}$$

For the major eutectic droplet above one obtains $V = 8.2\times10^3$ μm^3. With the atomic volume of 1 Ge atom per 22.6 $\times10^{-12}$ μm^3 (for bulk Ge) we find approximately 3.6 $\times10^{14}$ atoms inside the spherical droplet, assuming that the atomic volumes of Pt and Ge are identical in this crude estimate.

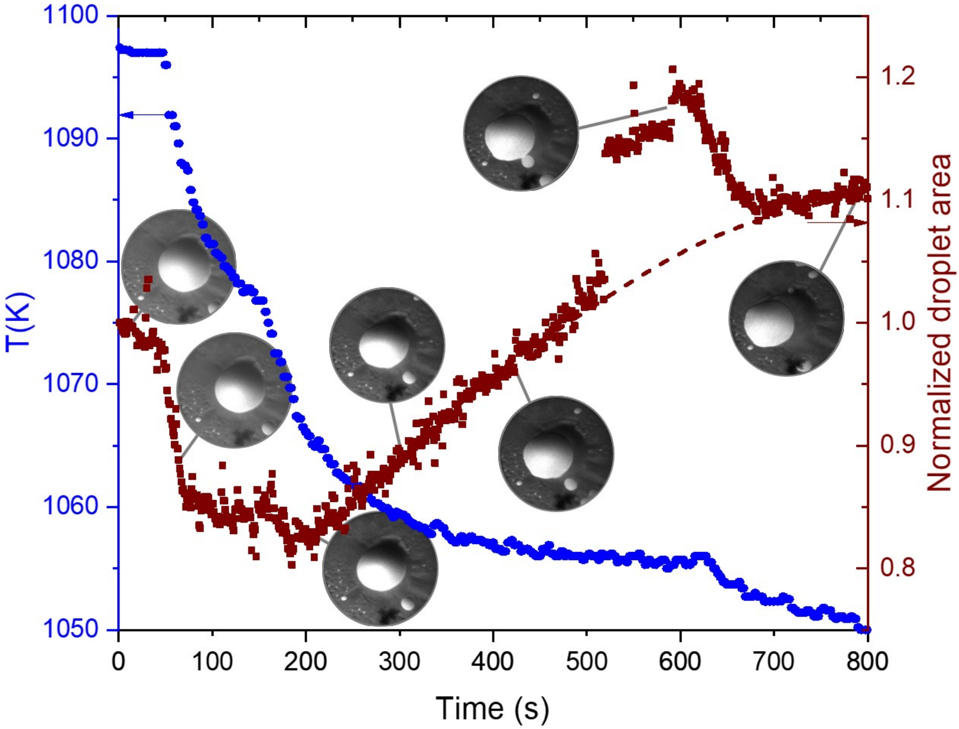

Figure 5.1: Several snapshots from a PEEM movie (Field of View 150 μm), taken during cooling towards the eutectic temperature of 1050 K taken at strategic temperatures. The temperature is given on the left hand scale. The projected area of the large eutectic droplet, normalized to its starting value, is given on the right hand scale. The relevant time scale is plotted along the abscissa.

As illustrated by Fig. 5.1, immediately upon cooling down the exposed area of the eutectic droplet decreases. It decreases by about 18% upon a temperature drop of 19 K. Qualitatively, this behavior is conform the expectation as derived from the Ge-Pt bulk phase diagram shown in Fig. 5.2. In equilibrium the system moves during cooling along the liquidus line marked in red towards the eutectic point at $T_{eutectic}$. As the number of Pt atoms inside the droplet remains constant and the relative content of Ge decreases, the segregating Ge atoms will be incorporated into/onto the Ge substrate at the droplet-substrate interface. For completeness we remark that also Ge_2Pt crystallites emerge below $T_{eutectic}$ [13, 14], which will be discussed in more detail at the end of this chapter. Immediately upon cooling one observes a decrease of the projected area of the droplet as illustrated in Fig. 5.1. This corresponds qualitatively to the expected decrease of the volume, provided that the wetting angle remains constant. However, we detect a substantial quantitative problem: we measure a decrease of the projected area of about 20 % during a temperature drop of 19 K, while from the slope of the liquidus line in the considered temperature range a volume drop of ca. 11 % is expected, resulting into a decrease of the projected area of only 7 %. In other words, the loss of Ge atoms inside the droplet can not fully account for the observed decay in the exposed area. This can be rationalized in terms of a change of the wetting angle. As is well known, the wetting angle is given by Young's equation [15]:

$$\gamma_{sv} = \gamma_{sl} + \gamma_{lv} \cos\theta_w \tag{5.2}$$

with γ_{sv} , γ_{sl} and γ_{lv} the interface tension of, respectively, the substrate-vapor, the substrate-liquid and the liquid-vapor interfaces, while θ_w denotes the wetting angle. Naively one would expect that within the small variations of the Ge content inside the droplet only marginal changes in the interfacial tensions occur and thus the wetting angle would stay constant. However, the sedimentation of Ge at the droplet-Ge(110) interface during cooling of the eutectic phase may well result in increasing kinetic roughness at this interface. This roughness would according to Wenzel [16] in the here applying case of wetting, lead to a reduction of the wetting angle:

$$\cos\theta_w^* = r \cos\theta_w \tag{5.3}$$

with θ_w^* the apparent wetting angle on the rough surface and r the roughness defined as the real surface divided by the nominal surface and thus by definition $r > 1$. Consequently, this would in our case, since θ_w is in the order of 20° (see chapter 3), result in an increase of the projected area. Therefore, kinetic roughening must be excluded as the course for the discrepancy we ran into. We do realize that an increase of γ_{lv} would lead to an increased wetting angle and potentially would lift the apparent discrepancy. To advance along this route we consider how much material is segregated from the spherical droplet segment to the droplet-substrate interface.

The base area of our spherical droplet segment with radius of curvature $R_C = 90$ μm droplet and wetting angle $\theta_w = 20°$ amounts to ~ 3000 μm^2. One atom in the Ge(110) surface covers 1.13×10^{-7} μm^2; in other words the circular base plane of the droplet counts roughly 2.6×10^{10} atoms. Deposition of all expelled Ge atoms at the base during the 19 K temperature decrease would therefore result in a growth of 1.4×10^4 Ge (110)-monolayers. The quick drop in exposed area during the 19 K temperature decrease occurs in about 25 s, conform the quick drop in exposed area is exhibited in Fig. 5.2. The Ge content of the droplet sinks from 0.85 to 0.831 and therefore 270 monolayers (ML) are deposited at the interface at an estimated rate of 11 ML/s. This is most likely too fast to secure crystalline growth, especially for semiconductors and amorphous Ge will grow at the interface [17]. At the amorphous interface the density of broken bonds is high and, therefore, the corresponding interface tension will be relatively high γ^{α}_{ls} [18]. Accordingly, we attribute the unanticipated shrinking of the exposed area of the cooling down eutectic droplet to kinetic amorphization of the growth front at the droplet-substrate interface.

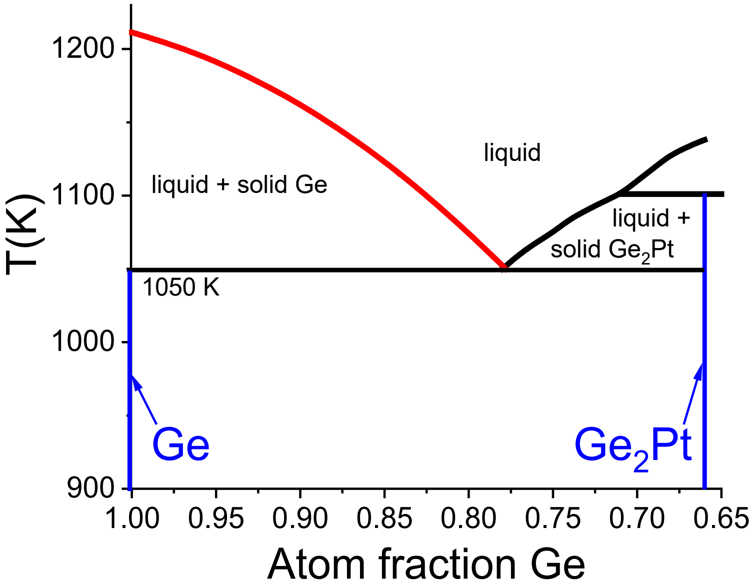

Figure 5.2: Bulk phase diagram of Ge-Pt reproduced from [19]

This scenario offers a natural framework for understanding the observed evolution of the projected area of the eutectic during later stages as illustrated in Fig. 5.1. A lower cooling rate gives rise to recrystallization of the amorphous crystalline interface. The liquid-substrate interface tension will thus decrease and the wetting angle decreases accordingly. Further slow decrease of the cooling rate then leads to lower wetting angles according to Wenzel (Eq. 3) and the final exposed area even overwhelms the initial one.

The behavior of the exposed area as a function of decreasing temperature clearly reveals that the two active processes, 1) kinetic amorphization and 2) crystallization at the droplet occur not consecutively, but rather simultaneously, i.e. competing processes are active with amorphization dominant during fast temperature decay and crystallization dominant at slow temperature decay rates. In this case the temperature adjustment was controlled in three steps and each time an initial drop is followed after some time by an increasing tendency of the exposed area when the temperature decay rate decreases. This behavior is nicely in line with the scenario outlined above.

When passing through the eutectic temperature two events occur simultaneously: 1) a spreading of material originating from the Ge-Pt droplet and 2) a partial crystallization of the former droplet remainders. In terms of the expected spinodal decomposition one would naively conclude that the spreading results mainly from Ge incorporation in the Ge(110) substrate and the crystallization at the position of the former droplet would result in Ge_2Pt crystallites. This expectation appears to be confirmed, however with an unanticipated twist as we will discuss in detail further below. In this evaluation scheme our exemplary spherically capped droplet with $R_C = 90\ \mu$m and $\theta_w = 20°$, when cooled down from 1100 K through the critical temperature contains 7.4×10^{13} Ge atoms which need to be reincorporated into the Ge(110) substrate. If these are equally spread over the area of the field of view of 150 μm in Fig. 5.1, it would imply a deposition of 470 ML and a corresponding height increase of slightly less than 0.1 μm. Anyway, one is bound to observe major mass transport near the center of the sample during spinodal decomposition.

A first impression of the events is provided by the snapshot in Fig. 5.3. The PEEM data shows that a film spreads from the congealing droplet and simultaneously the original droplet appears to solidify as well. First we concentrate on the spreading film, which soon covers the entire field of view in Fig. 5.3(b). After further cooling down the film one obtains evidence for remarkable structures that emerge during solidification of the spreading layer. An example is shown by the room temperature mirror image (-0.8 V) LEEM picture in Fig. 5.4, taken from the spreading layer at room temperature. A highly surprising and intriguing pattern has evolved, which we will refer to as “spaghetti” below. Across the field of view of 20 μm the spaghetti pattern appears quite homogeneous. It is

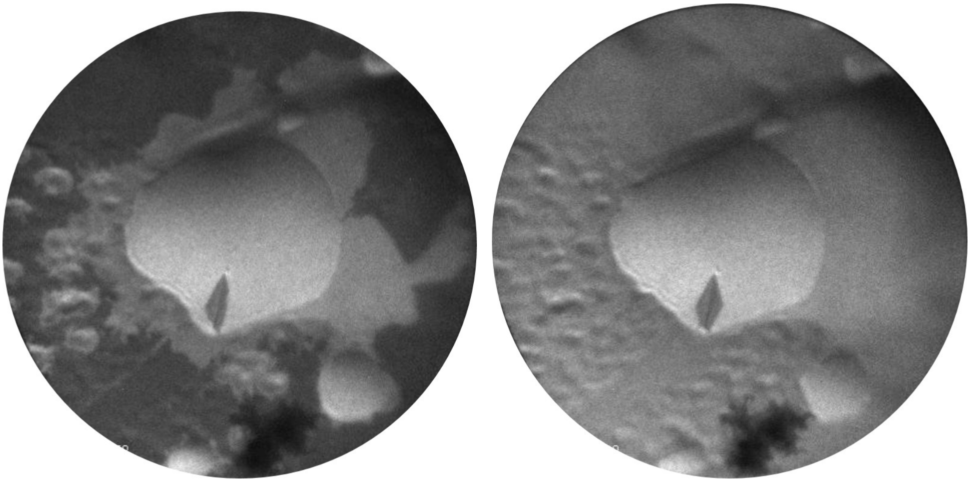

Figure 5.3: Two snapshots from a PEEM movie (Field of View 150 μm), taken during cooling. (a) PEEM image taken at 990 K; (b) PEEM image taken at 970 K.

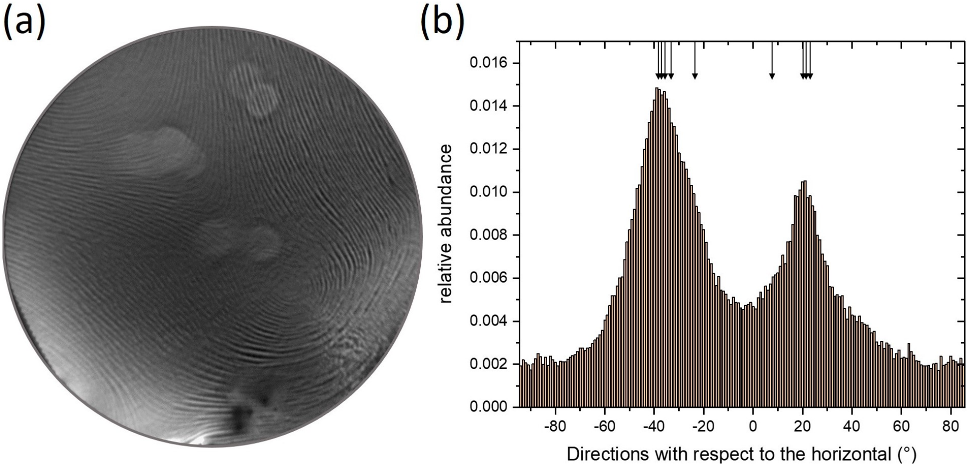

Figure 5.4: (a) Mirror image (start voltage - 0.8 V) taken at room temperature of the spreading-film (see text) with a Field of View (FoV) of 20 μm. At the somewhat brighter circular areas the electron beam dwelled for a longer term. (b) Histogram of the local directions of the “spaghettis” in (a) gathered in 1° wide bins. The numbers integrate to unity.

emphasized that the mirror image reveals work function variations mainly, which could be related to morphology (likely) and/or chemical composition (less likely). We find an obvious preference for the periodicity normal to the strings, which amounts to about 18 nm. The somewhat brighter circular areas result from a relatively long term interrogation of the structures by applying μLEED using the smallest available aperture of 1.4 μm. The contrast change is probably the result of a slight electron beam induced change of the local work function, but the figure clearly documents that there is no influence on the morphology. At first sight the directionality of the spaghettis is quite random, but a closer look reveals the strong preference for two azimuth directions as shown by the directional histogram in Fig. 5.4b). These preferred directions are about 60° apart. In order to gain a deeper insight into the complex rearrangement events at the surface during spinodal decomposition we apply μLEED on the spaghettis in a carefully selected area. The results have been obtained on one of the bright areas in Fig. 5.4a).

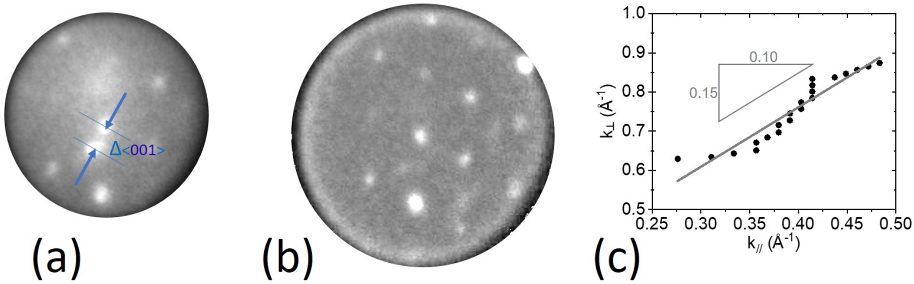

Figure 5.5: (a) and (b) μLEED patterns taken at 1.9 eV and 3.3 eV, respectively, aperture 1.4 μm, room temperature. The arrows indicate the (0,0) spots of the (110) substrate structure and that of the (distorted) hexagonal structure in the image. The distance between these spots along [001] is Δ_{001}. (c) the normal component of the wave vector (ordinate) versus Δ_{001} (abscissa) of the diffracted electrons.

To obtain more detailed insight into the structure and morphology of the "spaghettis" we apply μLEED, using an aperture of 1.4 μm. Figure 5.5 shows typical data from a representative area of the “spaghettis” (see Fig. 5.3a). Figure 5.5a) and 5.5b) exhibit measured diffraction patterns at electron energies of 1.9 and 3.3 eV. One distinguishes a distorted hexagonal pattern and an additional peak (indicated by the lower arrow), which is attributed to the specular peak of the (110) substrate (or areas parallel to this). Upon increasing the electron energy the distance between this peak and the specular spot of the distorted hexagonal pattern (higher arrow), referred to as Δ001, becomes larger. The value of the normal component of the wave vector of the diffracted electrons versus the parallel component change along [001] is plotted in Fig. 5.5(c). The relative motion of diffraction spots reveals the presence of facets at the surface [20-22]. From a plot of the vertical component of the wave vector change versus its parallel component for a number of electron energies one may derive the angle between different facets. Such a plot is made available in Fig 5.5(c) and we extract an angle of 35°. For a cubic crystal the angle between (111) and (110) planes amount to 35.26° and we can safely conclude that we are dealing with the emergence of (111) facets on the (110) substrate. This is further reinforced by the fact that (111) facets are quite stable and are often constituent of reconstructed (110) surfaces [23]. Also the presence of a (distorted) hexagonal structure in Fig. 5.5(a) and 5.5(b) hints into this direction. The intensity of the specular (110) spot decreases strongly with increasing electron energy. This feature is attributed to the fact that the transfer width of the instrument is a strong function of the electron energy and it gets only very large at zero energy [24]. The disappearance of the (110) specular spot already at low energies reveals that overall the (111)-facets dominate over (110)-areas.

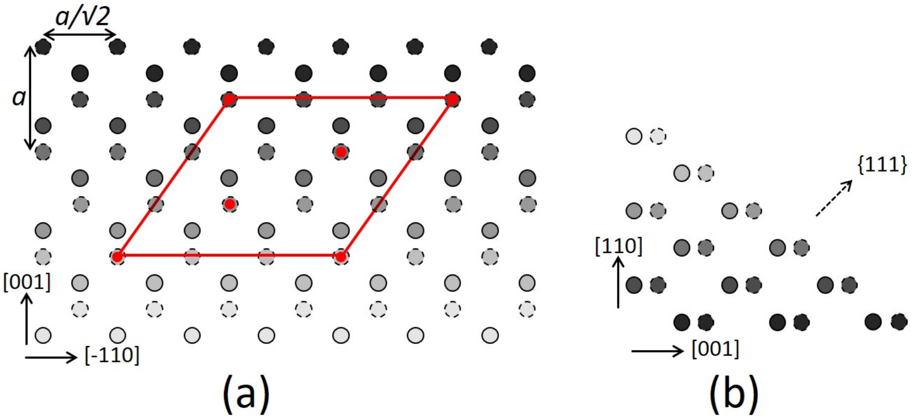

Figure 5.6: (a)Top view of the Ge(110) surface with a (111) facet. The edge runs along the [-110] direction (X-axis) and the Y-axis corresponds to the [001] direction. The atoms indicated by open and closed circles belong to different sublattices of the diamond structure. Increasingly darker atoms at consecutively lower (110)-levels. See text for the signification of the red dots. (b) Side view. The edges run along the [001] direction (X-axis) and the [110] direction (Y-axis).

Figure 5.6 shows a sketch of the Ge(110) surface with a (111)-facet. Figure 5.6(a) shows a top view of a projection on the (110) surface, while figure 5.6(b) shows a side view. The atoms indicated by open and closed circles belong to the two different sublattices of the diamond structure. We actually see the outermost [-110] strings of atoms at different (110) levels. The circles with stepwise increasing grey values denote Ge atoms at consecutively lower levels. Note that in this (110) projection the distance between the successive [-110] atom strings is smaller by a factor cos (35.26) = 0.82 than their distance within the (111) facet. This geometric fact causes the above mentioned distortion of the diffraction pattern of super-structures at the facets. A decrease in real space gives rise an elongation in reciprocal space. This is exactly what we observe as illustrated in the diffraction pattern taken at 4.1 eV and shown in Fig. 5.6. We have elongated an ideal hexagonal raster along the real space [11-2] direction by a factor $\cos^{-1}(35)$ (red grid) and find, neglecting minor residual image distortions, an almost perfect mapping of the measured diffraction peaks. This result is a strong confirmation for the already concluded presence of (111). The diffraction pattern reveals a (3×3) reconstructed hexagonal pattern. This is attributed to a Pt containing cover layer on the (111) facets. We suggest that 1/3 of the Ge atoms in the topmost layer of one of the sublattices is replaced by Pt. These are indicated by the red dots in Fig. 5.6. We emphasize that by definition the surface tensions for clean FCC (111), (100) and (110) surface increase in this sequence. In some cases the energy gain of (111) facets, when compared to the (110) termination may even outweigh the unfavorable correspondingly larger surface area, leading to a (2×1) reconstruction of the clean surface [25, 26]. The presence of a metal induced reconstruction of (111) may well influence the subtle energy balance in favor of the formation of (111)-facets. This may even lead to a preference of reconstructed (111) facets above (100) areas. A nice example of the latter is the Au-induced giant missing row reconstruction of Ge(100) with $(\sqrt{3}\times\sqrt{3})$ reconstructed (111) facets on Ge(100) [27, 28]. The current observations with Pt-induced (3×3) structures on large (111) facets reveals a similar mechanism. We suggest that the (3×3) structure originates from replacing 1/3 of the Ge atoms in the topmost layer of one of the sublattices by Pt as colored in red in Fig. 5.6(a). Note that the edge in Fig. 5.6(a) runs along the [-110] direction. Before we move on to a more detailed contemplation, we first want to note that the location of the incorporated Pt-atoms at the corners and the long diagonal gives rise to three Pt atoms in the $(\sqrt{3}\times\sqrt{3})$ and a simpler identification of the vital unit cell is rather a $(\sqrt{3}\times\sqrt{3})$ one with one Pt- and 2 Ge atoms in the unit cell. We prefer to work with this basic building block from now onwards.

It appears attractive to use the simple and straightforward model depicted in Fig. 5.6 as the explanation for the formation of Ge ripples, oriented along [-110] with Pt modified and stabilized {111} facets and mirrored $\{11-1\}$ facets on the opposite side. However, such a strong preference for the unilateral orientation of the ripples along [-110] is at variance with the observation displayed in Fig. 5.4, which clearly reveals a preference for two equivalent azimuthal directions which are about 60° apart. The reason for this at first sight unexpected result must be searched for in the strong anisotropy of the $(\sqrt{3} \times \sqrt{3})$-structure which is responsible for the evolution of the ripples in the first place. We suggest that the ripples are basically aligned along those directions which are most densely packed with Pt-atoms, i.e. along <11-2> rather than along <110> on the ripple's facets. This situation is sketched in Fig. 5.8 and explains the rationale for two strongly preferred azimuth directions for the emerged Ge ripples with $(\sqrt{3} \times \sqrt{3})$ reconstructed $\{111\}$ and $\{11-1\}$ oriented side facets. This biaxial local morphology is attributed to a strong stabi-

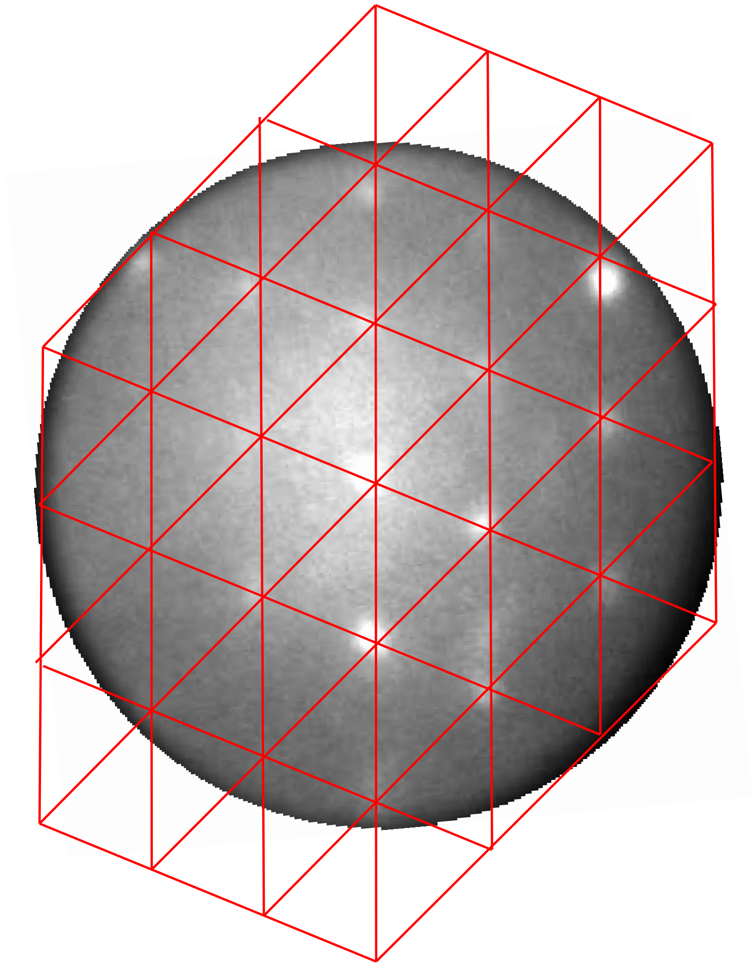

Figure 5.7: Measured diffraction pattern at 4.1 eV and room temperature. The red grid is elongated along the [11-2] direction by a factor 1/cos(35°).

lization of relatively favorable (111) terraces by the Pt induced ($\sqrt{3} \times \sqrt{3}$) reconstruction

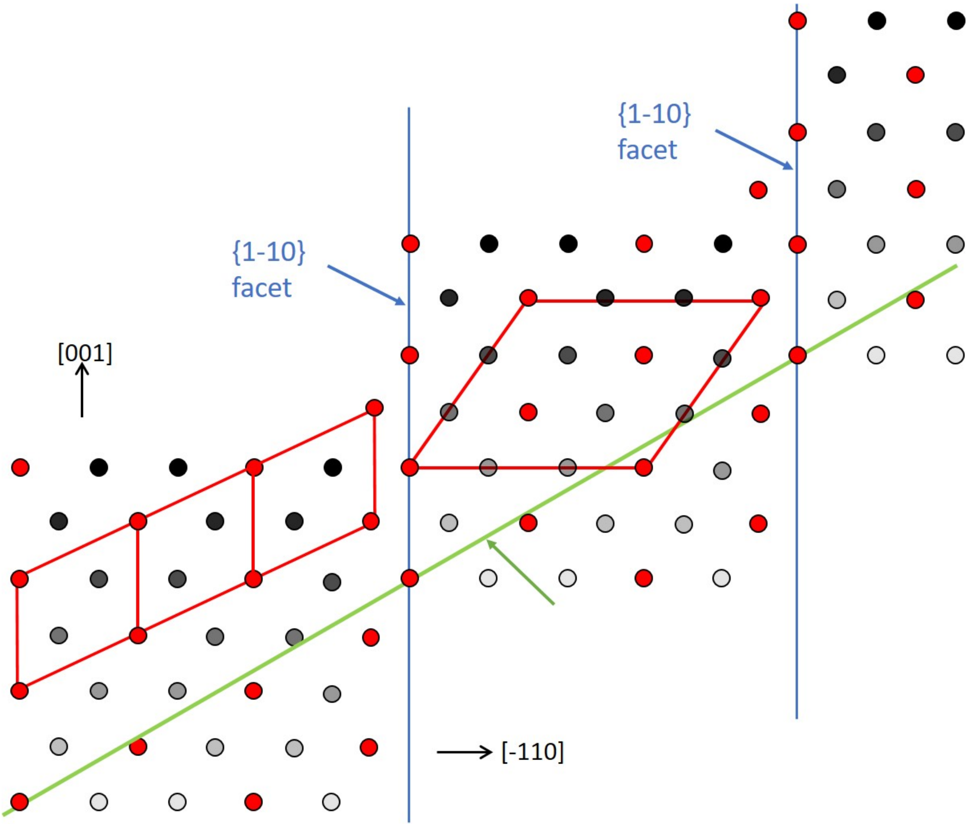

Figure 5.8: Top view of a Ge ripple oriented roughly along [-211] on the Ge(110) surface. A {111} facet is shown with increasingly darker atoms at consecutively lower lying lattice positions. For simplicity only one of the two sublattices is shown. Pt atoms that have exchanged positions with Ge are colored red. The blue lines indicate atomic (multi)steps on the 111 facet. The green line is the intersection of the {110} and {111} surface plane. The solid red grids show at the left hand side show ($\sqrt{3} \times \sqrt{3}$) unit cells on {111}. A full (3x3) cell in 110 projection is indicated by the larger red parallelogram on the central terrace. In reality atoms of both sublattices form a bilayer on (111) oriented facets. The uppermost atoms of the bilayer on 111 and 11-1 layers originate from different sublattices. The intersection of {735}, i.e. the stepped {111} face (see text), with {110} is indicated by the green line along [-554]. Note that for symmetry reasons w.r.t. [-110] an equivalent ripple occurs along [-55-4].

of the facets. The red circles identify Pt atoms which have replaced Ge atoms in the surface layer. We suggest that this feature even drives the distribution of atomic steps on the (111) facets in favor of a fit of the building blocks to individual terraces giving rise to so-called magic terraces [25]. For ease of survey Fig. 5.8 is organized differently when compared to Fig. 5.7: Still we show a (110) oriented projection, but instead of the two sublattices we only show one here. Deeper lying but still exposed lattice sites are shown with increasingly darker contrast. We only show the {111} oriented facet and the equivalent (mirrored) $\{11-1\}$ facet on the opposite side of the ripple is not shown. The blue lines indicate (multi)steps on the {111} facet. The red parallellograms on the left hand terrace indicate three $\sqrt{3}$ building blocks, while the larger red parallelogram on the central terrace illustrates an entire (3×3) unit cell. Note the distortion due to the projection onto {110}. The shown stepped (111) surface has a (7,3,5) nomenclature and intersects the macroscopic {110} surface along [-554], i.e. the thin green line in Fig. 5.8. We note that the [-110] line signifies mirror symmetry and therefore on {110} similar ripples are expected to align along the [-55-4] azimuth. The angle between both azimuth directions amounts to 59° in close agreement with the data displayed in Fig. 5.4(b). We consider this finding as strong supporting evidence for the proposed model. From the lack of a peak just in center between the two major peaks we can safely conclude that an alignment of the ripples along [-110] is insignificant, which is in firm agreement with the earlier suggested importance of alignment of Pt-rich chains with steps. We do note that a vertical shift of the domains in Fig. 5.8 along [001] cannot be excluded. In the ideal case such a shift would result in an angular spacing of 31.6° instead of 59° (cf. thin blank arrows in Fig. 5.4(b). The data displayed in Fig. 4b show shows quite clear evidence in support of 31.6° next to ~ 60°. In addition, a variation of the atomic step distance, for instance by one atomic building block, would only result in an increase of the angular separation of the ripple orientations by 3.4°, i.e. from 59.0° to 62.4°. As an intermediate result we conclude that the situation sketched in Fig. 8 nicely covers the observations.

In an attempt to gain additional information on the step density along [-554] (cf. Fig. 5.8) we have a closer look at the width of the peaks along [11-2] (real space indication) as displayed in Fig. 5.9. The corresponding intensity profile is shown in Fig. 5.9(b). For comparison we use the intensity profile along [-211] in Fig. 5.9(c). Note that both directions correspond to azimuth directions on the {111} facets with the highest Pt density, according to Fig. 5.9. The full-width-at-half-maximum of the specular beam along [11-2] (1st intense spot from left in b) is about 1.6 times larger than along. After correction for distortion caused by the {110} projection (see also Figs. 5.7) an additional broadening by a factor of 1.3 still remains. Since the broadening of the peaks is directly related to the step density as described in a detailed fashion in Refs [30, 31], this directly implies that the step density along [11-2] is relatively high. This is in nice agreement with the discussion on the terrace width in Fig. 5.8 and the references to the line arrows in Fig 5.3(b) and supports the presence of a significant distribution of step widths along [-554].

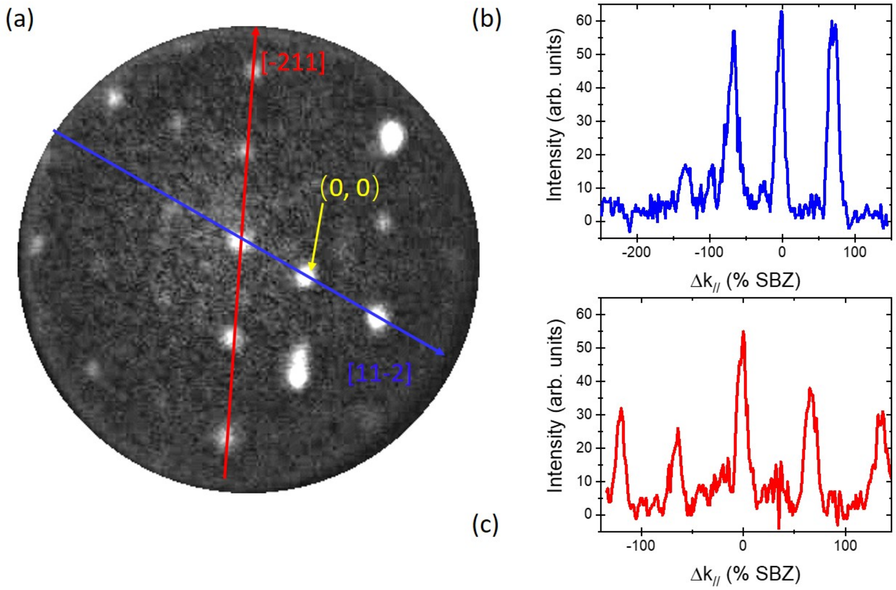

Figure 5.9: (a) The (3x3) μLEED pattern obtained at 5.4 eV. The azimuth directions indicate real space directions that correspond to azimuth direction on 111 with the highest Pt density cf. Fig. 5.8. The intensities have been corrected for the intensity variations resulting from the secondary electrons plume. Also indicated by an arrow is what we believe to be the specular spot (0,0). (b) and (c) show intensity profiles along [11-2] and [-211], respectively.

Encouraged by this result we now have a closer look at the step density along "[001]". For this purpose we inspect the μLEED pattern obtained for energies between 1.9 and 17 eV. In contrast to the broadening along [11-2] discussed above we now obtain clear evidence for the presence of well-defined split peak pairs for each energy. Characteristic data obtained at 4, 6, 10 and 15 eV are shown in Figs. 5.10 (a) – (d), respectively. Again, this evidence reveals the presence of atomic steps, now at a well-defined distance. According to, once more, Horn von Hoegen [20] a plot of the changes in vertical component of the wave vector plotted versus the parallel one directly yields the angle between the stepped facets and the constituting 111 terraces. The result is plotted in Fig. 5.10(e) for the split pairs measured in the energy window between 1.9 and 17 eV. The obtained angle is about 14° implying that the separation between [-554] steps is consistent with the presence of about 4 building block along a direction [0-11]. Therefore, the slope of the facets of the ripples on each side are about 21° from the The intermediate result for the emergence of the “spaghetti”-pattern can be summarized as follows. It is consists of ripples which are oriented mainly along [-554] – and equivalent directions on the {110} surface. The constituting material is Ge released by spinodal decomposition of the eutectic droplets upon passing the eutectic temperature of the GePt system. The facets of the parallel ripples (111)-vicinals topped by a Pt containing layer in a (3×3) (or, equivalently, $(\sqrt{3}\times\sqrt{3})R30$ř-structure in which one third of the Ge atoms in one of the bilayers, probably the lower one, is replaced by Pt atoms. The facets make an angle of about 21° with {110}.

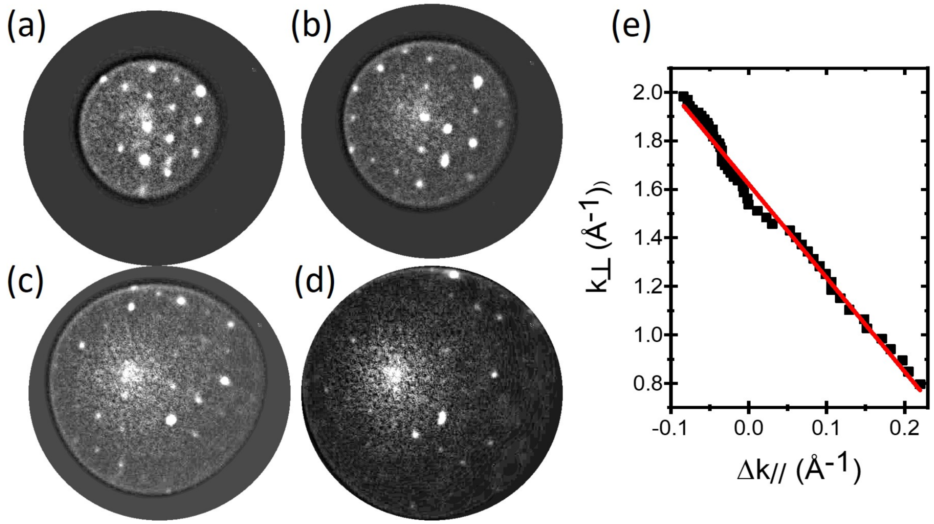

Figure 5.10: (a) - (d) μLEED patterns obtained at 4, 6, 10 and 15 eV, respectively. The pattern have been corrected for intensity variations resulting from the secondary electrons plume. The elllipses illustrate peak splitting along [-211] is due to steps at regular distances. The magnitude of this splitting is shown in (e) as a combination of $\Delta k_\perp$ and $\Delta k_\parallel$ obtained at each energy.

Above, we have discussed in quite some detail the break-away of Ge from a huge eutectic GePt droplet during a cool down through the critical temperature. As we have shown complex and large scale pattern formation occurs leading to ripples with vicinal (111)-facets of pure Ge covered by a $(\sqrt{3}\times\sqrt{3})$R30° Pt-containing cover layer. The ripples are oriented mainly along [-554], [-55-4] and also along [-552] and [-55-2] azimuth directions on the {110} surface. Nothing yet has been said about the counterpart, i.e. the emergence of Ge_2Pt crystallites upon passing through the eutectic temperature, in accordance with the phase-diagram in Fig. 5.2. The emergence of such crystallites has

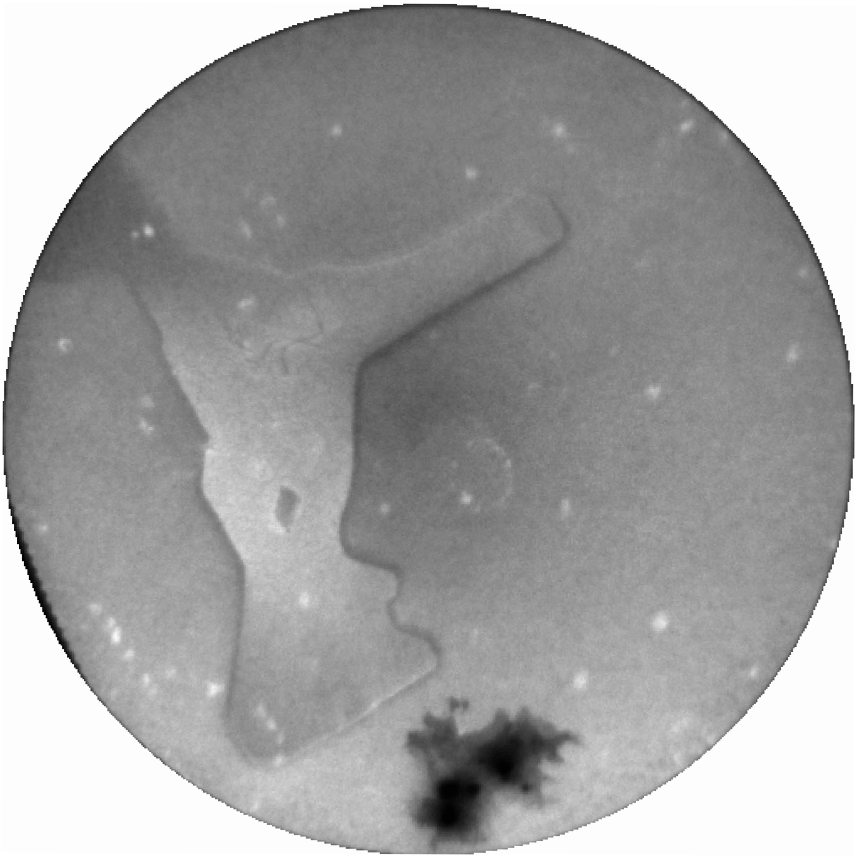

Figure 5.11: A LEEM image measured at room temperature, FoV 20 μm. Electron energy 3.1 eV. The “fairy circles” are left-over from former eutectic droplets originating from previous experiments. The small white features are probably 3D Pt-Ge objects. The irregularly shaped feature near the center is a 2D crystallite.

been reported recently [14] and their Ge_2Pt composition and crystalline structure was established beyond any doubt. Several crystalline shapes were detected, including so-called elongated hut clusters. These hut clusters have a {001} top face aligned parallel to Ge(110). An almost perfect match is detected along Ge[001] and twice the periodicity along the [100] azimuth on Ge_2Pt{100} equals well three times the periodicity along [-110] on Ge{110}. (110)-facets complete the hut clusters. Figure 5.11 shows a huge microcrystal. It was excreted at the position of the large droplet and the sharp and well-defined edges prove its crystalline nature. In contrast to the hut clusters, this large microcrystal has a rather compact shape. We refrain from a detailed structural analysis using μLEED, because of possible troubles due to field inhomogeneities around this huge microcrystal.

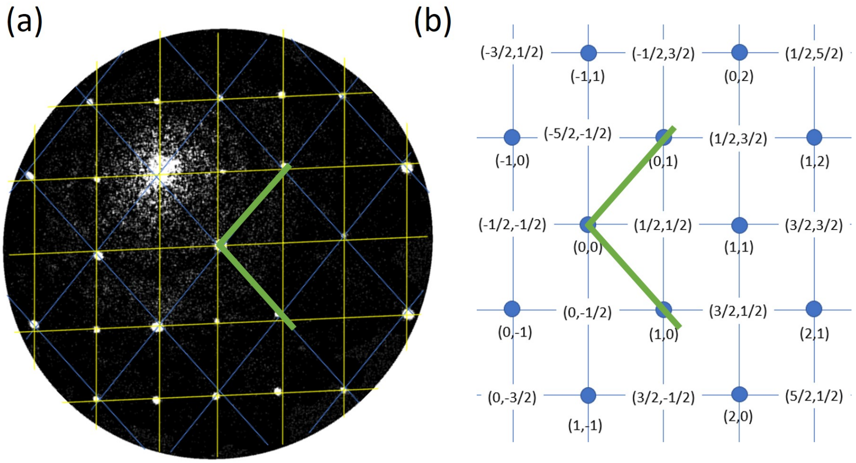

Figure 5.12: (a) Measured μLEED pattern on top of the 2D Ge_2Pt island shown; (b) Constructed LEED pattern for a base cell with two Pt atoms on a Ge_2Pt {101} plane.

As noted above both the composition and the overall crystal structure of the emerging Ge_2Pt are known. However, it appears that the intimate connection of these crystallites with the host substrate depends on the cooling rate. In order to obtain avoid possible complications related to field inhomogeneities around the huge clusters we have conducted μLEED measurements of the much smaller coagulated clusters at a distance of about one mm from the center of the surface in a further attempt to unravel the crystalline structure. Only limited coalescence has occurred at these positions and the passing small(er) clusters are still moving under the influence of the prevailing thermal gradient. As a result we cannot catch live the ultimate moment of solidification upon passing the eutectic temperature, but we can identify several crystallites after the action. A representative example is shown in Fig. 5.11 obtained at room temperature with 3.1 eV electrons. The small white blobs are probably crystalline Ge-Pt objects, but are too small to characterize in μLEED. Sometimes they are arranged in circular patterns and these “fairy circles” (see arrows) are left-overs of former droplets formed in earlier experiments. The irregularly shaped large feature turns out to be a 2D Ge_2Pt crystallite as is shown below. The crystalline structure of $PtGe_2$ is orthorhombic with $a = 6.179$ Å, $b = 5.779$ Å, $c = 2.914$ Å and $\alpha = \beta = \gamma = 90°$ [32]. Note that b equals the Ge lattice constant within about 2 % and a nice commensurability is obtained along Ge [001] if the contact plane is along the Ge_2Pt110 plane with the b-axis parallel to Ge[001]. The μLEED diffraction pattern obtained on-top of the Ge_2Pt island in Fig. 5.12(a), together with the expected diffraction pattern in Fig. 5.12(b). The blue grid in reciprocal space shows the primitive lattice for the $Ge_2Pt(101)$ contact plane, while the yellow grid corresponds to the centered two atomic base expected for the unit cell considering the Pt atoms only. This lattice is just slightly distorted when compared to the theoretical rectangular version. Given this limitation a very convincing agreement is obtained between the measured and the constructed patterns.

5.4. CONCLUSIONS

We first describe the expected initial shrinking of the project surface area of the droplet during cooling down, followed by an unanticipated expansion of the projected surface area. This is attribution to an initial fast amorphization of the interface between the droplet and the substrate, followed by recrystallization of the Ge expelled at this interface. In addition during spinodal decomposition the Ge expelled around the local hot spot on the surface is found to orient in parallel Ge ripples oriented mainly along [-554] and [-55-4] directons. Their sides are {111} and {11-1} Ge facets covered with an ordered Pt induced $(\sqrt{3}\times\sqrt{3})$ superstructure. Simultaneously we found the emergence of Ge_2Pt crystals across the entire surface, with their {101} planes oriented parallel to the Ge(110) interface.

BIBLIOGRAPHY

[1] W.C. Yang, H. Ade, and R. J. Nemanich, Phys. Rev. B **69**, 045421 (2004).

[2] P. A. Bennett, J. Chobanian, J. I. Flege, E. Sutter, P. Sutter,Phys. Rev. B **76**, 125410 (2007).

[3] P. Sutter, P. A. Bennett, J. I. Flege, E. Sutter, Phys. Rev Lett. **99**, 125504 (2007).

[4] A. El-Barraj, S. Curiotto, F. Cheynis, P. Müller, F. Leroy, Appl. Surf. Sci. **509**, 144667 (2020).

[5] S. Curiotto , F. Leroy, F. Cheynis P. Müller, Sci. Rep.**7**, 902 (2017).

[6] B.H. Stenger, A.L. Dorsett , J.H. Miller, E.M. Russell, C.A. Gabris , S. Chiang, Ultramicroscopy **183**, 72 (2017).

[7] Z. Zhang, B. Poelsema, H.J.W. Zandvliet, and A. van Houselt, Phys. Rev. Materials **5**, 105601 (2021)

[8] T.U. Schuelli, R. Daudin, G. Renaud, A. Vaysset, O. Geaymond, A. Pasturel, Nature **464**, 1174 (2010).

[9] G. Kurtuldu, J.F. Loeffler, Adv. Sci. **7** 1903544 (2020).

[10] M. Mroz, S. Tenney, T. Savina, M.E. Kordesch, AIP ADVANCES **8**, 065114 (2018).

[11] S. Curiotto, F. Leroy, F. Cheynis, P. Mueller, Sci. Rep. **7**, 1 (2017).

[12] Z.G. Zhang, B. Poelsema, H.J.W. Zandvliet, Phys. Rev. Mater. **5**, 105601 (2021).

[13] P. Bampoulis, L. Zhang, A. Safaei, R. van Gastel, B. Poelsema, H.J.W. Zandvliet, J. Phys.: Condens. Matter. **26** 442001 (2014).

[14] R. van Bremen, P. Bampoulis, J. Aprojanz, M. Smithers, B. Poelsema, C. Tegenkamp, H.J.W. zandvliet, J. Appl. Phys. **124**, 125301 (2018)

[15] T. Young, Philos. Trans. R. Soc., **95**, 65 (1805).

[16] R. N. Wenzel, Ind. Eng. Chem., **28**, 988 (1936).

[17] D.J. Eaglesham, H.J. Gossmann, M. Cerullo, Phys. Rev. Lett. **65**, 1227 (1990).

[18] C. Herring, Phys. Rev. **82**, 87 (1951)

[19] H. Okamoto, J. Phase Equilib. Diffus. **40**, 311 (2019).

[20] R. Hild, C. Seifert, M. Kammler, F.J. Meyer zu Heringdorf, M. Horn-von-Hoegen, R.A. Zhachuk, B.Z. Olshanetsky, Surf. Sci. **512**, 117 (2002).

[21] T.R.J. Bollmann, R. van Gastel, H. Wormeester, H.J.W. Zandvliet, B. Poelsema, Phys. Rev. B **85**, 125417 (2012).

[22] T. Yasue, T. Koshikawa, E. Bauer, J. Vac. Sci. Technol. B **20**, 2496 (2002).

[23] G. Binnig, H. Rohrer, C. Gerber, E. Weivel, Surf. Sci. **131**, L379 (1983).

[24] E. Bauer, Surf. Sci. **7**, 351 (1967).

[25] S. Tarlori, G. Galli, F. Gygi, M. Parrinello and E. Tosatti, Phys. Rev. Lett. **69**, 2947 (1992).

[26] R.M. Feenstra and J.A. Stroscio, Phys. Rev. Lett. **59**, 2173 (1987).

[27] A. van Houselt, M. Fischer, B. Poelsema, and H.J.W. Zandvliet, Phys. Rev. B **78**, 233410 (2008).

[28] A. Safaei, A. van Houselt, B. Poelsema, H.J.W. Zandvliet, and R. van Gastel, Phys. Rev. B **88**, 085415 (2013).

[29] J. Tersoff, Phys. Rev. Lett. **76**, 1675 (1996).

[30] T.M. Lu and M.G. Lagally, Surf. Sci. **104**, L229 (1981).

[31] M. Henzler, Surf. Sci. **19**, 159 (1970).

[32] K. Schubert, S. Bhan, M. Balk, H. Breimer, E. Stolz, and P. Esslinger, Naturwissenschaften **46**, 647 (1959).

6

SUMMARY AND OUTLOOK

THIS thesis is devoted to the study of the Pt/Ge(110) system. The Pt/Ge(110) system hosts interesting physics, since after the deposition of Pt on the intrinsically anisotropic Ge(110) surface and subsequent annealing at sufficiently high temperatures, the formation of the 2D material germanene, the germanium analogue of graphene, is observed. Germanene possesses, just like graphene, two sub-lattices and a honeycomb like structure with (partially) overlapping $2p_z$ orbitals. Consequently the band structure of germanene also exhibits a linear dispersion relation and the electrons in germanene can be also best described as massless Dirac fermions [1-2]. The formation of germanene in the Pt/Ge(110) system is connected to the formation of a Pt-Ge eutectic droplet at elevated temperatures and the subsequent spinodal decomposition upon cooling down.

A general introduction to the Pt/Ge(110) system is given in Chapter 1. After a general introduction of the Pt/Ge system, including a discussion of the Pt-Ge phase diagram, we shortly touched upon the intriguing 1D physics in the Pt/Ge(001) system [3] and introduce the Ge(110) surface.

In the second chapter we introduce Low Energy Electron Microsopy / Diffraction (LEEM/LEED) and Photo-Emission Electron Microscopy (PEEM) as the techniques of choice to study the dynamics of the Pt/Ge(110) system in situ, both above and below the eutectic transition. We show the versatility of these techniques, yielding information down to the level of individual droplets and clusters in both real space and reciprocal space. We detail how the obtained data is corrected for inhomogeneities in the channelplate detectors and in which way we correct for the contribution of the secondary electrons in the obtained LEED patterns.

Chapter 3 details the static properties of the eutectic droplets, which form in the Pt/Ge(110) system above the eutectic temperature as studied by PEEM, focusing on the properties of hemispherical eutectic droplets. From the experimentally obtained intensity profiles across these droplets we obtain both the local contact angle as well as the work function of the eutectic droplet. The photo-electron intensity is determined by both a direct surface contribution, as well as a contribution from a thin bulk-like skin near the surface of the droplet. The local inclination across the droplet's surface is a crucial ingredient to reconstruct the surface topography. The only two fit parameters in our description of the intensity are the contact angle and the work function of the eutectic droplet, the latter being the only parameter which influences the very characteristic bending of the intensity profile, thus enabling an absolute determination of the work function of the eutectic droplet. The obtained value for the contact angle from this fitting procedure is compared to an independent determination of the contact angle from both the interference pattern of the exciting electromagnetic radiation over the droplet's surface as well as a determination of the contact angle from the variation of the photoemission intensity behind the droplet, arising from diffraction of the incoming plane waves by the droplet. The determination of the work function of the eutectic droplet is compared to an independent determination from LEEM intensity variations with electron energy. For both the contact angle and the work function the values obtained from the different methods agree well with each other. In addition, by a comparison of the profiles along the advancing and the receding side of the eutectic droplets, we conclude that the droplets shape is exclusively determined by thermodynamics and the motion of the droplet plays no role.

The thermally induced motion of the micron sized eutectic PtGe droplets is studied in detail in chapter 4. The droplets move towards the higher temperature, driven by the entropy gain of the substrate atoms which become constituents of the eutectic droplet during its journey. The direction of motion is solely determined by the local thermal gradient, irrespective of the intrinsically strongly anisotropic nature of the Ge(110) substrate. We show that the velocity of the droplets is not determined by the diffusivity of Ge in the eutectic phase, as long has been assumed for metal-semiconductor eutectic systems. We provide evidence via LEED measurements that the droplets make direct contact with the flat Ge substrate, while the droplets are surrounded by a $PtGe_3$ crystalline wetting layer with a (2×1) structure. Dissolution of the edges of the wetting layer at the leading edge of the droplets is identified as the rate limiting step for its motion. We find an activation energy of 2.2 eV for this process. The variation of the velocity with temperature of other eutectic droplets in similar metal-semiconductor eutectic systems in the literature can be properly described using an Arrhenius fit.

The processes occurring during cooling of the eutectic droplets are the topic of chapter 5. We first describe the expected initial shrinking of the project surface area of the droplet during cooling down, followed by an unanticipated expansion of the projected surface area. This is attribution to an initial fast amorphization of the interface between the droplet and the substrate, followed by recrystallization of the Ge expelled at this interface. In addition, during spinodal decomposition the Ge expelled around the local hot spot on the surface is found to orient in parallel Ge ripples oriented mainly along [-554] and [-55-4] directons. Their sides are {111} and {11-1} Ge facets covered with an ordered Pt induced $(\sqrt{3}\times\sqrt{3})$ superstructure. Simultaneously we found the emergence of Ge_2Pt crystals across the entire surface, with their {101} planes oriented parallel to the Ge(110) interface.

In conclusion, we have studied the Pt/Ge(110) both above the eutectic transition temperature as during cooling and we encountered a wealth of interesting physics. We found that the movement of the eutectic droplets at elevated temperatures cannot be described by the dissolution-diffusion-repulsion mechanism [4], which is widely used for similar systems like Pt on Si [5-7], and Au on Si and Ge [8-11]. A detailed study and comparison of the (temperature dependence of the) droplet motion in these systems would be fruitful. A more detailed insight in the physics of these eutectic systems during spinodal decomposition, as we described in chapter 5, is a crucial ingredient in the ultimate goal of this thesis to tailor the Pt/Ge(110) system such that we gain a high degree of control on the production of germanene [12-14] in this system. Detailed comparison with and further investigations of (other) systems which involve a temperature driven phase transition in the production of 2D materials like silicene [15] is certainly warranted.

BIBLIOGRAPHY

[1] L. Zhang, P. Bampoulis, A.N. Rudenko, Q. Yao, A. van Houselt, and H.J.W. Zandvliet, Phys. Rev. Lett. **116**, 256804 (2016).

[2] L. Zhang, P. Bampoulis, A. van Houselt, and H.J.W. Zandvliet, Appl. Phys. Lett. *107*, 111605 (2015).

[3] D. Kockmann, T.F. Mocking, A. van Houselt, B. Poelsema, and H.J.W. Zandvliet, J. Phys. Chem. C **113**, 17156 (2009).

[4] H. E. Cline and T. R. Anthony, J. Appl. Phys. **47**, 2325 (1976).

[5] W.C. Yang, H. Ade, and R. J. Nemanich, Phys. Rev. B **69**, 045421 (2004).

[6] P. A. Bennett, J. Chobanian, J. I. Flege, E. Sutter, P. Sutter, Phys. Rev. B **76**, 125410 (2007).

[7] P. Sutter, P. A. Bennett, J. I. Flege, and E. Sutter, Phys. Rev Lett. **99**, 125504 (2007).

[8] A. El-Barraj, S. Curiotto, F. Cheynis, P. Müller, and F. Leroy, Appl. Surf. Sci. **509**, 144667 (2020).

[9] S. Curiotto, F. Leroy, F. Cheynis, and P.Müller, Sci. Rep. **7**, 902 (2017).

[10] B.H. Stenger, A.L. Dorsett, J.H. Miller, E.M.Russell, C.A. Gabris, and S. Chiang, Ultramicroscopy **183**, 72 (2017),

[11] F. Leroy, A. El Barraj, F. Cheynis, P. Müller, and S. Curiotto, Phys. Rev. Lett. **123**, 176101 (2019).

[12] P. Bampoulis, L. Zhang, A. Safaei, R. van Gastel, B. Poelsema, and H.J.W. Zandvliet, J. Phys.: Condens. Matter. **26**, 442001 (2014).

[13] R. van Bremen, P. Bampoulis, J. Aprojanz, M. Smithers, B. Poelsema, C. Tegenkamp,and H.J.W. Zandvliet, J. Appl. Phys. **124**, 125301 (2018).

[14] L. Zhang, P. Bampoulis, A. van Houselt, and H.J.W. Zandvliet, Appl. Phys. Lett. **107**, 111605 (2015).

[15] C. Volders, E. Monazami, G. Ramalingam, and P. Reinke, Nanoletters **17**, 299 (2017).

SAMENVATTING

In het proefschrift dat nu voor u ligt wordt een studie uitgevoerd naar de eigenschappen van het zogenaamde (110) oppervlak van de halfgeleider germanium (Ge, atoomnummer 32) wanneer daar een klein laagje platinum (Pt, atoomnummer 78) op wordt gedeponeerd. Dit Pt/Ge(110) systeem is fysisch interessant, omdat, als dit systeem naar een voldoende hoge temperatuur wordt verhit, de vorming van het tweedimensionale materiaal germaneen wordt waargenomen. Germaneen is de germanium versie van het bekendere grafeen. Beide materialen hebben twee subroosters in een honingraatstructuur waarin de $2p_z$ orbitalen (gedeeltelijk) overlappen. De bandenstructuur van de beide materialen vertoont grote overeenkomsten. In beide gevallen is de dispersie lineair en kunnen de elektronen worden beschreven als massaloze Dirac fermionen. De vorming van germaneen in het Pt/Ge(110) systeem is gerelateerd aan de aanwezigheid van een Pt-Ge eutectiucum bij voldoende hoge temperaturen. Tijdens het afkoelen via spinodale decompositie kan dit resulteren in de vorming van germaneen.

In het eerste hoofdstuk van dit proefschirft wordt het Pt/Ge(110) systeem geïntroduceerd. Daarbij wordt het Pt-Ge fase-diagram beschreven (figuur 1.1), met daarin het Pt-Ge eutecticum. Dit eutecticum is een mengsel van Pt en Ge, met een lagere smelttemperatuur dan de beide afzonderlijke fases waaruit het is samengesteld, Ge en Pt. De compositie waarvoor de smelttemperatuur van dit mengsel het laagst is, wordt het eutectisch punt genoemd. In dit geval ligt dit eutectisch punt bij een atomaire compositie van 22 % Pt en 78 % Ge. Vervolgens wordt beknopt de interessante fysica van het verwante Pt/Ge(001) systeem beschreven en wordt het hoofdstuk afgesloten met een introductie van de eigenschappen van het Ge(110) oppervlak.

De gebruikte meettechnieken worden beschreven in het tweede hoofdstuk van dit proefschrift. Alle beschreven experimenten zijn uitgevoerd in een zogenaamde lage-energie elektronenmicroscoop, waarin zowel afbeeldingen van het oppervlak kunnen worden gemeten (LEEM metingen) als diffractie-experimenten kunnen worden uitgevoerd (LEED metingen). Bovendien is het door gebruikt te maken van een UV-lamp ook mogelijk om foto-emissie microscopie (PEEM) metingen uit te voeren. Deze techieken zijn bezonder geschikt om de dynamica van het Pt/Ge(110) systeem te bestuderen, omdat het mogelijk is om bij temperaturen boven de eutectische temperatuur *in situ* metingen te doen van de dynamica en structuur van individuele eutectische druppels en het onderliggende substraat. Er wordt ook ingegaan op de correctie van de LEEM metingen voor de inhomogeniteiten in de detector en de correctie voor de secundaire elektronen, die diffractiemetingen beïnvloeden.

Uitvoerig worden in hoofdstuk 3 door middel van PEEM metingen de eigenschappen van de eutectische druppels, die zich bij voldoende hoge temperaturen vormen, bestudeerd. Deze druppels hebben de vorm van bolsegmenten. Uit de gemeten PEEM intensiteitsprofielen over deze druppels wordt de contacthoek en de uittreearbeid bepaald. Aan de PEEM intensiteit wordt bijgedragen door het oppervlak, maar ook door een dunne oppervlakte-laag met een bulk karakter, waarvan de bijdrage exponentieel afneemt naarmate de afstand naar het oppervlak toeneemt. De lokale kromming van het oppervlak bleek van cruciaal belang om uit de PEEM intensiteit de topografische vorm van de druppel te bepalen. Daarbij wordt gebruikt gemaakt van slechts twee fit parameters: de contacthoek van de druppel en de uittreearbeid van het PtGe eutecticum. Van deze twee heeft alleen de uittreearbeid invloed op de zeer karakteristieke bolling van de gemeten intensiteitsprofielen, wat een nauwkeurige bepaling van de uittreearbeid mogelijk maakt. De verkregen waarde voor de contacthoek wordt vergeleken met waardes die verkregen worden uit het interferentiepatroon in de PEEM intensiteit ten gevolge van reflectie van het exciterende UV licht aan het substraat oppervlak als ook met waardes afgeleid uit het diffratiepatroon achter de eutectische druppel. De verkregen waarde van de uittreearbeid wordt vergeleken met een onafhankelijke bepaling vanuit de variatie van LEEM intensiteit als functie van de elektronen-energie. Zowel de waardes voor de contacthoek als voor de uittreearbeid komen voor de verschillende methodes goed met elkaar overeen. Door vergelijking van metingen aan de voor- en achterzijde van bewegende druppels concluderen we dat de vorm van de druppels louter thermodynamisch bepaald wordt en dat contacthoekhysterese geen rol speelt.

De thermisch geïnduceerde beweging van de eutetische PtGe druppels wordt beschreven in hoofdstuk 4. De druppels, van enkele tot tientallen micrometers in diameter, bewegen naar de hoogste temperatuur, gedreven door de entropiewinst van de Ge atomen die onderweg opgenomen worden in de bewegende druppel. Alhoewel het Ge(110) oppervlak van nature anistroop is, wordt de bewegingsrichting louter door de temperatuursgradient bepaald. Aangetoond wordt, dat de snelheid van de druppels niet bepaald wordt door de diffusie van het Ge in de eutectische fase, zoals veelal wordt aangenomen voor metaal-halfgeleider systemen die een eutecticum vormen. Via LEED metingen laten we zien dat de druppels direct contact hebben met het Ge substraat, terwijl de druppels omgeven worden door een kristallijne $PtGe_3$ bevochtigingslaag met een (2×1) structuur. Het oplossen van de randen van deze bevochtigingslaag blijkt de snelheid van de druppels te bepalen. We vinden voor dit proces een activeringsenergie van 2.2 eV en kunnen dit proces, en vergelijkbare processen in de literatuur, goed beschrijven met Arrhenius gedrag.

De processen die optreden tijdens het afkoelen van de eutectische druppel zijn onderwerp van studie in hoofdstuk 5. Initieel blijkt het geprojecteerde oppervlak van een druppel af te nemen, gevolgd door een onverwachte toename. De afname wordt toegeschreven aan amorfisatie van het interface, omdat er heel veel Ge wordt afgezet, wat resulteert in een (tijdelijk) hogere oppervlaktespanning. Tijdens de spinodale decompositie worden er op het warmste gedeelte van het substraat veel extra Ge atomen afgescheiden. Deze ordenen zich in parallele rijen voornamelijk langs [-554] en [-55-4] richtingen. De zijvlakken van deze rijen zijn {111} en {11-1} Ge facetten bedekt met een geordende Pt geïnduceerde $(\sqrt{3} \times \sqrt{3})$ structuur. Tegelijkertijd ontstaan er op het gehele oppervlak Ge_2Pt kristallieten, met hun {101} vlakken parallel aan het Ge(110) oppervlak.

ACKNOWLEDGEMENTS

I would like to thank the Chinese Scholarship Council (CSC) for financially supporting my PhD project at the University of Twente. It is a great honor for me that this opportunity has been offered to me. I would also like to thank my supervisors, colleagues, friends and parents as well as my relatives for their help, support and encouragement.

I would like to thank my supervisor, Prof. Harold Zandvliet, who gave me the opportunity to perform my PhD study in his group. The first appointment we had dated back to early 2017. During these discussions I presented the research that I did during my master study in China, whereas Harold gave a brief impression of the PhD project that was available in his group. I was highly interested in this challenging PhD project as well as the new research environment. Although 4 years is not a long period, I believe I have learned a lot and have become a more mature researcher.

Besides Harold, I would also like to thank Dr. Arie van Houselt and in particularly, Prof. Bene Poelsema. Without their guidance, help and continuous support I would not have been able to complete my PhD project. I still remember the first presentation I had to give during the weekly group meetings. I found it difficult, not only because of the language, but also because of the different research backgrounds. However, with the help of my supervisors and colleagues I have managed to deal with these challenges.

I'm particularly grateful to Prof. Bene Poelsema. At first sight one might have the impression that he is a very serious person, but if you know him better you will quickly find out that he is a very kind and very wise man with an exceptionally creative mind. Once he sent me an email that he wanted to share with me how to build the bridge between an experiment and a model. He emphasized the importance of independent thinking, which I neglected before. Bene's ability to elucidate the difficulties in a simple terms was an eyeopener for me. I highly appreciate the numerous discussions I had with him. His sharp and clear mind always shed new light on problems and his attitude towards research has profoundly affected my life.

Arie taught me all the ins and outs of low energy electron microscopy in a step-by-step fashion. In my first attempt I failed to reproduce all these steps, but Arie patiently explained it again and again. I like Arie's positive attitude and in the case that we encountered problems, he always replied by "That's life". I also enjoyed the numerous discussions I had with him. He taught me that the palest ink is better than the best memory.

Junia has contributed to the work described in chapter 4. I'm very gratefull for her detailed analysis and would like to wish her success with her own PhD project.

I have been a proud member of the Physics of Interfaces and Nanomaterials group. I enjoyed the pleasant and helpful atmosphere in the group. Special thanks to the support staff Simone, Martin and Hans. I'm also much indebted to my fellow PhD students Zhen Jiao, Lijie Zhang and Qirong Yao for their continuous support, ideas, help and encouragement. I'm still in touch with them and I hope to stay in touch with them as they have played a very important role in my life. I also much indebted to my other PIN colleagues Kai, Pantelis, Martina, Carolien, Valent, Jort, Jorn, Binglin, Xiaolai, Yuxuan and the numerous BSc and MSc students of the PIN group. I wish the PIN group a prosperous future.

Many Chinese friends have accompanied me in the Netherlands. Zhen Jiao, Weiqiu Chen and Min Lin I already knew before I entered the Netherlands. There are all very kind and introduced me to many more new Chinese friends. I would like to thank Jie Wang, Penfei Sun, Pei Zhang, Ruosha Zeng, Hao Wu, Jinmeng Hao, Dan Hu and others for the nice parties and activities that released the pressure and allowed us to recharge our batteries. I share very good and pleasant memories to a visit of Italy together with Pei Zhang, Weiqiu Chen, Minsi Li, Zhen Jiao, Ye Lyu, Tao Tian, Kun Dai and Keyan Chen. The Italian culture, the beautiful buildings, the delicious food, the fun we had has enriched us. In the second year Panfei, Jie, Zhen and I rented a house together, where we became brothers for life. In the third year we, unfortunately, had to stay at home owing to the outbreak and spread of the corona virus. However, Jie, Panfei, Pei, Weiqiu, Zhen, Yu, Ye and me as well as many other friends encouraged and supported each other, which resulted eventually in a big unified family. This and many other experiences have resulted in great memories that I do want to cherish and remember forever.

Last, but not least I would like to thank my parents, sisters, bother and relatives for their unconditional support. Of course also special thanks to my girlfriend and her relatives for their continuous and warm support. Distance and time cannot separate us. Without your care, help and support it would have been impossible to complete this PhD project. I look forward to a bright and promising future.

All BEST WISHES TO MY PARENTS, RELATIVES, COLLEAGUES and FRIENDS. I wish you all a healthy, happy and successful future.

身体健康

万事如意


LEEM
PEEM
LEED
PIN
PNAS
ACTA
PRL
Science
Nature